**The Dissertation Committee for Guillaume Jack Nicolas Noiseau Certifies that this is the approved version of the following dissertation:**

# Study of Atomic-scale Mechanisms for Deposition of Nanostructured Films from Nanoparticles

**Committee:**

Desiderio Kovar, Supervisor

Michael F. Becker

John W. Keto

David Bourell

Paulo Ferreira

# Study of Atomic-scale Mechanisms for Deposition of Nanostructured Films from Nanoparticles

**by**

**Guillaume Jack Nicolas Noiseau, M.S.E.**

**Dissertation**

Presented to the Faculty of the Graduate School of

The University of Texas at Austin

in Partial Fulfillment

of the Requirements

for the Degree of

**Doctor of Philosophy**

**The University of Texas at Austin**

**December 2015**

*To my parents*

# Acknowledgements

There are many people I would like to thank for making this project possible. First and foremost, I would like to thank my supervisor Dr. Kovar, for his exceptional guidance, advice and expertise in the field of Materials Science. I would like to thank Drs. Becker and Keto for their invaluable input on the many aspects of the LAMA process, both practical and theoretical. Their input that was essential in conducting this project. I would also like to thank my other two committee members, Drs. Bourell and Ferreira for their service and advice.

Dr. Jarvis deserves a special thank for her help and expertise in transmission electron microscopy, and for guiding my choices when it came to the challenging tasks of preparing, manipulating and analyzing ultra-thin electron-transparent samples of material. Dr Swinnea's expertise in the field of X-ray diffraction was also invaluable.

I would also like to thank Michael Gammage, whose contribution in running and improving the LAMA lab throughout the years was essential, and Tushar Chitrakar for providing the molecular dynamics simulations presented in this work. My other colleagues and friends, either long-term or short term members of the LAMA team, are also to thank for their contribution and support: Zach Levine, Malcolm Hamilton, Etienne Coffy, Davy Ea, Manuj Nahar, Claire Davis, Romain Fleury and Kris Gleason.

**Study of Atomic-scale Mechanisms for Deposition of Nanostructured Films from Nanoparticles**

Guillaume Jack Nicolas Noiseau, Ph.D.

The University of Texas at Austin, 2015

Supervisor: Desiderio Kovar

The LAMA process (Laser Ablation of Microparticle Aerosols) is a manufacturing process for producing thin to thick films by supersonically impacting nanoparticles (NPs) onto a target substrate. The goal of this work is to study the mechanisms occurring at the atomic scale during LAMA within the impacting NPs and in the nearby substrate, and ultimately to use this knowledge to control the microstructure and properties of the resulting films. For example, dense, polycrystalline films or single-crystal (epitaxial) films would produce films with high conductivity and would make the LAMA process a good candidate for manufacturing films with properties that cannot be achieved at room temperatures by other film deposition techniques. Conversely, films with high porosity and surface area are desirable for catalysis and other applications. Thus, the ability to systematically tune the film microstructure through control of the process parameters would broaden the applicability of LAMA for film production.

In this dissertation, the impaction of silver nanoparticles is studied in detail through a combination of experimental techniques. Scanning electron microscopy, transmission

electron microscopy, and x-ray diffraction techniques are utilized to study the final microstructure of the films. The experimental results are compared with molecular dynamics (MD) simulations that allow both the evolution of the microstructure during impaction as well as the final microstructure after impaction to be studied. The influence of increasing the speed of impacting NPs on the morphology of Ag films is studied, and evidence is shown that film density can be increased using this route. Epitaxial deposition of NPs at a local level is observed using electron microscopy observations and the mechanisms for the occurrences of epitaxial deposition is presented. The challenges for obtaining fully epitaxial deposition of films are discussed.

# Table of Contents

## List of Tables

## List of Figures

# Chapter 1: Introduction

The LAMA process (Laser Ablation of Microparticle Aerosols) is a manufacturing process to produce thin–to–thick films by supersonically impacting nanoparticles (NPs) onto a target substrate. It has been shown previously [1]–[3] that this process can produce a variety of nanostructures ranging from highly porous films to nearly dense, nanocrystalline materials from metallic, semi-conducting, or dielectric NPs. The goal of this dissertation is to develop an understanding of the atomic-scale mechanisms that occur when metallic NPs impact onto a substrate at high velocities and stick to produce films. Ultimately, this knowledge can be used to extend the process to produce film nanostructures and microstructures that cannot be produced currently. A particular focus of this dissertation is in determining if it possible to produce dense, nanocrystalline films or single-crystal films because such films would be highly desirable and cannot be easily produced by other film deposition techniques.

For this work, films have been produced from the impaction of Ag NPs. Some potential applications that could benefit from patterned Ag thin or thick films deposited with a controlled microstructure include electronic interconnects and packaging.

A number of processing parameters (gas type, gas pressure and ablation energy) have been used previously to influence NP size, impaction velocity, and ultimately, the film microstructure when producing films using LAMA. Unfortunately, these parameters influence both NP size and impaction velocity simultaneously. Because of the difficulty

in individually controlling the factors that influence film formation and also the difficulty in measuring impaction events at the velocities necessary for producing films (300 – 1200 m/sec), most of the literature related to film formation by impaction of NPs rely on molecular dynamics (MD) simulations [4]–[7]. These simulations have been used to study mechanisms for film formation and the resulting morphologies of films produced by impaction of NPs. However, it is notable that these models have not been validated by experimental data that would confirm the predicted microstructures. Fig. 1.2 shows an example of the results of MD simulations that predict a transition from porous to dense microstructures as the impaction velocity of the NPs is increased. Validating these models with experimental observations would make them a valuable tool in understanding the mechanisms that cause the NPs to stick upon impaction (e.g. plastic deformation, melting, etc.) and the resulting film microstructure, since these mechanisms are not well understood.

In this dissertation, a new method for experimentally varying impaction velocity is presented that, unlike previous methods, does not simultaneously alter particle size. This allows a systematic set of experiments to be conducted where only particle velocity is varied. In addition, the range of film architectures that can be produced over large areas is extended. The resulting film morphologies are characterized and analyzed, starting from a macroscopic point of view and progressing down to the atomic scale. Appropriate characterization techniques have been used to study film microstructures across this scale range: optical profilometry, scanning electron microscopy (SEM), transmission electron microscopy (TEM) and X-ray diffraction provide information about the film densities,

pore and grain morphologies, and grain size. The experimental results are compared to MD simulations to determine likely NP deformation and film formation mechanisms.

**Figure 1.1: Example of MD simulation predicting an increase in film density as the kinetic energy of impacting NPs is increased, reprinted from [5] a) 0.1 ev/atom and b) 1 ev/atom**

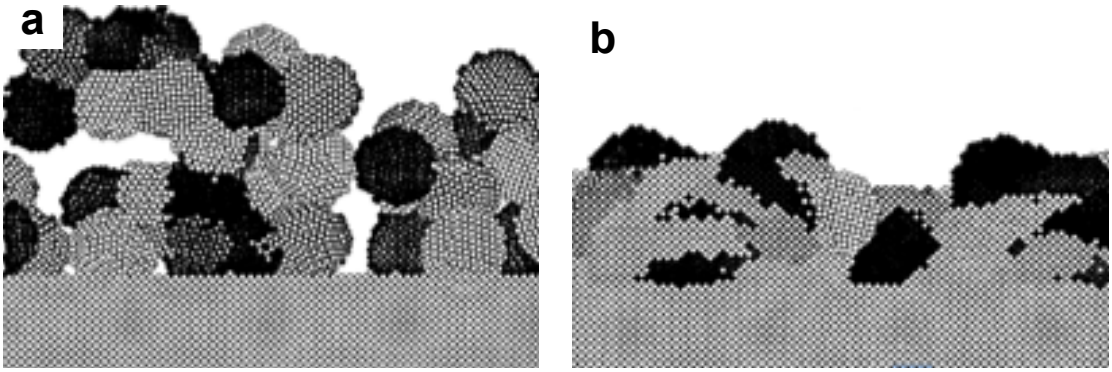

# Chapter 2: Background

This chapter presents background information that is relevant to understanding the mechanisms for formation of thin or thick films by impaction of particles. Existing manufacturing processes that utilize impaction of particles accelerated to velocities of 100 - 1,500 m/s to deposit films are reviewed and compared over the full range of particle sizes that are currently used for film deposition by high velocity impaction of aerosols.

Cold-gas dynamic-spray (CGDS) relies on the impaction of microparticles (MPs) ranging from 5 μm - 50 μm. The aerosol deposition method (ADM) utilizes large nanoparticles (NPs) ranging from 80 nm - 400 nm. The LAMA process used in this work utilizes small NPs (5 - 40 nm). Here we focus on the fundamental differences in impaction mechanisms that occur when the particle size is varied over this range. The methods used to model the impaction process and predict the microstructure of deposited material are also reviewed. Our goals are 1) to understand the deformation mechanisms that impacting particles undergo 2) to predict the resulting film microstructures 3) to use this information to control processing parameters and 4) to produce films with a well-controlled microstructures. These mechanisms are not well understood for NPs, but it is established that particle size and impaction speed are two parameters that have a significant influence on the mechanisms operating at the atomic scale upon impaction of particles, and ultimately on the final microstructure.

## 2.1 Film deposition by impaction of microparticles (MPs)

Cold-gas dynamic-spray (CGDS), also referred to as cold spray (CS), is an established, commercial process that was developed as a high deposition rate method for depositing thick films [8]. CGDS uses the expansion of a compressed gas (usually around 35 MPa; the gas is often heated) through a De Laval type nozzle to accelerate microparticles (5 μm- 50 μm) to typical speeds of 500 m/s – 1000 m/s.

**Figure 2.1: Schematic of typical setup for cold gas spraying, reprinted from [9]**

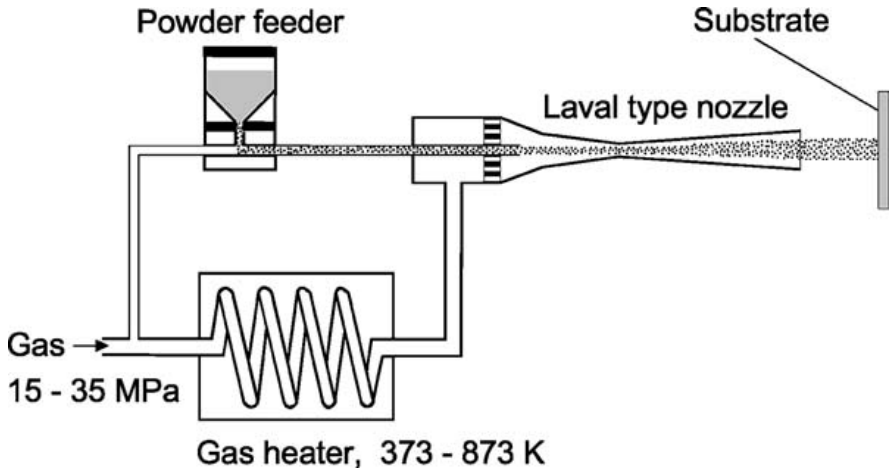


Compared to other aerosol deposition processes, there are three critical differences in CGDS: 1) the size of the accelerating nozzle is large, allowing large area films to be deposited quickly with a single-pass film width of 1 cm or more [10] (2) The particle size is larger than in other particle deposition processes, and 3) the pressure downstream of the nozzle is atmospheric pressure, whereas the other processes require vacuum. The films produced from metals such as Al, Cu, Ni, Zn and Ti form a dense film [8] (up to 99% relative density). Contrary to other deposition processes, the deposition of ceramics using CGDS has not been reported. Other important aspects of this process are that MPs stay substantially below the melting temperature of the impacting material and that little

heat is transferred to the substrate upon impaction, so the growth process occurs by deformation of the MPs and through disruption of the oxide layer at the surface, rather than melting/solidification of the MPs [11]. The intimate contact between the clean surfaces of the deformed particle and that of the substrate, combined with high pressures resulting from impaction, are believed to create chemical bonds and thus permit the growth of films. Fig. 2.2 presents macroscopic and microscopic views of cold-sprayed materials. The deformation of impacting MPs is obvious in the final microstructure (Fig. 2.2.b), as well as a high dislocation density resulting from plastic deformation (Fig.2.2.c).

**Figure 2.2: (a) Macroscopic view of cold-sprayed Al deposited with increasing substrate translation speed from left to right, reprinted from [12]**
**(b) Optical micrograph showing the microstructure of cold-sprayed Al, reprinted from [9]**
**(c) TEM micrograph showing high dislocation density in cold-sprayed Al, reprinted from [13]**

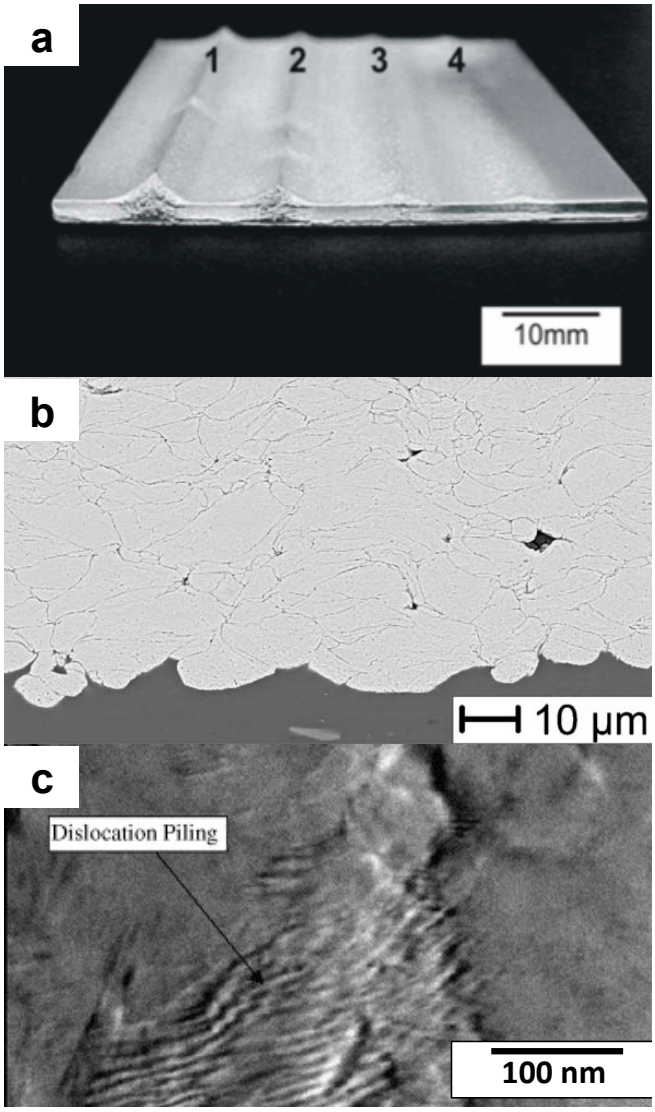


The extremely high particle impaction speeds and associated strain rates make it extremely challenging to experimentally determine mechanisms for deformation directly. Thus, modeling has been used to understand potential mechanisms for deformation and particle sticking. For impaction of MPs, finite element models (FEM) have been used by various research groups [9], [11]. In the CGDS process, the relatively large size of the

impacting particles makes it possible to assume bulk constitutive plasticity behavior. Using this assumption, the FEM have shown that deformation is mostly isolated to narrow regions near the interface between the particle and the substrate. The high strain rate combined with softening from heating creates a feedback loop: heating softens the material which leads to localized deformation in the heated regions, which results in more heating. This creates favorable conditions for the onset of adiabatic shear instabilities. These instabilities lead to jetting of material and extensive deformation of the MP and substrate upon impaction. This MP deformation and sticking mechanism had been validated both experimentally and by computer simulation (Fig. 2.3).

**Figure 2.3: (a) Plan-view SEM micrograph of MP after impaction on a substrate, taken from [9] (b) FEM model of the cross section of a 25 µm Cu MP impacting onto a Cu substrate at 550 m/s, taken from [11]**

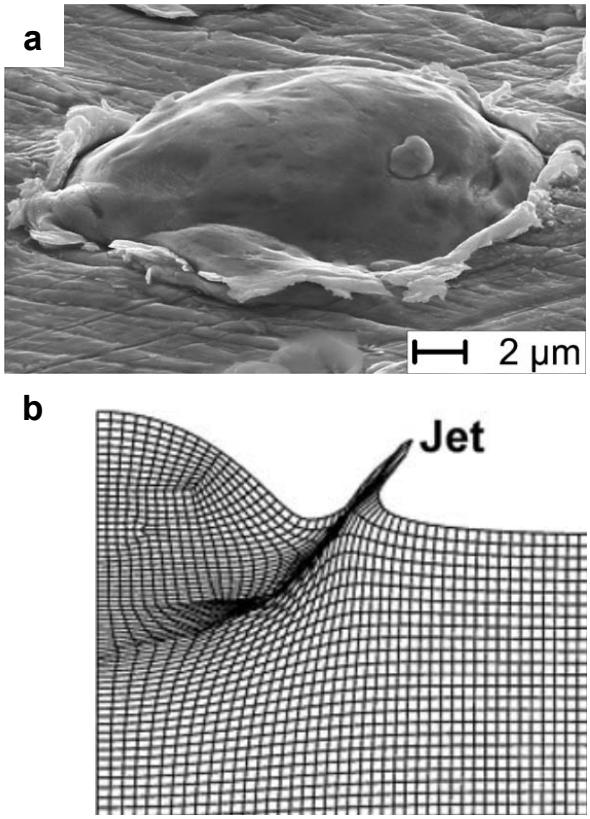

The critical impaction speed at which adiabatic shear instabilities are observed in the FEM correlates well with experimental measurements of critical speed for particle adhesion [9], [11]. In addition, TEM observations, particularly in the regions where the shear instabilities are observed, show very high dislocation densities [13]. Thus, it is believed that the deformation and sticking that occurs during the impaction of MPs is the result of bulk plastic deformation associated with dislocation activation and motion.

In CGDS, particles smaller than 5 μm cannot be deposited, unlike in the ADM and LAMA processes discussed later. In CGDS, the inlet of the impacting nozzle is at high pressure while its outlet and the deposition chamber are kept at atmospheric pressure. Therefore, a high pressure bow shock forms at the surface of the target substrate [14], [15]. Particles smaller than 5 μm cannot be deposited because they do not have enough momentum to cross the high pressure bow shock. To deposit smaller particles, the process would need to be modified so that a lower inlet pressure was used. This would reduce the pressure in the bow shock and allow smaller particles to have sufficient momentum to deposit. To accomplish this, the deposition chamber would need to be under vacuum to generate the pressure differential necessary for acceleration of the particles to achieve supersonic speeds.

## 2.2 Films deposition by impaction of nanoparticles (NPs)

### 2.2.1 Films produced by impaction of large NPs (ADM)

Akedo *et al.* [16]–[20] have studied the aerosol deposition process (ADM) as an alternative manufacturing process to fabricate dense or nearly dense films. Their studies are among the few studies providing any experimental data in the field of film growth by

NP impaction. ADM utilizes large nanoparticles (NPs) ranging from 80 nm - 400 nm, accelerated to 100-600 m/s. This is a versatile process that allows several types of materials to be deposited: Both metals (Ag) and ceramics ($Al_2O_3$, $Y_2O_3$, PZT ) have been reported. Deposited films exhibit a high as-deposited density (85% bulk density to fully dense). The ADM process has a high deposition rate compared to conventional film deposition techniques, enabling films with a thickness between 1-100 μm, suitable for optical coatings, MEMS or electrode applications.

**Figure 2.4: Schematic of experimental setup for ADM, reprinted from [21]**

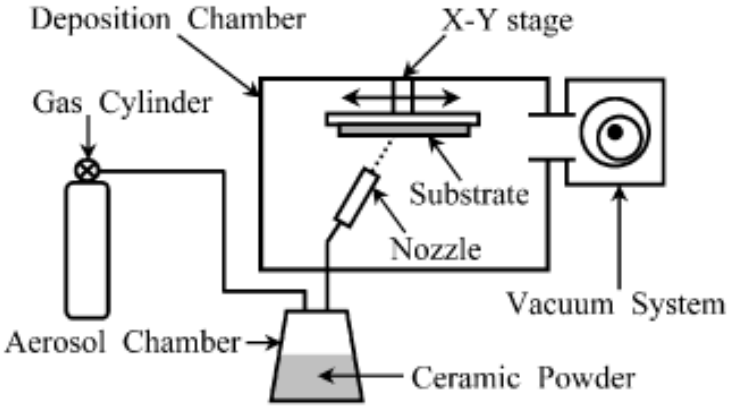


A viable method to control the microstructure of final deposits was reported in [20]. It was shown that the microstructure of $Al_2O_3$ films produced from the same starting particles of 80 nm, accelerated to the same speeds, could be controlled by varying the temperature of the substrate. This phenomenon was attributed to the changes in the mechanical properties of the substrate and particle materials. As the substrate temperature was varied from -30 °C to 450 °C, the microstructure transitioned from dense with an average grain size of 11 nm (see Fig. 2.5), to a highly porous microstructure with an average grain size of about 43 nm. No deposition occurred for substrate temperatures above 500 °C.

As opposed to the impaction mechanisms occurring in CGDS, Akedo *et al.*'s work suggests that there is a transition in behavior that occurs when the impacting particle size is reduced and that below a critical particle size, film formation is no longer controlled by bulk dislocation motion. Although they have not performed quantitative modeling of the mechanisms occurring upon NP impaction, they have suggested a qualitative model in which particles in this size range fracture upon impaction [20], based on experimental results showing the reduction in film grain size relative to the impacting particle size.

**Figure 2.5: TEM micrographs of $Al_2O_3$ deposited by ADM, showing a dense, nanocrystalline grain structure [19]**

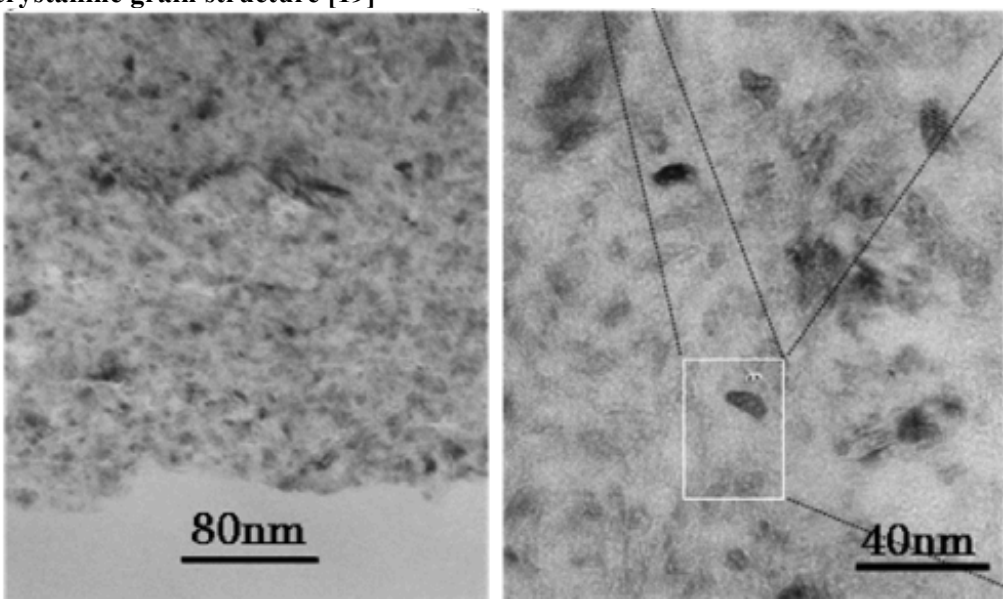


### 2.2.2 Films produced by impaction of small NPs (LAMA)

The laser ablation of microparticle aerosol (LAMA) process used for this work can produce films up to 50 μm thick by supersonically impacting NPs onto a target substrate. Compared to ADM, the LAMA process utilizes smaller NPs (2 - 40 nm). The small particle size used in LAMA makes this process amenable for direct comparison between experimental observation of LAMA-produced materials and available MD simulations.

Indeed, NP impaction for NP larger than 10 nm are difficult to implement due to the large computing capacity necessary to model the impact event, even when super computer resources are being used. Thus, with the LAMA process, there is the opportunity to couple experimental observations to MD simulation, unlike with the ADM process.

In short, the LAMA process consists of the following: feedstock MPs are entrained in a carrier gas (He in this study) and converted into NPs when illuminated by the pulse of an excimer laser. The resulting NPs are then accelerated via a pressure differential using a flat-plate nozzle and impacted onto the substrate. Unlike CGDS but similarly to ADM, the upstream chamber is maintained at atmospheric pressure, while the deposition chamber is maintained under vacuum (typically, 200 mTorr). Therefore the bow shock forming upon recompression of the accelerated gas forms at atmospheric pressure, which enables the deposition of small particles that could not be deposited via CGDS. More details on the apparatus, processing conditions, and capabilities of the LAMA process are provided in chapter 3.

This process allows the production of NPs from virtually any inorganic material. Currently, highly porous films of nanocrystalline materials from metallic, semi-conducting or dielectric NPs can be deposited. The density of Ag films deposited using a 0.25 mm diameter impacting nozzle has been estimated to be 70% relative to bulk Ag [22] with an average grain size of 25 nm [23]. A notable aspect of LAMA-deposited film microstructure is that the grain size is larger than the impacting NPs size. The size of NPs typically ranges from 2 nm to 40 nm, with a size distribution centered around 5 nm [2]. In this study, the impacting velocity of Ag NPs has been increased while keeping the same NP size to study the influence on the final microstructure.

### 2.2.3 Modeling and film formation mechanisms for small NPs

Although the high impaction velocities and unknown material properties for materials with nano-sized grains makes it extremely difficult to measure deformation experimentally in real time, particles in this size range are amenable to modeling using atomic-scale simulation methods. Several research groups have studied NP impaction for film deposition using molecular dynamics (MD) simulations for NPs with similar sizes and at similar impaction velocities to those that are typical for the LAMA process. Some of their results are summarized in Table 2.1. In particular, when studying the impaction of individual NPs, two regimes can be distinguished: epitaxial deposition and non-epitaxial deposition (see Fig. 2.6). In the epitaxial regime, the crystal lattice of the impacting particle aligns with that of the substrate, and the resulting grain size of the deposited film is larger than the size of starting NPs. In the non-epitaxial regime, the impacting particle adheres to the substrate but its crystal lattice does not fully realign with that of the substrate. The grain size of the deposited film is thus equal to or smaller than that of the starting NPs. Notably, unlike impaction of MPs in CGDS, there are no dislocations present in the impacting NPs because they are not stable in particles in this size range [24]. This suggests that there are fundamental differences between the sticking and deformation mechanisms for NPs compared to MPs.

The MD simulations have been used to study the microstructure of deposited films (density, grain size, degree of epitaxy) for various impacting conditions. They suggest that at low energies many of the particles elastically bounce off the surface and do not stick to form a film [25] At higher energies ($\geq$ 0.2 eV/atom) the particles stick but the resulting films are porous and polycrystalline. As shown on Fig. 2.8, in the energy

range of 0.5-1 eV/atom, a small change in energy of impacting NPs can lead to a large difference in the final microstructure [26]. In particular the film density increases and a transition from non-epitaxial to epitaxial deposition is predicted. These predictions suggest that previous LAMA films were deposited in the non-epitaxial deposition regime and that epitaxial regimes can be achieved by increasing the impaction energy of NPs by just a small amount. Unfortunately, there have been no previous experimental studies for NPs in this size and impaction velocity range to validate these predictions.

**Table 2.1: Summury of MD simulations results for film growth by impaction of NPs, and comparison with previous LAMA-deposited films**

| Author | Exp / Sim | Material | NP size *number of atoms or nm* | Impaction Energy *eV/atom* | Epitaxy | Density (relative to bulk) |
|---|---|---|---|---|---|---|
| Haberland 1995 [5] | Sim | Mo | $10^3$ | 1) 0.1<br>2) 1<br>3) 10 | 1) No<br>2) Yes<br>3) Yes | 1) Low<br>2) 80%<br>3) 100% |
| Meinander 2005 [6] | Sim | Cu | 140 to 15,700 | 1) 0.005<br>2) 0.05<br>3) 0.6<br>4) 1.0 | Yes if E > 5eV/atom and size > 2000 | - |
| Meinander 2008 [27] | Sim | Cu | 711 (2.5 nm) | 0.005 | - | 30% |
| Nordlund 2008 (review paper) [26] | Sim | Au | 1) $10^3$<br>2) $10^4$ | 1) 0.4<br>2) 0.3 | yes | - |
| Akedo 2005 [20] | Exp | $ZrO_2$ | 400 nm | - | - | Powdery to dense as substrate temperature decreases |
| LAMA [22], [23] | Exp | Ag | 3800 (5 nm) | 0.47 | no | 70% |

**Figure 2.6: Deposition regimes of NPs: (a) non-epitaxial deposition showing a grain boundary within the deposited nanoparticle (b) epitaxial deposition where the entire nanoparticle inherits the same orientation as the underlying substrate, taken from [6]**

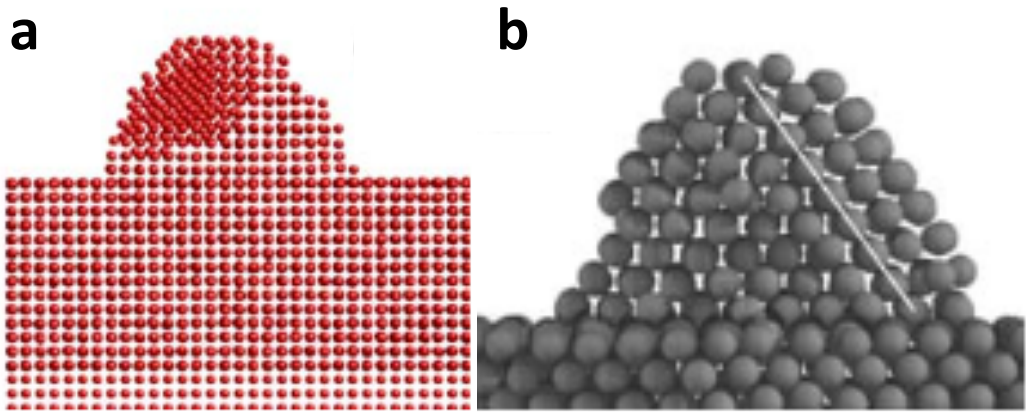


**Figure 2.7: Impacting energy and NP size ranges for epitaxial and non-epitaxial deposition of Au NPs, adapted from [26]. The current LAMA conditions are shown in the box.**

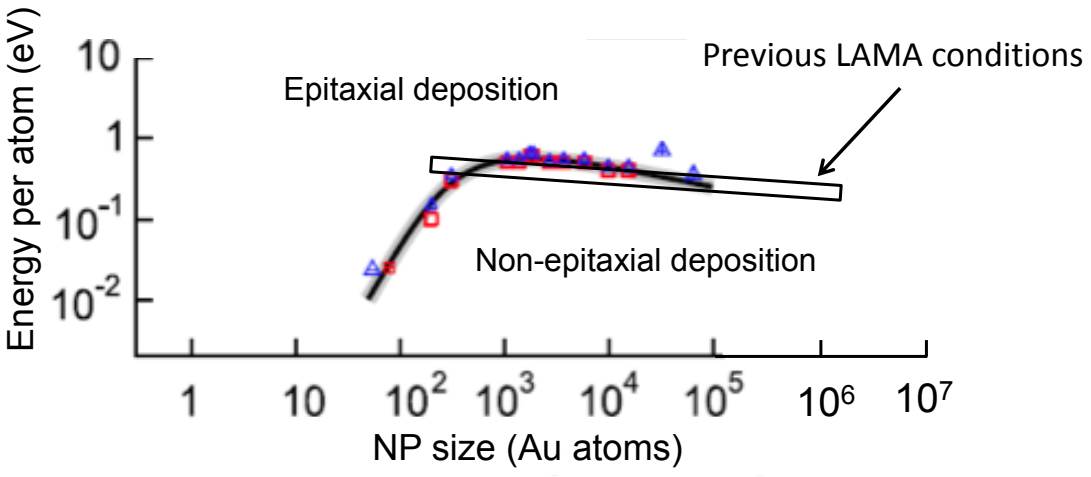

# Chapter 3: Direct Writing of Nanoparticulate Films

The LAMA direct-write, additive manufacturing process, where nanoparticles (NPs) are impacted onto a target substrate, is used to produce patterned thin and thick films. This chapter describes the equipment used to first create an aerosol of NPs from starting feedstock microparticles (MPs), then accelerate and impact the NPs onto a target substrate to produce films. The substrate is mounted on a motion-controlled stage to control the film pattern geometry and the film thickness by varying the translation speed of the stage under the NPs jet. The x-y resolution of the pattern is limited by the width of the NP jet (50 μm to 250 μm depending on process parameters) rather than by the resolution of the stage. The equipment was originally designed and built to accelerate the NPs using an accelerating nozzle with a 0.25 mm orifice; for this dissertation the apparatus was adapted to accommodate larger nozzles with 0.5 and 1 mm diameters. This allows for the deposition of NPs with increased impaction velocity relative to experiments conducted previously with LAMA.

## 3.1 Equipment to create an aerosol of nanoparticles

### 3.1.1 Principle of laser ablation

The physics of NP formation when a microparticle is illuminated by a laser pulse have been described previously [1], [2]. Two regimes of NP formation are possible, depending on the laser fluence (energy per unit area). At low fluences, the laser energy is uniformly absorbed by the MP, which results in sublimation from the surface of the MP.

NP formation results from subsequent condensation of the vapor, but particles produced from this mechanism tend to have a wide size distribution [2]. A second mechanism for NP formation occurs if the fluence exceeds the threshold for plasma breakdown. In this case, a high pressure/density shockwave is produced that travels through the MP. NPs form in the rarefaction region, behind the shock [28]. The shockwave-driven mechanism results in finer particles with a narrower size distribution [2], and has therefore been preferred for this work.

During laser ablation of microparticles, the laser pulse is long enough so that the NPs are formed while the laser is still on. Thus, the NPs are charged due to photo- and thermal- ionization. This prevents agglomeration for time before recombination occurs.

**Figure 3.1: Formation of NPs following laser ablation of a MP, reprinted from [29]**

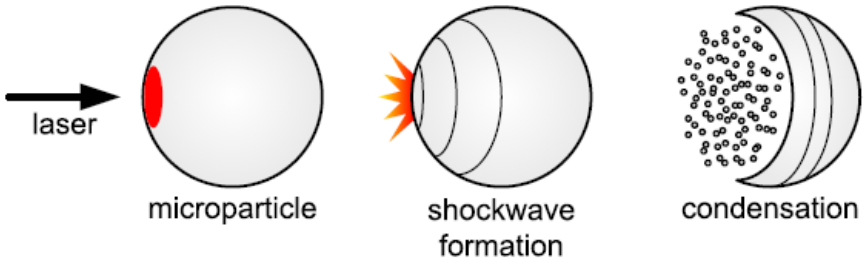


A notable difference between the NPs produced by LAMA compared to other synthesis methods are that they are that there are no organic surfactants necessary to prevent agglomeration because the particles are charged as they are produced. Another relevant aspect of NPs that relevant to this dissertation is that if they are small enough, they do not contain dislocations. Indeed, it has been shown that dislocations are unstable in nanoscale particles, as any dislocation that nucleate within the NP instantaneously migrate towards and then are eliminated at the NP surface [24].

### 3.1.2 Microparticle aerosol feeder

A fluidized powder bed feeder was used to entrain feedstock microparticles (MPs) into a carrier gas and thus create an aerosol of MPs. In brief, the feedstock MPs are first loaded in a conical holder placed above a small fluidization orifice and a carrier gas (He) is passed upwards through the orifice to entrain MPs. A glass settling chamber is positioned above the conical holder and the MP aerosol is collected at the top of the glass chamber. In this way, most of the heavy MP agglomerates present in the feedstock powder resettle before reaching the top of the chamber, and the output MP aerosol contains mostly individual MPs. In addition, the MPs aerosol density can be adjusted by varying the flow passing through the aerosol feeder (see Fig. 3.1 and Table 3.1). The main features of this fluidized bed feeder are that it is capable of generating a high density MP aerosol, and the feed rate is stable over long periods of time. Both of these factors are critical for the research presented in this dissertation; a high density aerosol is necessary to maintain the high NP production rates needed to produce thick films and a uniform feed density in necessary to both produce films of uniform thickness and because variations in aerosol feed rates have been shown to affect the degree of agglomeration of the produced NPs prior to impaction into films. This, in turn, affects the film morphology and film density [23], [29]. Further details on the design of the powder feeder have been discussed previously [29].

The feedstock material used in this work consists of Ag MPs with a size of 1.5 ± 0.2 μm and a spherical geometry (DuPont, formulation P311J).

**Table 3.1: Gas flows used in LAMA process for Ag film deposition using 0.25, 0.5 and 1 mm orifice diameter nozzles (corresponding to increasing NP velocity)**

| | Mass flow rate *(sccm)* | | | Description |
|---|---|---|---|---|
| $Q_1$ | 200 | | | Center flow, carrying MPs to ablation zone |
| $Q_2$ | 0-200 | | | Portion of center flow passing through MP fluidized bed feeder |
| $Q_3$ | 5921 | | | Coaxial flow to maintain a laminar flow regime of MP aerosol in the ablation zone |
| $Q_4$ | 2401 | | | NP aerosol + unablated MPs |
| $Q_5$ | 4720 | | | Excess gas exhaust |
| $Q_6$ | 2209 | | | NP aerosol |
| $Q_7$ | 192 | | | Unablated MPs exhaust |
| | Nozzle diameter *(mm)* | | | |
| | 0.25 | 0.5 | 1 | |
| $Q_8$ | 0 | 6627 | 33135 | Buffer gas |
| $Q_9$ | 2209 | 8836 | 35344 | Supersonic nozzle flow (NP aerosol) |

**Figure 3.2: Schematic of the experimental setup for deposition of Ag films by impaction of nanoparticles, showing all gas flows**

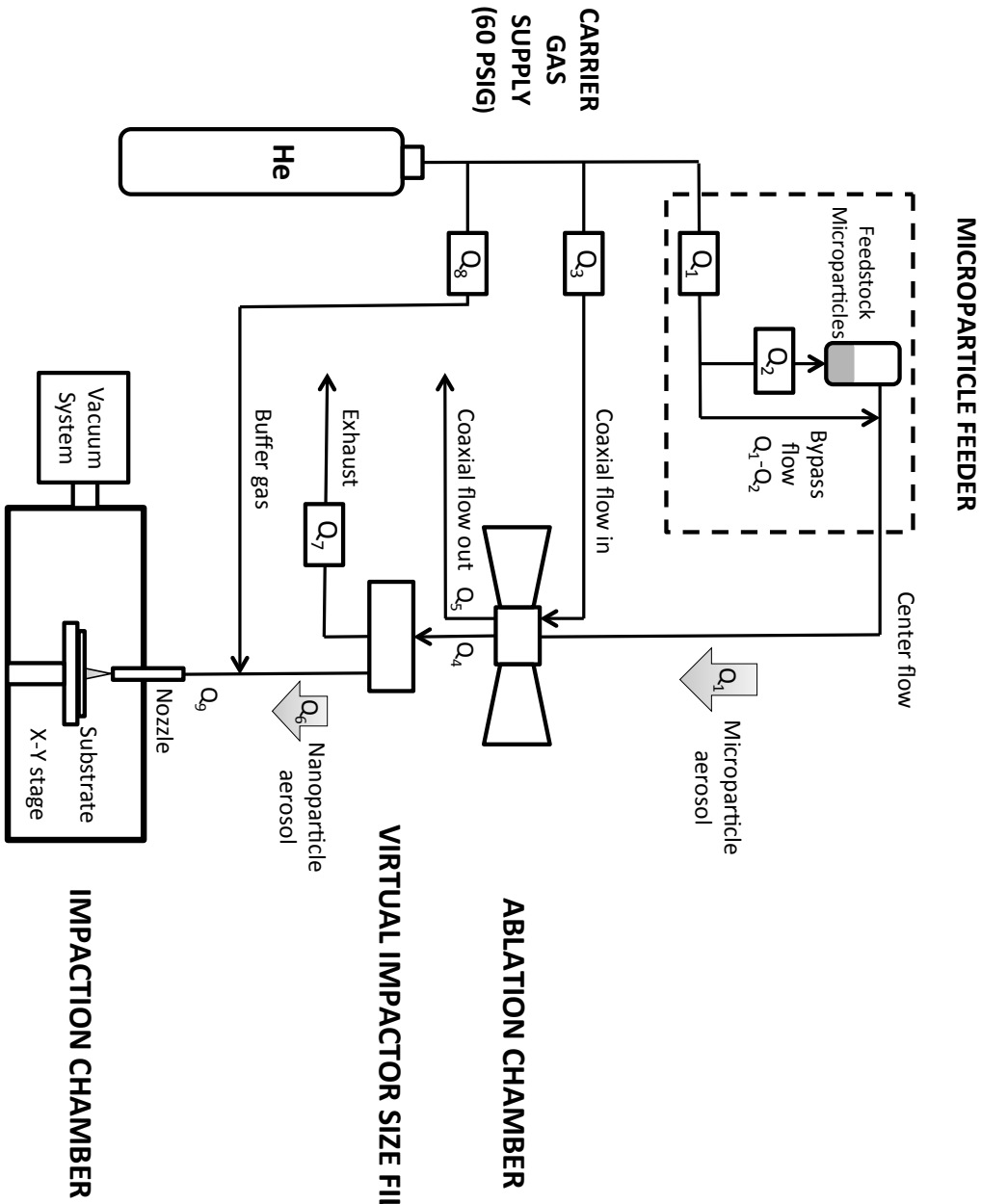

### 3.1.3 Laser ablation chamber and optical system

A pulsed, KrF excimer laser (Lumonics PM-848, Light Machinery, Inc., Ottawa, Canada) with a nominal wavelength $\lambda$ = 248 nm, maximum power output of 80 W, pulse length of 12 ns, is used at its maximum repetition rate of 200 Hz for the laser ablation of the MPs aerosol into a NP aerosol. Two cylindrical lenses of focal lengths $f_1$ = 110 cm and $f_2$ = 14 cm are used to focus the beam respectively horizontally and vertically (see Fig. 3.3). In this work, the laser beam energy was set at 250 mJ and the beam area at the ablation zone was measured to be 0.08 $cm^2$, resulting in a fluence of 3.1 $J/cm^2$, which is well above the breakdown threshold for ablation of Ag MPs (0.8 $J/cm^2$) [28].

**Figure 3.3: Schematic of the optical system used for ablation of micoparticles**

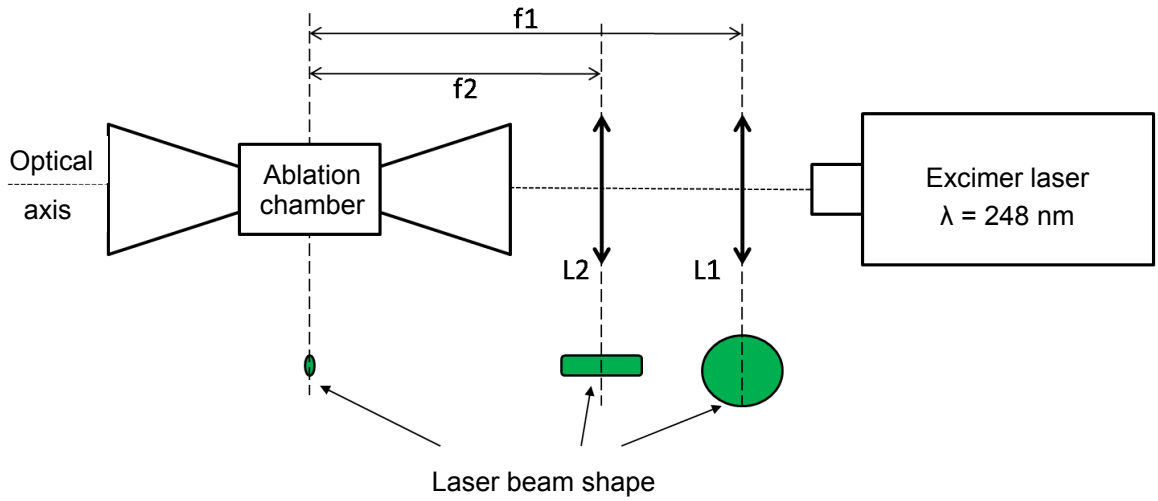


A schematic drawing of the chamber in which the MP aerosol is brought to the focal point of the laser beam is shown in Fig. 3.4. The MPs are fed in the ablation zone through a feed nozzle and then the ablated aerosol is collected through a skimmer. The gas velocity at the ablation zone is calculated so that the laser beam hits the MPs exactly once as they travel across the ablation zone, and the center flow ($Q_1$) is adjusted accordingly, depending on the cross section area of the feed nozzle. In addition, a coaxial

flow ($Q_3$) is passed through a laminator and then around the center flow to contain the center flow so that it is collected through the skimmer rather than expanding inside the chamber during the ablation step. The skimmer collects the center flow as well as part of the coaxial gas. The excess gas is evacuated to a fume hood.

**Figure 3.4 Drawing of the ablation chamber (horn cell) and virtual impactor size filter assembly, adapted from [29]**

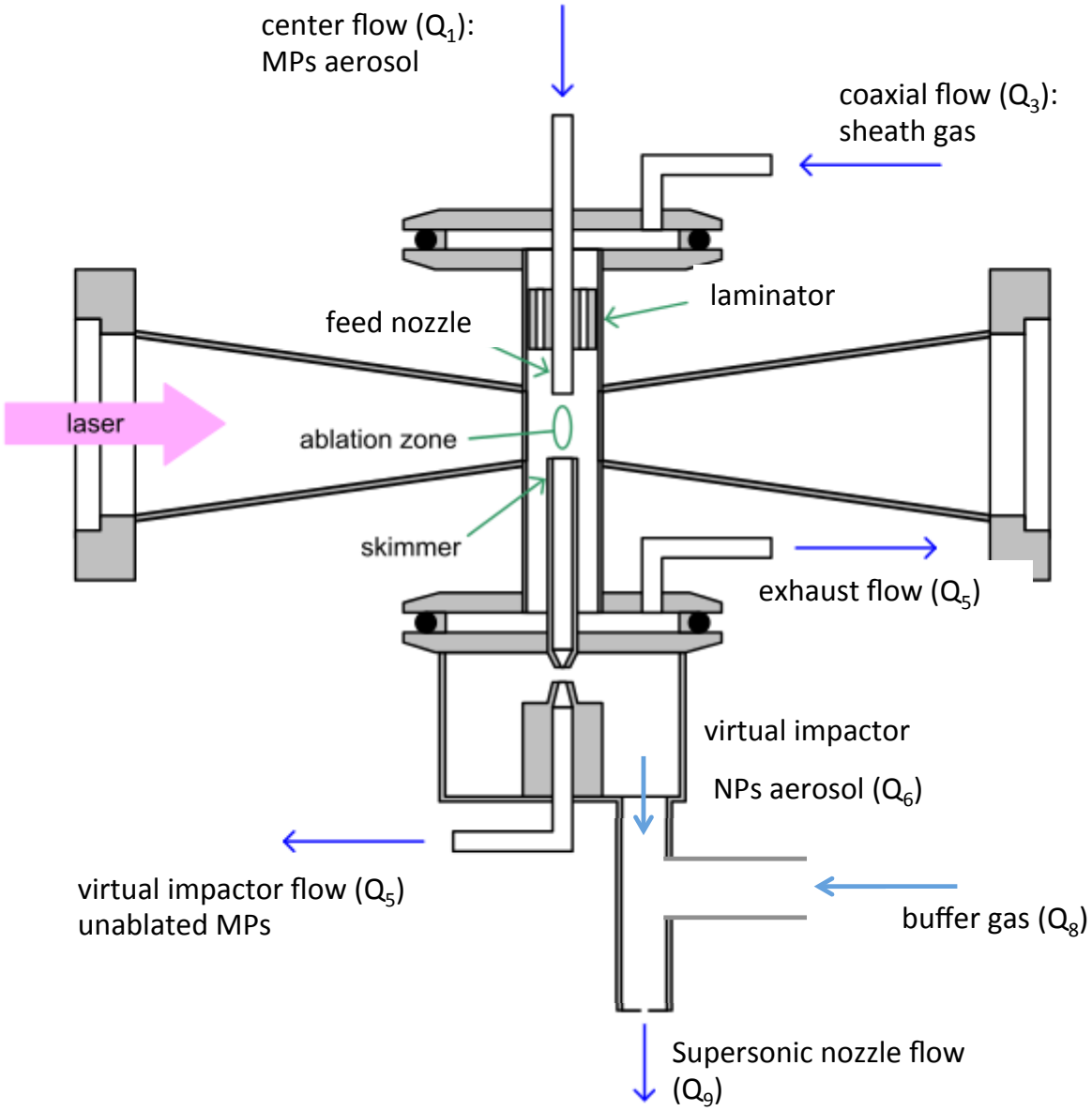

### 3.1.4 Size filtering using a virtual impactor

Downstream of the ablation zone, the center flow contains a mixture of individual NPs, unablated MPs, and NPs that agglomerated following the ablation process. To remove the unablated MPs and agglomerated NPs, a virtual impactor is used. It operates as an aerodynamic size selector, sorting out the oversize particles. The input aerosol is directed towards a conical probe with a small orifice in the center. Only a portion of the aerosol enters this orifice that contains the heavier particles that stay in the inner streamlines of the aerosol [30]. The smaller particles (individual NPs and small NPs agglomerates) contained in the outer streamlines are deflected around the probe and are directed into the direct write chamber. The cutoff size of the virtual impactor is set by the geometry and the ratio between the gas flows; the cutoff size used in this work was set at 500 nm. More details on the design of this virtual impactor can be found in earlier work by Gleason [29].

## 3.2 Direct writing of silver films

### 3.2.1 Acceleration of NPs

After the filtering of the NP aerosol, NPs are accelerated by expansion of the carrier gas through a flat-plate nozzle using a pressure differential. While the aerosol of NPs is created under atmospheric pressure, a vacuum is pulled on the downstream side of the nozzle. Huang *et al.* [3] studied the gas dynamics during acceleration and calculated the velocity reached by the carrier gas and by the NPs. They reported that for large pressure differentials (as it is the case in the current LAMA setup), the maximum velocity reached by the carrier gas after the jet expansion can be calculated and depends only on

the nature of the gas and the geometry of the nozzle. Then, they developed a model to predict the velocity reached by the NPs, taking into account the drag force applied by the gas on NPs. The calculations are not straightforward since the gas velocity and density vary as the gas expands and so does the drag force. Nevertheless, the partial differential equation that describes the NP speed can be solved numerically and the maximum speed reached by the NPs is found to depend on the NP diameter, the nature of the carrier gas, and the nozzle diameter. For example, higher gas and particle velocities are obtained in He than in heavier gasses such as Ar, assuming the particle size can be kept constant. Note however that it is not possible to vary only the impaction velocity or particle size by changing gas types. Changing the gas type influences both the particle size and impaction velocity [2].

An alternative to influencing the particle velocity by instead varying the nozzle geometry is explored here. This method has the advantage that the particle velocity can be altered, independent of the particle size. In these experiments the nozzle aspect ratio is fixed at 1:1 so that the nozzle diameter and plate thickness are equal. Using He as a carrier gas, the maximum predicted velocity reached by a typical 5 nm particle is close to 1000 m/s upon impaction onto the target substrate for a 0.25 mm nozzle (corresponding to a kinetic energy of 0.6 eV/atom). The calculations suggest that the deposition velocity can be increased to 1200 m/s for a 5 nm particle by using a 0.5 mm nozzle (0.8 eV/atom) and up to 1330 m/s with a 1 mm nozzle (1 eV/atom). Predictions of impaction velocities for a range of particle sizes and gas types are shown in Fig. 3.4. These calculations justify increasing the diameter of the flat-plate nozzle to achieve higher impaction energies and therefore the potential to form a broader range of film microstructures. To

achieve this, the vacuum line connecting the vacuum system (mechanical pump and roots blower) to the deposition chamber was improved to maximize its conductance and make possible the use of 0.5 mm and 1 mm nozzles while maintaining a pressure in the deposition chamber that is low enough to maintain choked flow through the nozzle orifice. In addition, NP deceleration in the bow shock forming over the substrate is discussed in chapter 6, section 3, and especially the influence of nozzle-to-substrate distance on the deceleration of NPs.

**Figure 3.5 : (a) Influence of accelerating nozzle length and particle size on the final velocity reached by impacting Ag NPs (courtesy Dr. Michael F. Becker)**
**(b) Same data shown for kinetic energy rather than velocity for easier comparison with MD simulations**

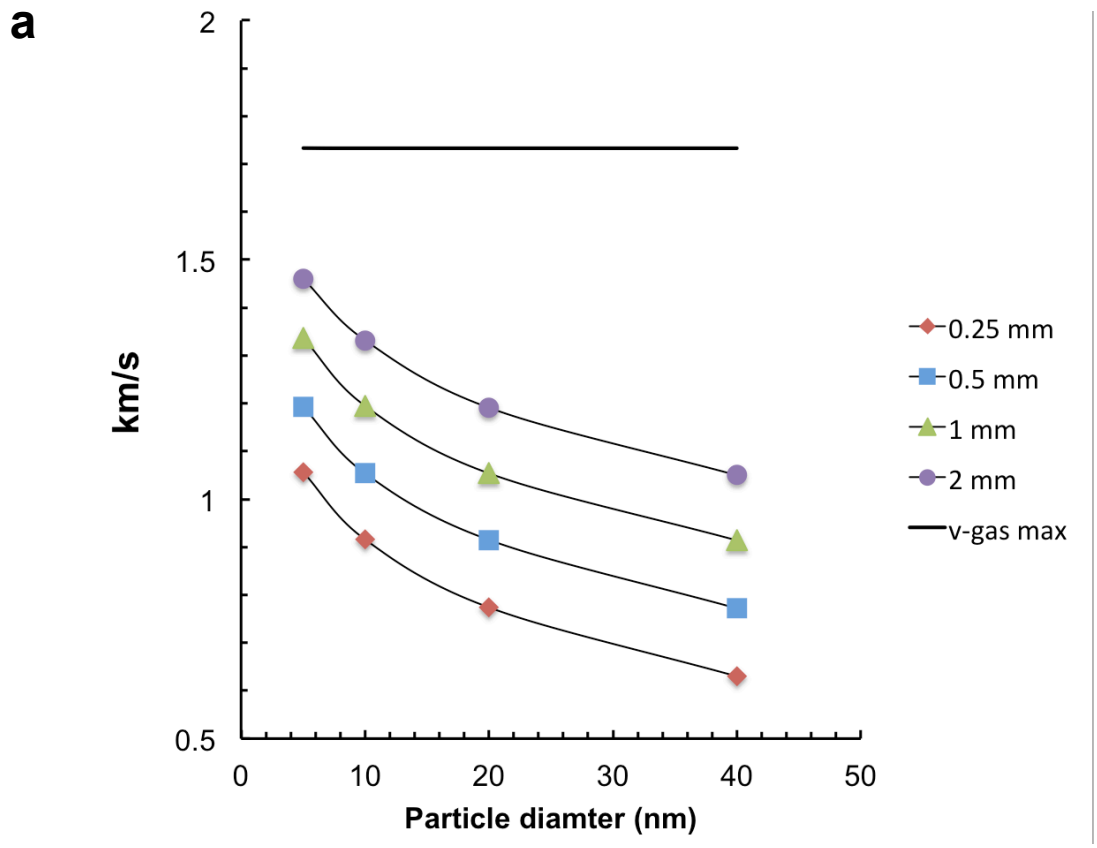

**Figure 3.5, continued**

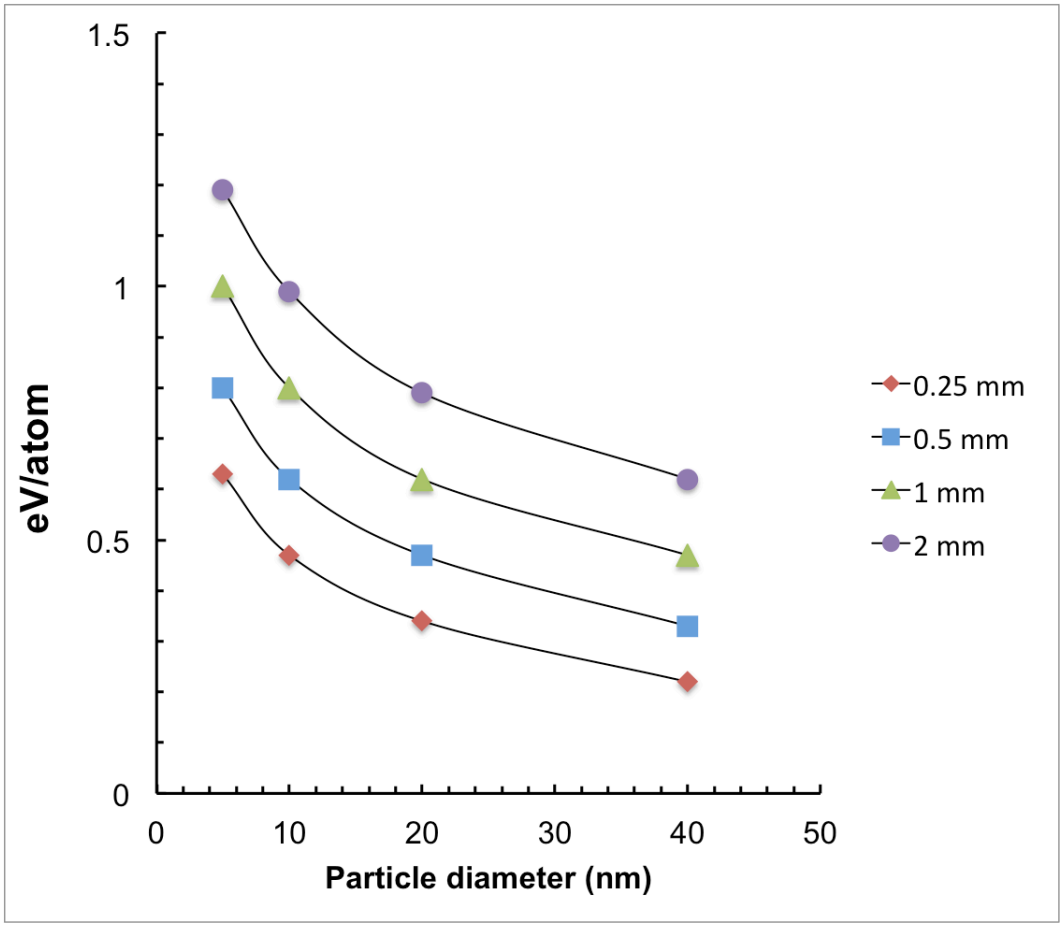


### 3.2.2 Computer-controlled translation stage

A X-Y translation stage was placed in the deposition chamber underneath the flat-plate nozzle for deposition of patterned films from the NP jet. The motion in X and Y directions was made possible by 2 stepper motors (Model #37443-05-910, Haydon Kerk Motion Solutions, Inc., Waterbury, CT) and suitable control electronics (IM483, IMS Inc., Marlborough, CT). A computer program written in National Instrument's LabVIEW© was combined with a National Instruments digital input/output module to send the proper command signals to the motor's control electronics. The LabVIEW©

program was developed to write shapes from text files containing the motion instructions (speed, distance, direction) for more flexibility and simplicity. This allowed control of the stage motion, in order to deposit films with the desired pattern and thickness (see Fig. 3.5). The stage has a resolution of about 10 µm but the actual pattern resolution is instead limited by the width of the NP jet (50 µm to 250 µm depending on nozzle diameter and nozzle-to-substrate distance). The motion range is currently limited to dimensions of 2.3 cm × 2.3 cm but there are otherwise no obstacles in scaling up the system to deposit films with larger areas.

**Figure 3.6:Block diagram of the stage motion control system. A LabVIEW program using a state machine architecture was implemented to manage deposition patterns**

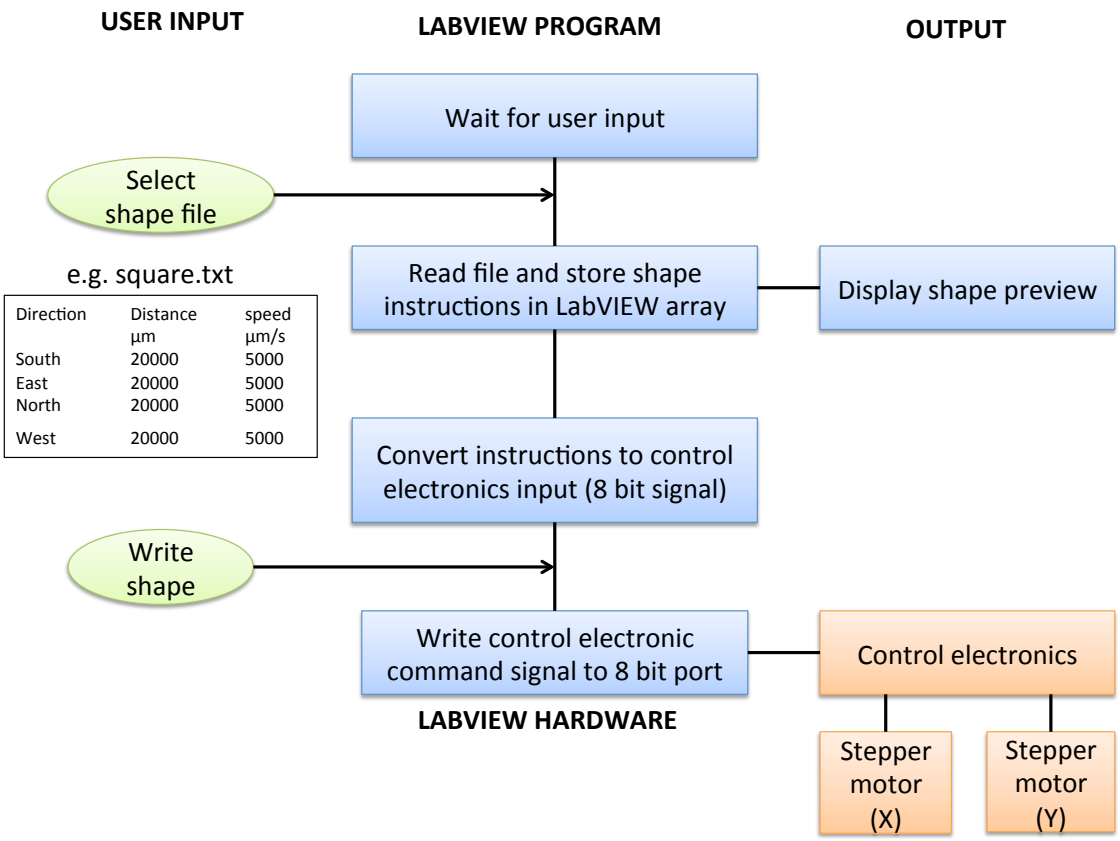

# Chapter 4: Experimental procedures

## 4.1 Microstructure analysis by transmission electron microscopy

### 4.1.1 Deposition of nanoparticles on TEM grids

To investigate the morphology of individual nanoparticles and small clusters of nanoparticles created by the LAMA process (Chapter 5), TEM grids with a Formvar® support film (Model 200M-TH, Ted Pella Inc., Redding, CA) were clamped on a flat substrate and then NPs were deposited via the LAMA process. A large nozzle-to-substrate distance (typically equal to 10 times the nozzle diameter) was used in order to minimize the pressure of the gas jet on the support films and avoid their destruction. These samples were deposited using a stage translating speed fast enough (typically 5 mm/s) to avoid the formation of a continuous film, e.g. so that individual particles could still be easily discerned on the TEM grid.

### 4.1.2 Preparation of electron-transparent cross-sectional samples

In order to investigate the microstructure of LAMA-deposited Ag films, cross sectional samples of the films that were electron transparent were prepared using a focused ion beam (FIB) technique. The instrument used was a FEI Strata DB235 SEM/FIB (FEI, Hillsboro, OR). The thickness required to achieve electron transparency is less than 100 nm [31], which makes the preparation of cross sectional samples challenging. As illustrated in Fig. 4.1, stubs were prepared by assembling a half copper aperture grid (Product #1GC42S, Ted Pella Inc., Redding, CA) and a rectangular piece of 10 μm thick shim stock steel using epoxy (M-bond 610, Ted Pella). This epoxy was

chosen for both its strength and its stability under the electron beam, preventing excessive carbon build-up on the sample during the TEM observations. Shim stock stainless steel was chosen as the substrate material for the films because of good adhesion of LAMA-produced NPs on this material, and because it was available in very thin sheets. The thin substrate materials minimized the time required to carve out electron transparent membranes using the FIB (see sample geometry in Fig. 4.1.c). To obtain a flat edge, the steel rectangular pieces were made by gluing a piece of shim stock stainless steel between two flat silicon pieces using wax (CrystalBond, Ted Pella), then a precision saw (ISOMET, Buehler, Lake Bluff, IL) was used to cut 1 mm × 2.5 mm rectangles from the stack. Ag films were then deposited on the cross section of the stainless steel substrate using the LAMA process. For film deposition under the NP jet, the stubs were clamped on a FIB precision grid holder (Model #15466, Ted Pella) that was mounted on the translation stage in the LAMA apparatus. The use of the precision FIB grid holder ensured that the surface on which the films was deposited was perpendicular to the NPs jet, and also minimized the handling of the fragile samples after deposition. The FIB grid holder can be placed directly in the FIB instrument for carving out a transparent electron membrane without removing the sample from the holder. Fig. 4.2 shows an electron-transparent window of a 2 μm thick Ag film deposited on the stainless steel substrate, showing good contrast between both materials.

**Figure 4.1: TEM cross-sectional sample preparation**

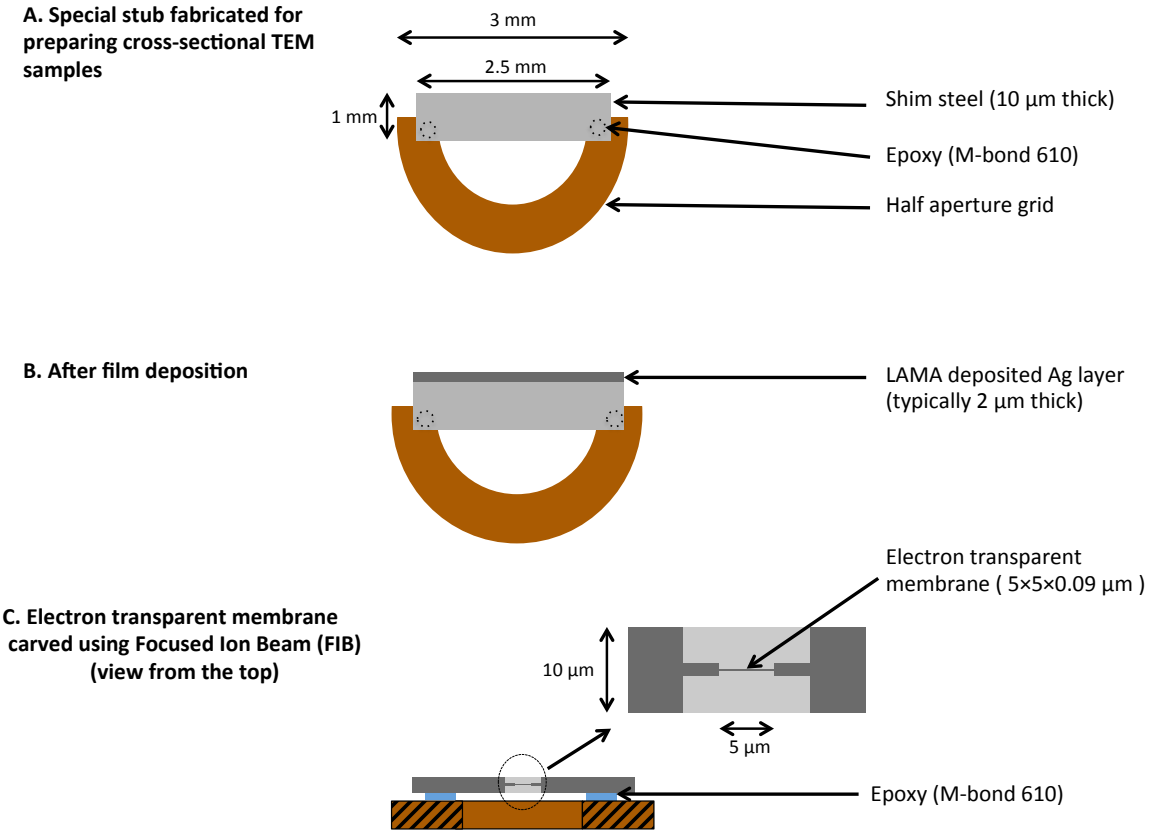

**Figure 4.2 SEM micrograph taken in the FIB of an electron transparent cross-sectional sample of silver film deposited on stainless steel using the LAMA process (tilted view)**

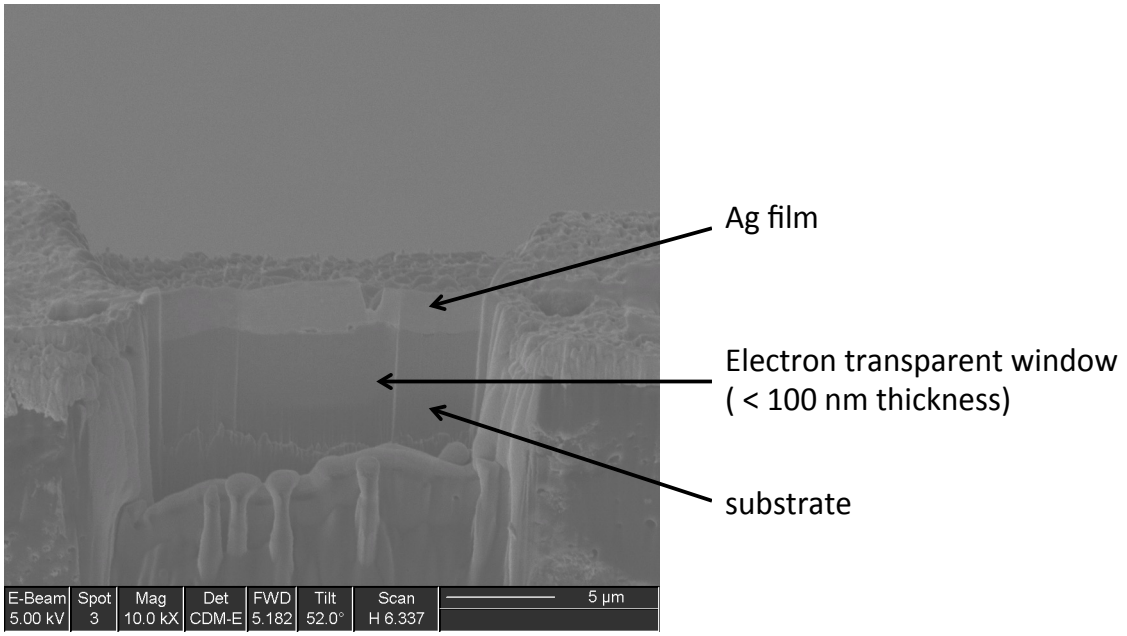


### 4.1.3 TEM observation conditions

A transmission electron microscope (TEM) (2010F, JEOL, Tokyo, Japan) was used to perform high resolution imaging (HRTEM), bright field imaging and dark field imaging. HRTEM images were obtained easily from NPs and NPs clusters deposited on TEM grids. However, it was often not possible to perform HRTEM on cross-sectional samples since they were too thick. To reveal the grain morphology in thick samples that contained multiple grains within the sample cross-section, dark field imaging was used. A bright spot in the diffraction pattern of the studied area was selected so that only grains with the corresponding orientation appear bright in the image. This provided very good contrast of the selected grains even in thick samples.

Selected area diffraction (SAD) was performed on regions of interest within the cross sectional samples to determine the degree to which a preferred crystallographic orientation arose during film growth during deposition using the LAMA process. With the microscope used in this work, the smallest area for which SAD could be performed had a 100 nm radius.

### 4.1.4 Energy-dispersive X-ray spectroscopy

Energy-dispersive X-ray spectroscopy (EDS) was performed to identify the elements present in different areas of the TEM samples: Ag film, stainless steel substrate and interface layer. To compare the composition of different regions within a same sample, EDS spectra were obtained with a standardized acquisition time (15 s) and electron beam size (100 nm).

## 4.2 Grain size measurements using X-ray diffraction

### 4.2.1 Sample preparation and data acquisition

Films with a 1 cm × 1 cm area (similar to the ones shown in Fig. 6.3) were deposited on glass substrates. An X-ray diffractometer (MiniFlex 600, Rigaku, Tokyo, Japan) with a Cu Kα X-ray source was used to obtain powder diffraction patterns (θ-2θ plots) with a typical scanning speed of 0.25° /min and 0.01° step size. The 2θ scanning range was 35°-120° and included {111}, {200}, {220}, {311}, {222} and {400} peaks.

### 4.2.2 Sources of peak broadening

In X-ray diffraction patterns, several factors contribute to peak broadening. In this section, we discuss briefly the effects of instruments broadening, size broadening and microstrain broadening.

To account for the instrument contribution to peak broadening, a θ-2θ plot of a standard annealed sample of lanthanum hexaboride ($LaB_6$) with negligible peak broadening due to crystal strain and grain size was acquired (The sample was prepared by Dr. Steve Swinnea). A Lorentzian fit of the peaks was then obtained and the full width at half maximum was plotted against 2θ. A parabolic model was then obtained, as shown in Fig. 4.3. This instrumental broadening model was used to remove the instrument contribution from the observed peak of LAMA-deposited Ag samples.

The finite size of the diffracting crystallites also causes peak broadening. This effect is measurable for grains < 100 nm and can be estimated using the Scherrer formula [32]:

$$B_{size} = \frac{K \cdot \lambda}{L \cdot \cos(\theta)} \qquad \textbf{(4.1)}$$

Where K is a constant (0.8 to 1.39, chosen equal to 0.9 in this work), λ is the wavelength of the incident X-ray beam (for Cu $K_\alpha$ radiation, λ=0.15418 nm) and L is the size of the diffracting domains in the direction of parallel planes of {hkl} corresponding to the Bragg angle θ.

Peak broadening occurs when microstrain (strain arising from point or line defects), ε, is present in the material, and strain broadening ($B_{strain}$) can be estimated using the Stokes-Wilson formula [32]:

$$B_{strain} = C \cdot \varepsilon \cdot \tan(\theta) \quad \textbf{( 4.2 )}$$

Where C is a constant (C = 8/ π when the full width at half maximum is used to define the broadening B, expressed in radians).

### 4.2.3 Data analysis

Jade 10 software (MDI, Livermore, CA) was used to extract the peaks from the raw data, remove the background signal and remove the Cu $K_{\alpha 2}$ component from the peaks. After this initial data processing, the observed peaks were fitted using the curve-fitting tool in Matlab® (version R2014a). A Lorentzian model was used to model the intensity of observed peaks:

$$I(x) = I_{hkl} \cdot \frac{(0.5 \cdot fwhm)^2}{(0.5 \cdot fwhm)^2 + (x - x_0)^2} \quad \textbf{(4.3)}$$

Where I is the measured intensity, x is equal to twice the scattering angle (2θ) and is expressed in radians. $I_{hkl}$ is a fitting parameter representing the maximum peak intensity of the {hkl} reflection. fwhm is a fitting parameter equal to the width of the peak at half its maximum, and $x_0$ is the position of the peak.

After removal of the instrument contribution, the size and strain contribution to broadening were separated using a Williamson-Hall plot [33] , that utilizes the different

dependence in θ of $B_{size}$ and $B_{strain}$. In the Williamson-Hall method, $B \times \cos(\theta)$ is plotted against $\sin(\theta)$ for the peaks available in the diffraction pattern, where B is the total peak broadening ($B = B_{size} + B_{strain}$). This assumes that both broadening effects lead to a Lorentzian-broadened profile and therefore the FWHM of the convoluted profile (observed peak) is the sum of size- and strain-induced broadenings. If the strain and size effects are independent of crystallographic directions, a straight line arises from the Williamson-Hall plot. The size is deduced from the Y-intercept and the strain from the slope of the line.

**Figure 4.3: Model used for instrumental contribution to peak broadening for 2θ in the range [30° - 140°]. The data points represent measured instrument peak broadening using a Lorentzian fit, and the equation is a parabolic fit to the data.**

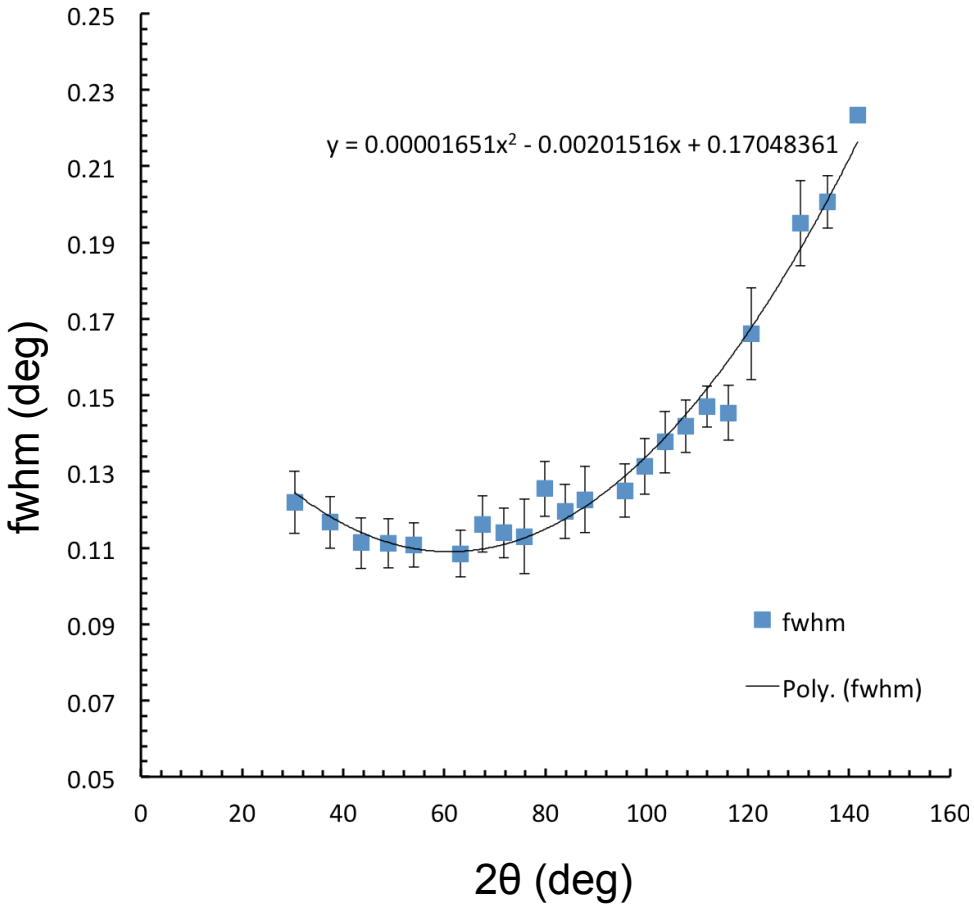


## 4.3 Texture analysis

To investigate the texture of LAMA-produced silver samples and any influence of deposition substrate on texture, pole figures were obtained from samples deposited on soda lime glass (amorphous) and a {100} silicon wafer (monocrystalline). Circular films with a 1.5 cm diameter and thickness of approximately 5 μm were deposited.

The diffractometer used for pole figure analysis was an Ultima IV (Rigaku). The diffracted intensity of {200} planes (2θ = 44.27°) was measured for all orientations of the

film relative to the X-ray beam to investigate any preferred orientation of the {200} planes relative to the surface of the deposition substrate. In the spherical coordinate system relative to the sample, the scanning ranges for polar angle (α) and azimuthal angle (β) were [0°-90°] and [-180° 180°], respectively, using an α-axis step size of 2°, and a β-axis step size of 3°.

For texture analysis, pole figures were generated from the raw data using Rigaku's PDXL software.

## 4.4 Molecular dynamics simulation details (simulations are courtesy of Tushar V. Chitrakar and Dr. Michael F. Becker)

Molecular dynamics (MD) simulations were conducted using LAAMPS [34] run on the Lonestar Linux cluster at the Texas Advanced Computing Center (TACC) at The University of Texas at Austin. Visualizations were conducted off-line using VMD for Windows platforms (developed by the Theoretical and Computational Biophysics group at the Beckman Institute, University of Illinois at Urbana-Champaign).

The rectangular simulation volume base was 60 x 60 lattice constants (LC, for silver, LC= 0.409 nm) and 80 LC in the z direction or NP impaction-velocity direction. The boundary conditions in all three dimensions were periodic. The silver atoms within the larger NP had their z-direction momentum fixed to zero during the simulation so that the NP impaction momentum would not move the atoms out of the simulation volume. There was no thermal boundary condition set for the substrate base; and for periodic boundary conditions, this would be a vacuum interface.

The tabulated potential function for silver, Ag.eam.alloy, was downloaded from the NIST Interatomic Potentials Repository Project [35]. The silver atoms in the substrate and impacting NP were allowed to thermalize at 300 K for 30-40 ps, depending on the simulation system size, before the NP was set in motion in the -z direction towards the substrate.

For thermalization and impaction, the NPT integrator was used with a 1 fs time step. This isothermal-isobaric integrator was configured to incorporate a thermostat to a 300 K bath with a time constant selected for the impaction phase to give reasonable cooling times for the substrate. This method for incorporating thermalization in the simulation

was used because more traditional methods such as enforcing a heat sink at the bottom surface gave unreasonably fast cooling because the surface was too close to the sink. Using the NPT integrator method, the dynamic temperature behavior of regions of the impacting NP and adjacent substrate was found to be independent of the thermostat damping rate. The overall cooling of the sample volume was cooled by 1/e in ~0.5 ns for the selected thermal damping time for the npt integrator of 100 ps. This generally resulted in complete thermalization of the particle/substrate in about 100 ps.

Diagnostic temperatures were obtained for multiple groups of atoms that were defined by their initial region within the substrate and NP. These data were generally collected at 2-10 ps intervals. Complete atom configurations for use with visualization software were dumped to text files for later analysis at longer intervals of 2 to 50 ps depending on the length of the run and desired degree of time resolution.

# Chapter 5: Study of atomic-scale mechanisms occurring during impaction of nanoparticles

In this chapter, we study the mechanisms occurring when Ag nanoparticles (NPs) impact at high velocities. Ag NPs were produced using the LAMA process and then accelerated using a pressure differential, as explained in detail in Chapter 3. The goal of this chapter is to understand the mechanisms that occur within a single NP upon impaction that causes it to stick to the substrate, or to an already deposited NP layer. Mechanisms that cause plastic deformation in fcc crystals as small as a few nanometers, as well as other possible matter flow mechanisms that occur when such small crystals are subject to very high strain rates (melting, amorphization, followed by crystallization) are crucial to explain experimental observations, but they are not yet well understood. This chapter provides representative experimental observations, as well as a computer simulation of NP impaction, and both are used to discuss the mechanisms of deformation that occur upon NP impaction.

In the first section, experimental observations of supersonically impacted silver NPs are presented. High-resolution TEM (HRTEM) observations were conducted, where lattice fringes of the crystal, representing columns of Ag atoms interacting with the electron beam, are visible. This gives insight to the deformation mechanisms that occurred during impaction. Different impaction regimes are observed: non-epitaxial

deposition, fully epitaxial deposition, and partially epitaxial deposition. The presence of planar defects (twins or stacking faults) is discussed.

Special consideration is given to the last TEM micrograph (Fig. 5.5), which shows a 13.6 nm NP that impacted onto a 32 nm NP at a calculated speed of 860 m/s. This micrograph is used to compare to a molecular dynamics (MD) simulation (courtesy Tushar V. Chitrakar) in order to study the mechanisms that led the final microstructure; and this simulation is described in the second section of this chapter. Mechanisms are identified and discussed, including matter flow, amorphization and recrystallization. In the conclusion section of this chapter, the advantages of coupling HRTEM observations with computer simulations to understand the phenomenon of NP impaction is discussed. This leads to an inventory of possible matter flow and deformation mechanisms occurring during impaction of NPs. Finally, how this knowledge can be used to achieve material deposition with a controllable microstructure is discussed.

## 5.1 TEM observations

### 5.1.1 Non-epitaxial deposition

During high resolution TEM investigations of Ag NPs impacted on TEM grids, multiple cases of non-epitaxial deposition were observed. The term non-epitaxial is used when the impacted NP and the material on which it impacts produces different crystallographic orientations after the impaction event. Figs. 5.1 and 5.2 illustrate two cases of particle impaction in this deposition regime.

In Fig. 5.1.a, a spherical NP is still clearly visible after impacting onto a previously deposited NP. The lattices fringes in the TEM image show that there is no

continuity of the crystallographic planes across the original boundary between the two NPs, indicating that this was a non-epitaxial deposition. A closer look at the crystallographic arrangements within the spherical NP (Fig. 5.1.b) shows periodic changes in contrast that are consistent with planar defects (stacking faults) that are indicated by white arrows in Fig. 5.1.b. The fast Fourier transform (FFT) of this region (Fig. 5.1.c) is also consistent with what is expected for a fcc crystal with a high density of stacking faults [31]. These stacking faults could have been created during the NP formation process by laser ablation, and therefore be present prior to the impaction event, or could have been caused by the impaction event either due to plasticity (deformation twinning) or due to rapid crystallization following amorphization (annealing twins). Plasticity mediated by planar defects nucleation and motion has indeed been reported in fcc nanocrystals in recent studies [36].

Another case of non-epitaxial deposition is shown in Fig. 5.2. A 12 nm NP on the left-hand side of the TEM micrograph has impacted onto a larger NP. In this case, the smaller NP consists of a number of small grains (5 nm). It is interesting that, in contrast to the epitaxial regime where the grain size is expected to increase upon impaction, in this regime, the grain size of impacted particles is reduced relative to the original NP size.

**Figure 5.1: (a) HRTEM micrograph showing non-epitaxial deposition of Ag NP (b) Closer view of region highlighted in (a), white arrows indicate stacking faults (c) FFT of region highleted in (b), consistent with of fcc crystal with a high density of stacking faults, with imperfect stacking of the {111} planes**

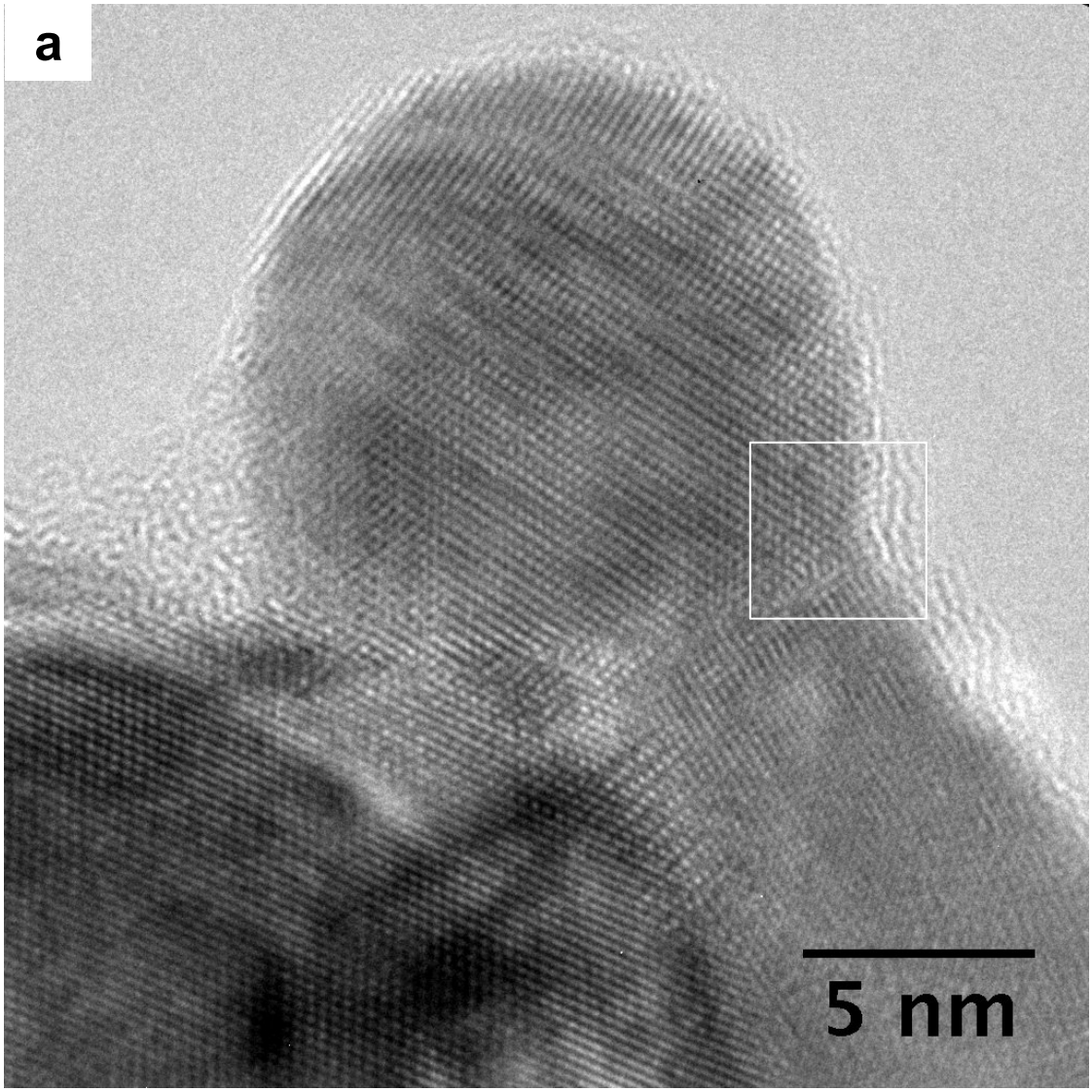

**Figure 5.1, continued**

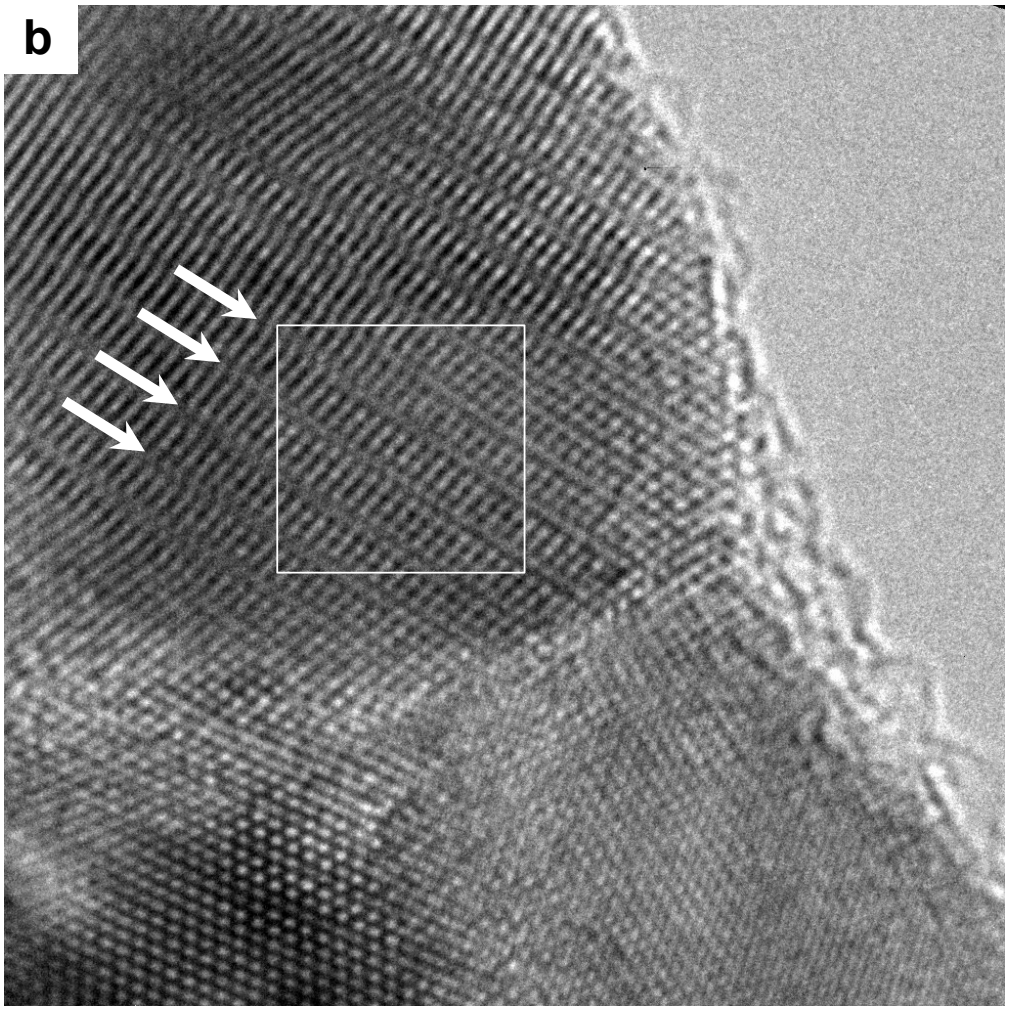


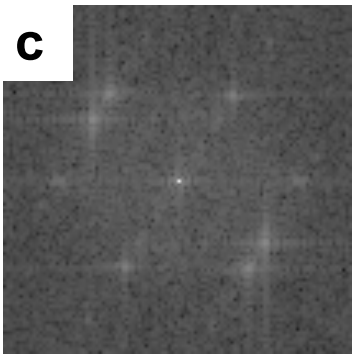

**Figure 5.2: HRTEM micrograph showing non-epitaxial deposition of Ag NP**

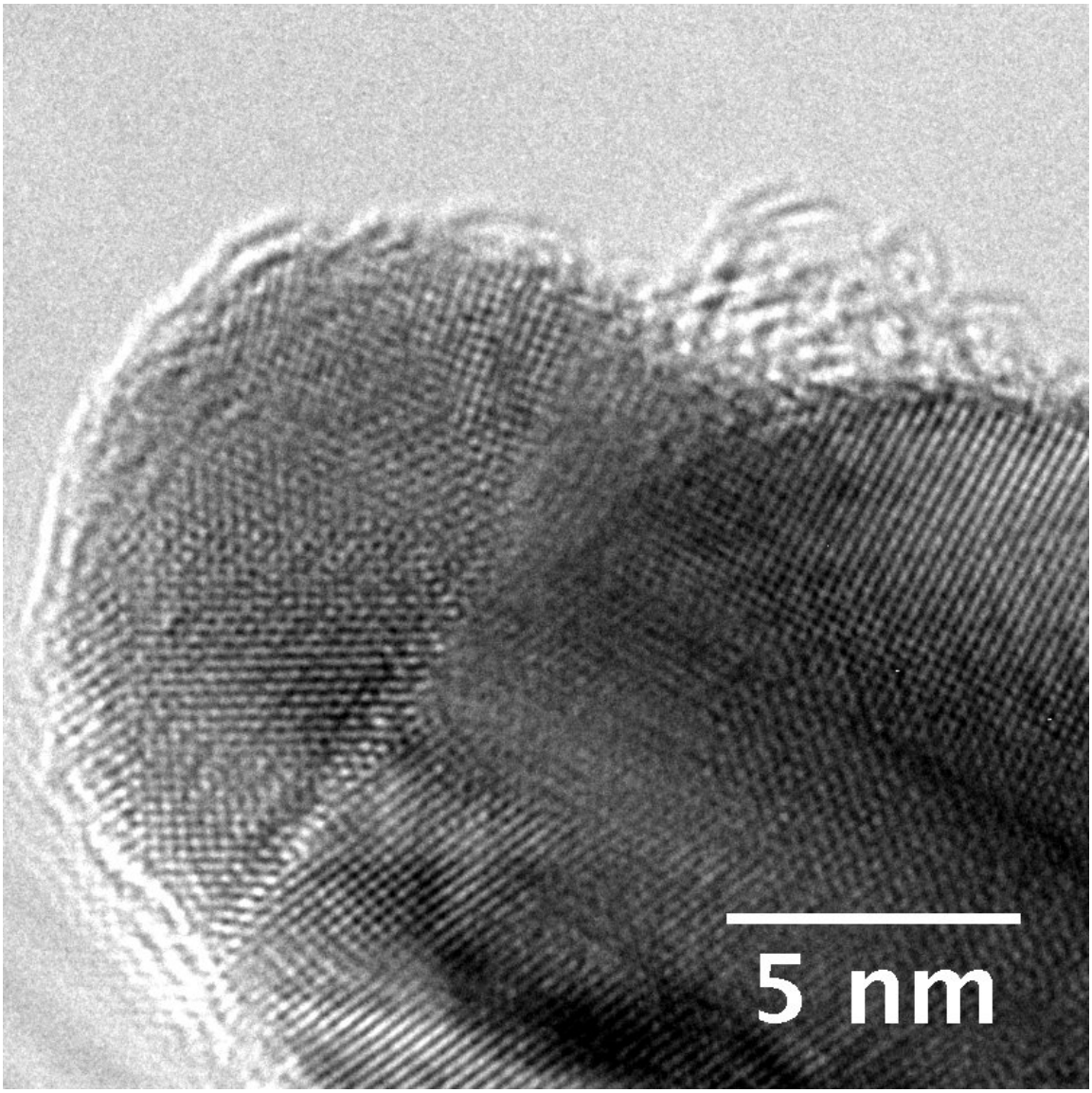


### 5.1.2 Fully epitaxial deposition

Two HRTEM micrographs (Fig. 5.3 and Fig. 5.4) are shown where epitaxial deposition occurred. In these micrographs, the crystallographic orientation of the impacting NPs aligns fully with the crystallographic orientation of the already deposited NPs. In Fig 5.3.a, a 8.5 nm NP is shown in the upper right corner of the micrograph. The

lattice fringes of the crystal are continuous between the NP and the material on which it impacted. In this case, no defects are observable within the grain, and the epitaxial impaction of the 8.5 nm particle resulted in an increase in grain size relative to the size of the NPs involved in the impaction.

Fig. 5.4.a shows a case where te impaction of a NP (at the top left corner of the micrograph) was epitaxial and also leads to an increase in grain size relative to the size of the impacting particles. The location of the original interface between the two NP involved in the impaction event can be estimated based on the surface curvature at the top left of the micrograph, and we can see that the lattice fringes of the grain extend beyond the initial positions of this interface. In the grain highlighted in Fig. 5.4.b, we observe a high density of stacking faults. The fact that the grain size is larger than the initial impacting NP suggests that these stacking faults were produced during crystallization and occurred either during or after the impaction. The conditions determining whether a defect-free crystal or a crystal with a high density of stacking faults forms during crystallization from an amorphous state is not well understood. However, the formation of stacking faults during crystallization is common in Ag due to its low stacking fault energy (SFE = 20-30 $mJ/m^2$) [37].

In the two above examples, it was possible to identify cases of epitaxial deposition because some of the features of the original NPs in the final microstructure are visible (in particular, the surface curvature). However, this is not always the case, particularly for smaller particles (<10 nm) that impact epitaxially. When this occurs the particles likely sinter into a single grain with no discernable features that identify the morphologies of the original particles. At least three factors indicate that smaller NP tend

to land epitaxially, even though this has not been directly observed in the TEM: (1) MD simulations conducted previously predict that smaller NPs are more likely to impact epitaxially [6] (2) During supersonic acceleration of the LAMA-produced NPs, smaller NPs get accelerated to higher speeds (Fig. 3.5), a factor that also favors epitaxial deposition [6] and (3) according to previous measurements of the size distribution of Ag NPs in LAMA-produced aerosols made from individual NPs [2], [29], a large portion of the aerosol consists of NPs in this size range. The fact that few of such NPs were observed in deposited films under the TEM is consistent with the hypothesis that they have sintered and formed larger grains.

**Figure 5.3 : HRTEM micrograph showing epitaxial deposition of Ag NP**

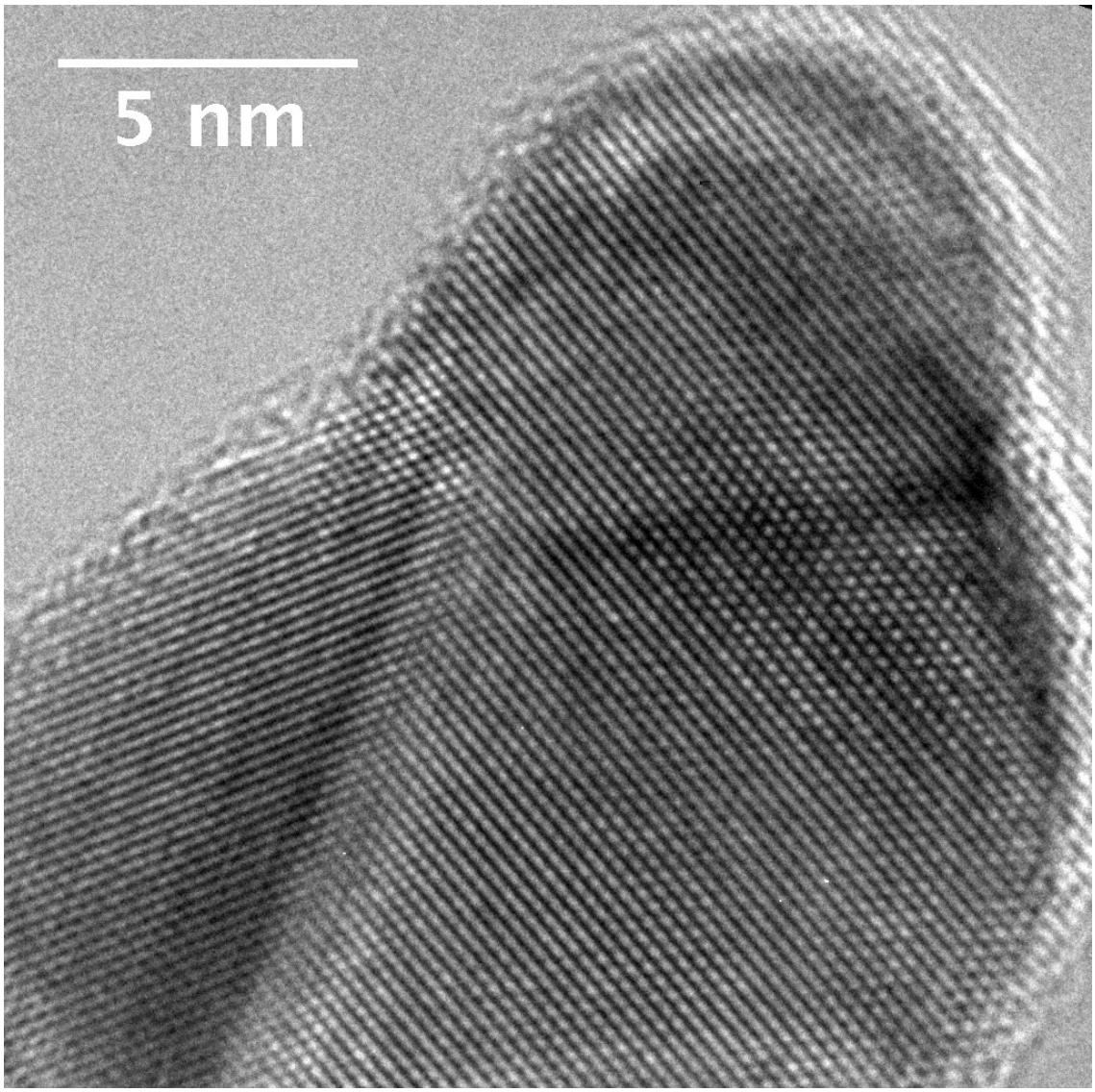

**Figure 5.4 : (a) HRTEM micrograph showing epitaxial deposition of Ag NP, leading to an increase in grain size compared to NP size. Note the high density of stacking faults. (b) Higher magnification view**

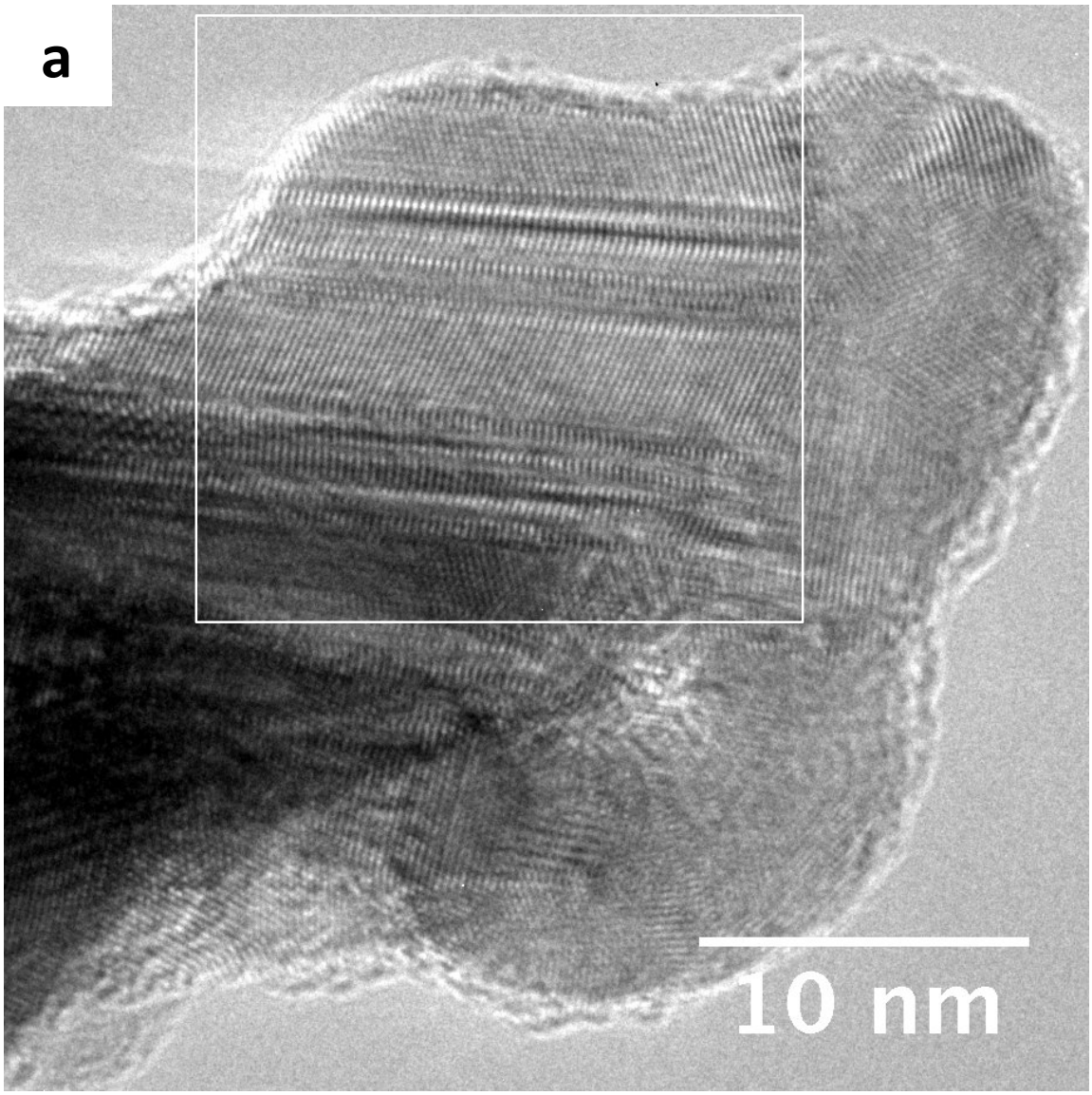

**Figure 5.4, continued**

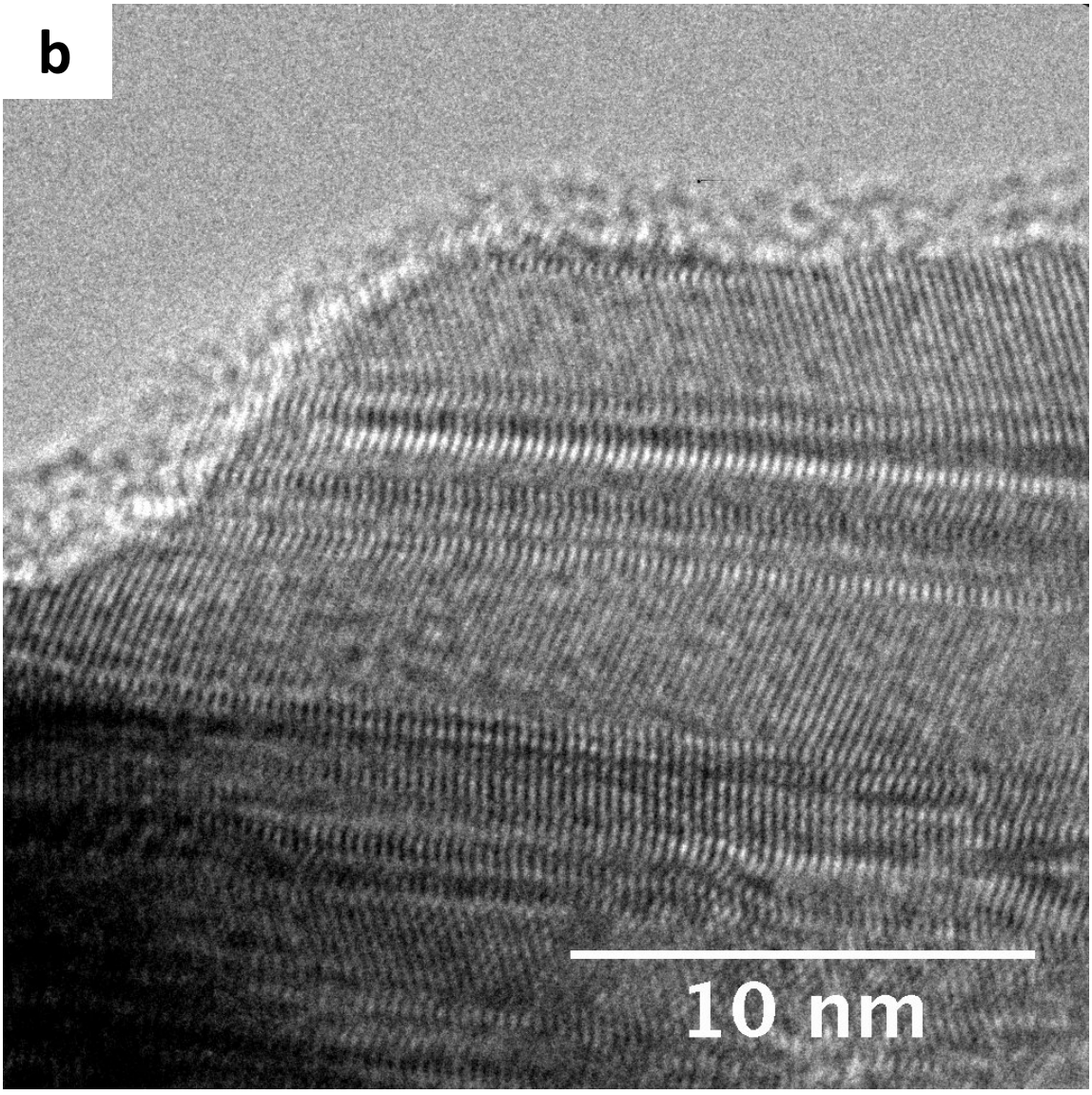


### 5.1.3 Small NP impacting on larger NP

In Fig. 5.5, a high resolution TEM micrograph is shown of a 13.6 nm spherical NP that impacted onto a larger 32 nm NP. The velocity of impaction can be calculated from the size of the particle using Fig. 3.5 and was approximately 860 m/s. The methodology to calculate the NP velocity is explained in previous work [3]. Both particles are observed near the <100> zone axis (orientation of the electron beam relative to the crystal), as

suggested by the FFT of an undisturbed region in the larger particle (Fig. 5.5.a). From the non-spherical shape of the smaller particle it is apparent that this NP experienced a large deformation upon impaction. This is in contrast to the larger particle, which remained nearly spherical and therefore relatively undeformed. Dark bands, perpendicular to the direction of impaction, are visible in the micrograph. The dark bands are likely to be stacking faults that appear as bands because the HRTEM micrograph was taken slightly off the ideal zone axis to observe stacking faults in fcc. In addition, previous analysis of LAMA deposited Ag NPs taken in a perfect zone axis [45] showed a high density of stacking faults.

The sample shown on Fig.5.5 was chosen as a representative example on which to carry out a series of detailed computer simulations of NP-on-NP impaction, in order to study the deformation mechanisms, defect evolution and resulting microstructure that occurs during and following impaction of NPs.

**Figure 5.5 : (a) HRTEM micrograph of small NP impacted on larger NP, FFT of highlighted region is shown in the inset. The interplanar spacings can be measured from the spots in the FFT.**
**(b) & (c) higher magnfication views showing planar defects. In (c), the spacings between the lattice fringes has been measured to be close to close to 205 pm, consistent with spacings of {200} planes in Ag.**

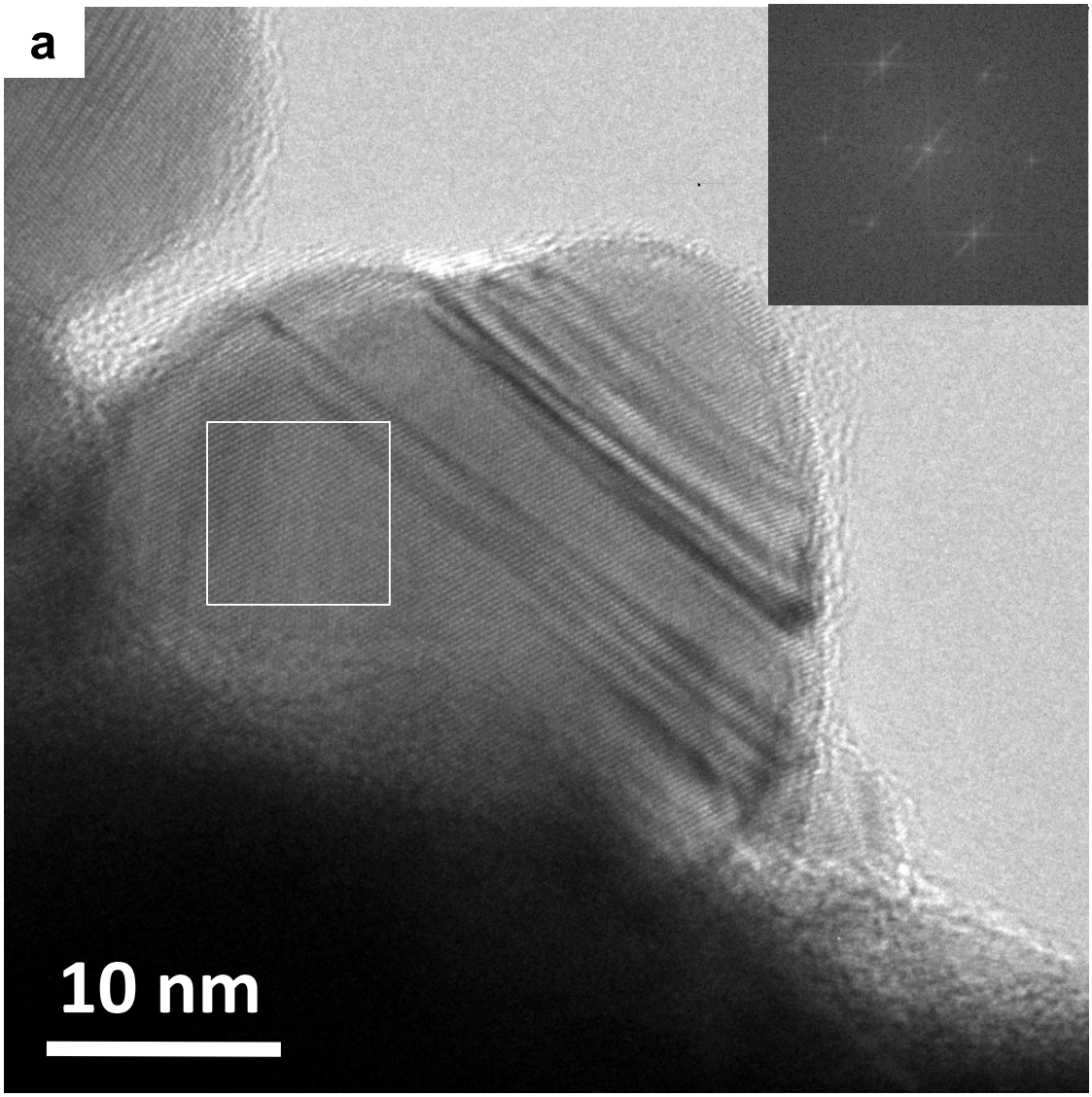

**Figure 5.5, continued**

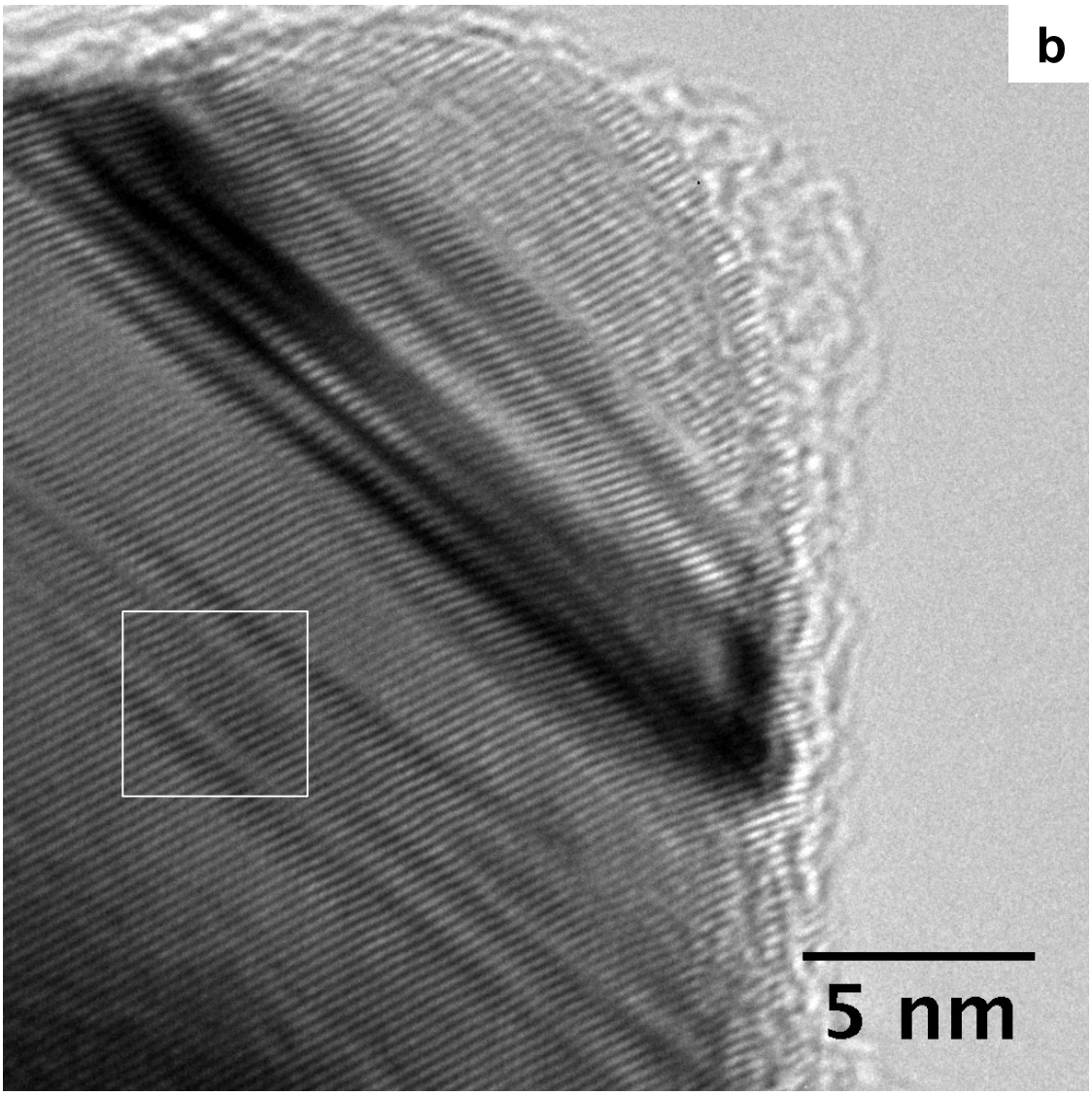


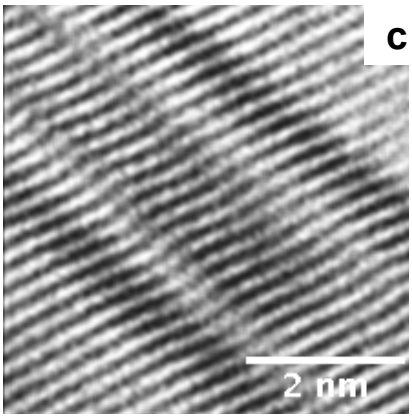


Interfringe spacing = 205 pm for {200}

**Figure 5.6: Schematic of impact event shown in Fig. 5.5 and then modelled using a MD simulation**

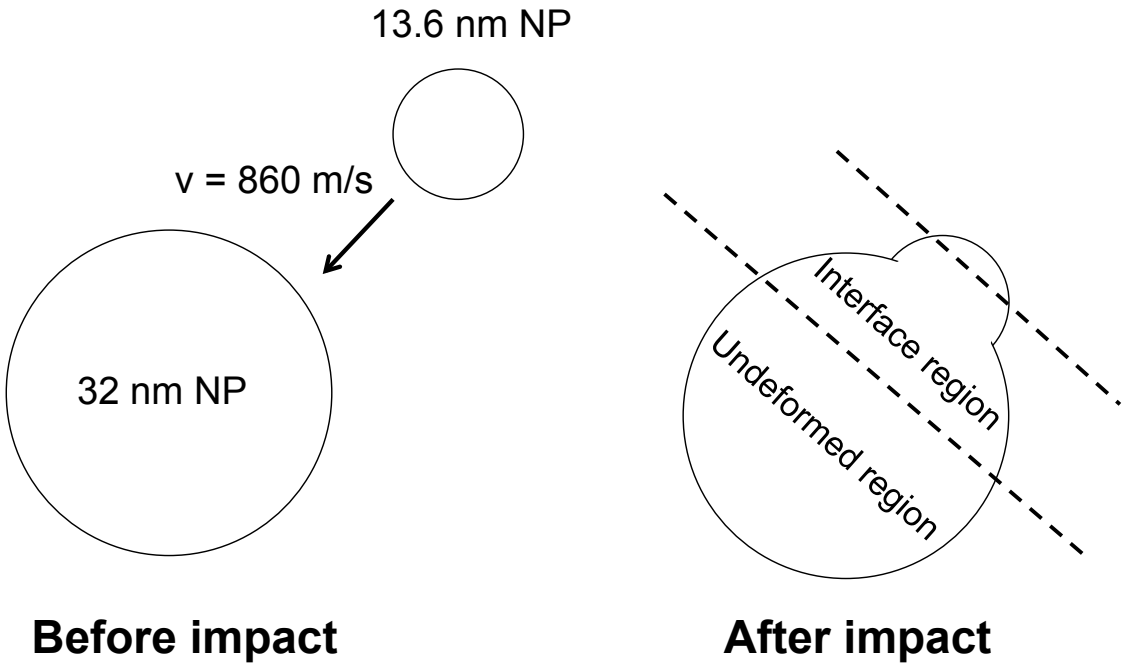


## 5.2 Computer simulation of NP on NP impaction microstructure (courtesy Tushar V. Chitrakar and Dr. Michael F. Becker)

The NP impaction observed using HRTEM (Fig. 5.5) and shown schematically in Fig. 5.6 (13.6 nm particle impacting on 32 nm particle at a calculated speed of 860 m/s) was modeled using MD simulation. MD simulations allow the positions for every atom in the simulation to be detailed at sub-picosecond resolution. Thus, the entire impaction event can be modeled and studied from the instant the small particle impacts the surface until the system formed by both particles completely thermalize and reach equilibrium. In contrast to the TEM observations, where only the final state can be observed, the computer simulation makes it possible to take snapshots of the impaction event as it is happening. Lastly, the final states from the simulations and experiments can be compared

and, if they are similar, give confidence that the mechanisms that led to the final state in the simulations have been accurately captured.

Figs. 5.7.a through 5.7.h are a series of snapshots from the MD simulations of the impaction event, showing the time sequence from the instant at which impaction occurs (t = 0 ps) until after equilibrium is reached (t = 560 ps). Based on these simulations, the impaction event can be decomposed as follows: Prior to the impact, a 13.6 nm particle is moving towards a 32 nm particle at a speed of 860 m/s. The 32 nm particle is set to be immobile by the boundary conditions in the computer simulation (Fig. 5.7.a). At the onset of the impact (Fig. 5.7.b), some of the atoms around the point of impaction point rearrange to form a region of what appears to be amorphous material that does not exhibit regular, long-range atomic periodicity (henceforth referred to as amorphous). Subsequently, the smaller particle keeps deforming and the amount of material in the amorphous state continuously increases. Six ps after the onset of impaction (Fig. 5.7.c), another mechanism is observed to accommodate the deformation of the smaller particle: Lattice planes at the top of the nanoparticle (that remained fully crystalline to this point) start to bend that and the particle starts to split in 3 different regions that remain crystalline or grains (labeled 1, 2, and 3 in the figure), and these grains move with respect to each other. The relative motion between those regions occurs both by translation and rotation. Fig. 5.7.d (t = 8 ps after impact) shows the continuation of this grain splitting. After t = 20 ps, the flow of matter and amorphization of material both cease (Fig. 5.7.e). In Fig. 5.7.e, some regions with a high concavity, indicated by an arrow, are also visible. This is a highly unstable configuration of atoms that subsequently disappears.

After the deformation of the 13.6 nm particle is complete, the amorphous material begins to crystallize. Fig. 5.7.f shows the end of this process. A large number of small grains are visible as the crystallization initiates from different regions in the particle. The coalescence of these grains is stopped when grains growing from different directions impinge on each other. At longer time scales, between t = 30 ps and t = 560 ps, other mechanisms occur more slowly that lead to grain growth (driven by the reduction in grain boundary area), and the disappearance of the highly concave area shown in Fig. 6.e (driven by the reduction in surface energy). The final state (t = 560 ps), after a stage of grain growth has occurred, is shown in Fig. 5.7.g. This final time step shows that the impaction event overall resulted in a reduction in grain size relative to that of the impacting particles. For example, the grain size of the 13 nm particle is reduced in size by one third when it is converted from a single grain before impaction to 3 grains after impaction. A high stacking fault density is also observed in the grains that resulted from the rapid crystallization process that followed amorphization. The MD simulations show that these twins within the grains and that formed close to the impact region are annealing twins rather than deformation twins because they grew from the crystallization from amorphous regions rather than from the nucleation and propagation of partial dislocations.

In contrast to the smaller NP, the larger 32 nm NP deforms to a much lesser degree. A small region in the vicinity of the impaction amorphizes and then crystallizes, but most of the material within the larger particle remains undeformed. In Fig. 5.7.h, twins are visible that were not present initially. This indicates that some of the kinetic energy of the impacting NP was accommodated by plastic deformation in the larger NP.

This plastic deformation occurred by twinning on {111} planes, leaving deformation twins in the final microstructure.

Comparing the experimental TEM observation following the impaction event (Fig. 5.5) to the final state of the computer simulation (Fig. 5.7.g and Fig. 5.7.h), there are significant similarities that suggest that the simulations are capturing much of the essential physics of the impaction: (1) the amount of deformation undergone by the smaller impacting NP is similar in both cases, as evidenced by the similarities in the final shapes (2) the larger NP deforms only to a small degree in both cases (3) There is a high density of twins present in both cases. There are also some significant differences between the simulation and the experiment. For example, in the simulation, the impaction event resulted in a reduction in grain size whereas in the TEM observation the particles were observed to coarsen into a single particle. Note, however, that TEM observations of other particles impacted under nominally identical conditions resulted a decrease in grain size (See, for example, Fig. 5.2), which suggests that there is a statistical distribution in behaviors for impacting particles under the same impaction conditions. Another difference between the simulation and the experiments is the orientation of twins that are observed. In the simulations the twins are present at an angle relative to the impaction plane whereas in the experiments the twins are oriented parallel to the impaction plane. These differences suggest that, in this regime of impaction conditions, the mechanisms for amorphization and crystallization are sensitive to small perturbations such as the relative orientation of the particles and these effects were not explicitly considered in these simulations.

**Figure 5.7: MD simulation of 13.6 nm Ag NP impacting on a 32 nm NP at a velocity of 860 m/s (velocity calculated to match impact condition during Ag deposition via LAMA)**
**(a) Before impaction**
**(b) t = 2 ps after impaction**
**(c) t = 6 ps**
**(d) t = 8 ps**
**(e) t = 20 ps**
**(f) t = 30 ps**
**(g) & (h) t = 560 ps**

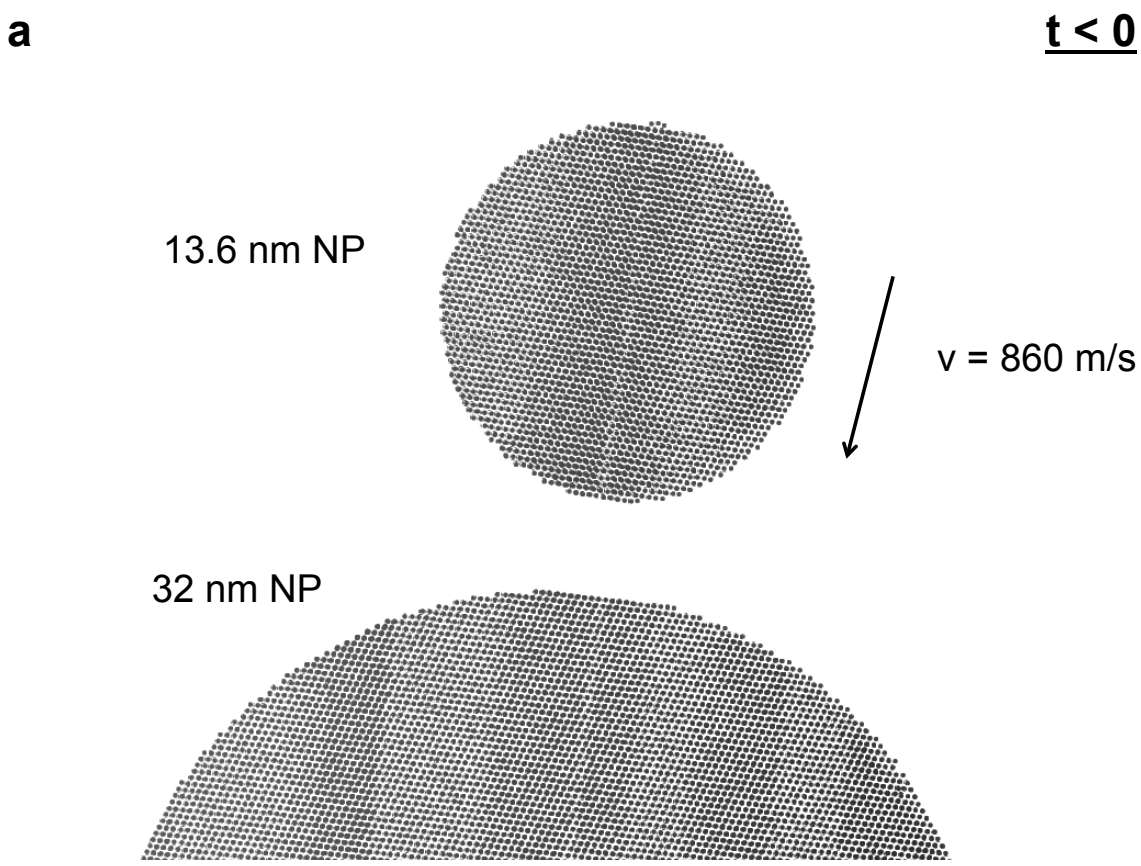

**Figure 5.7, continued**

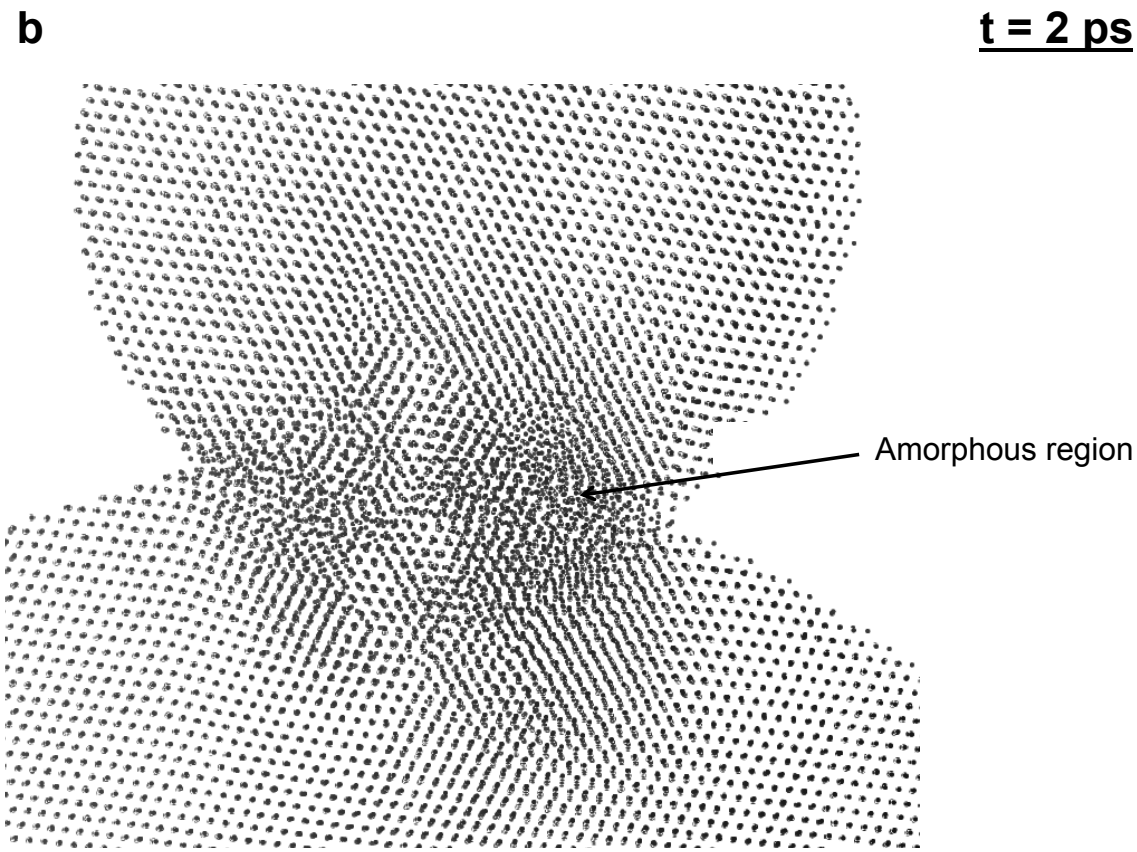

**Figure 5.7, continued**

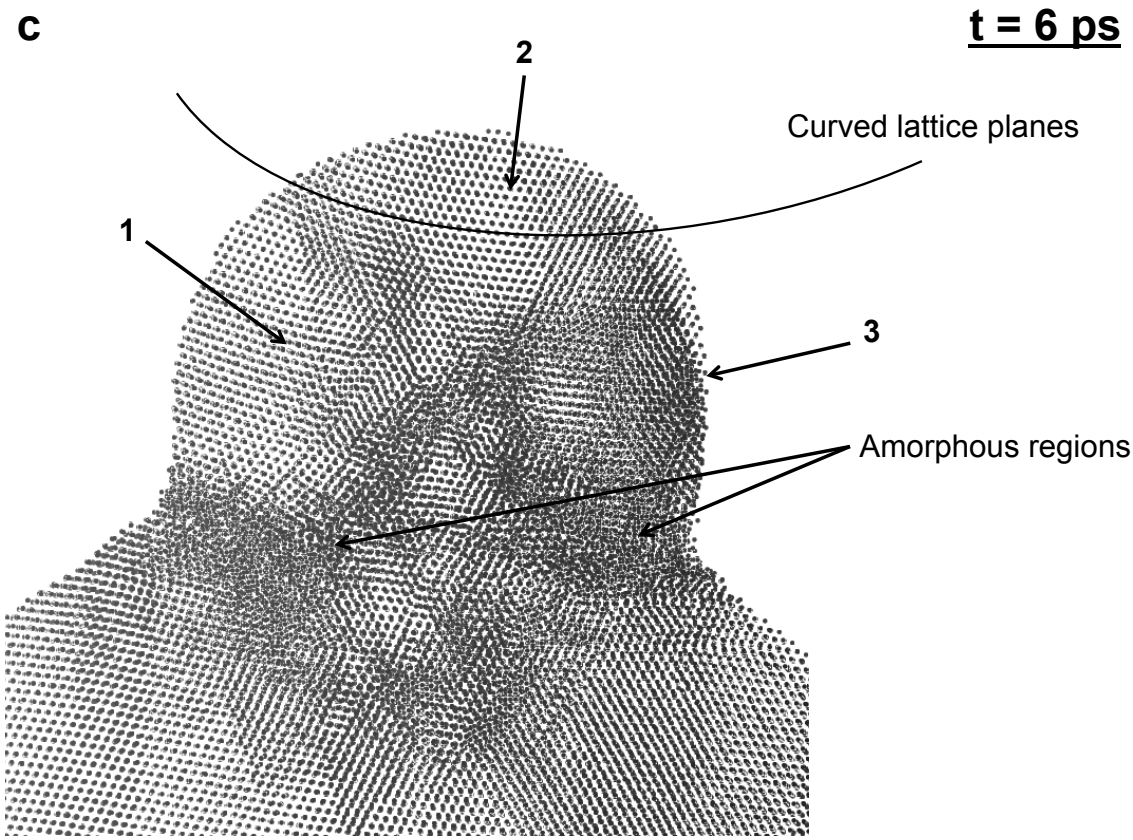

**Figure 5.7, continued**

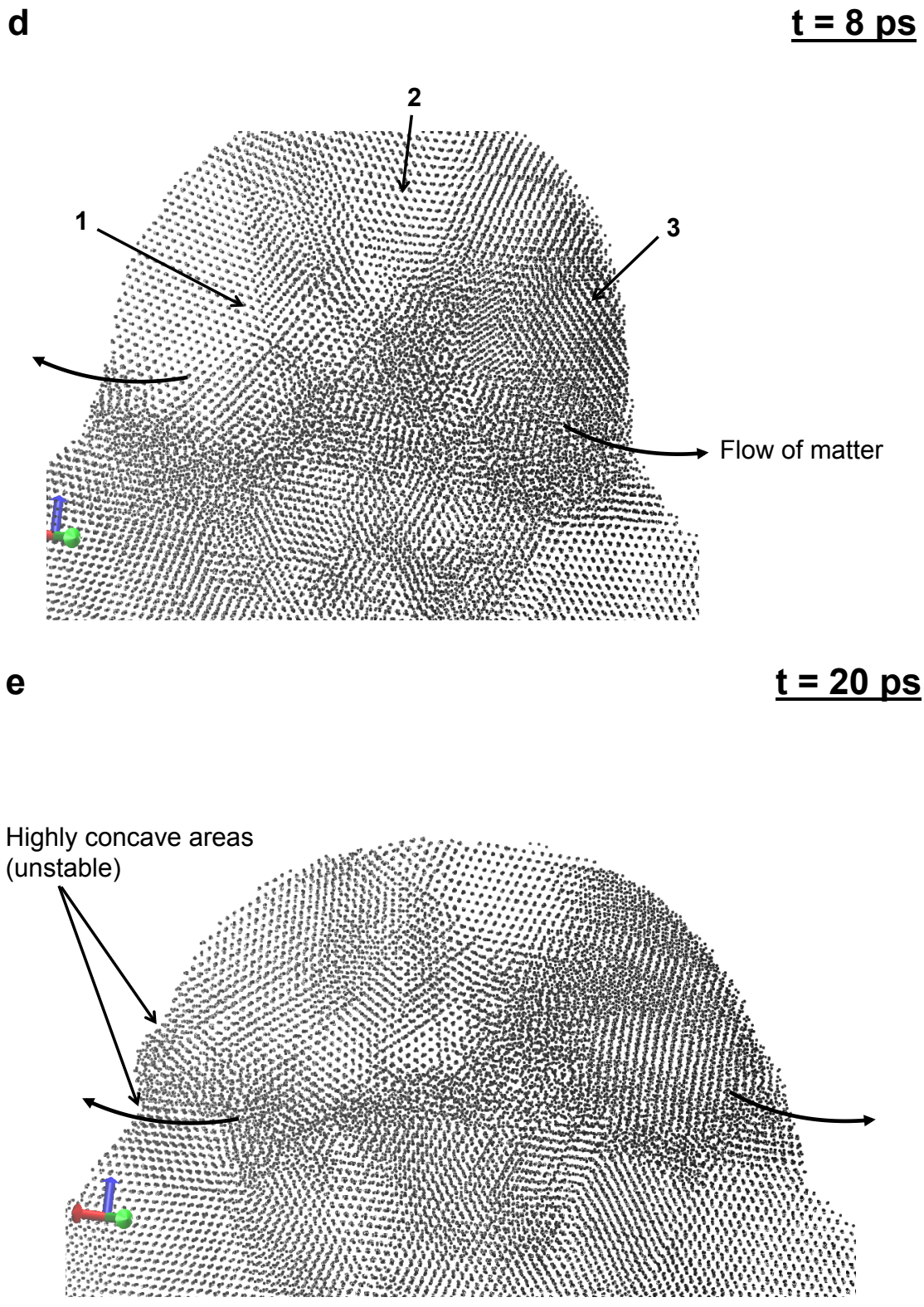

**Figure 5.7, continued**

**f** **t = 30 ps**

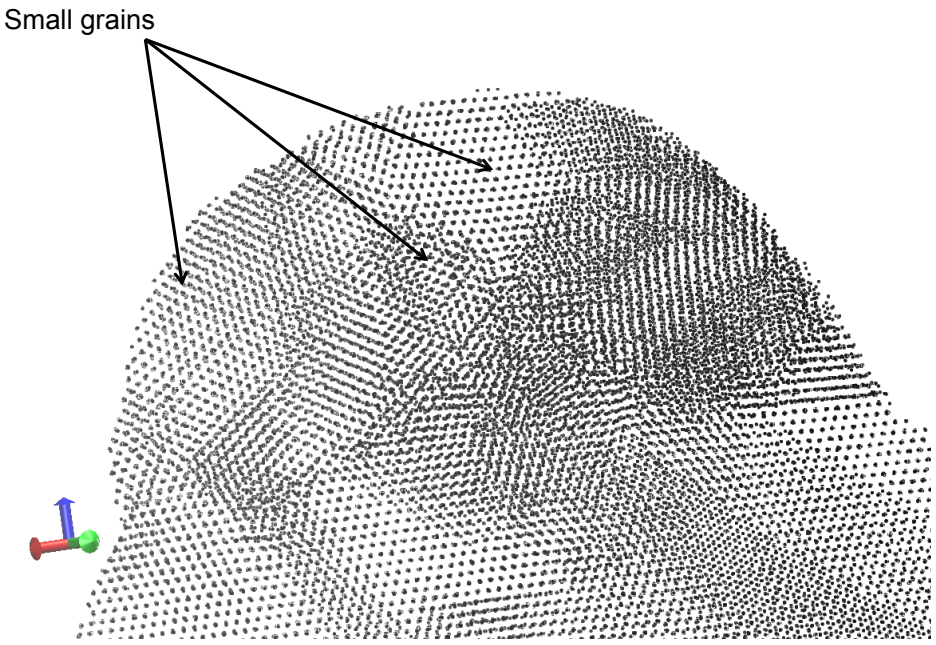


**g** **t = 560 ps**

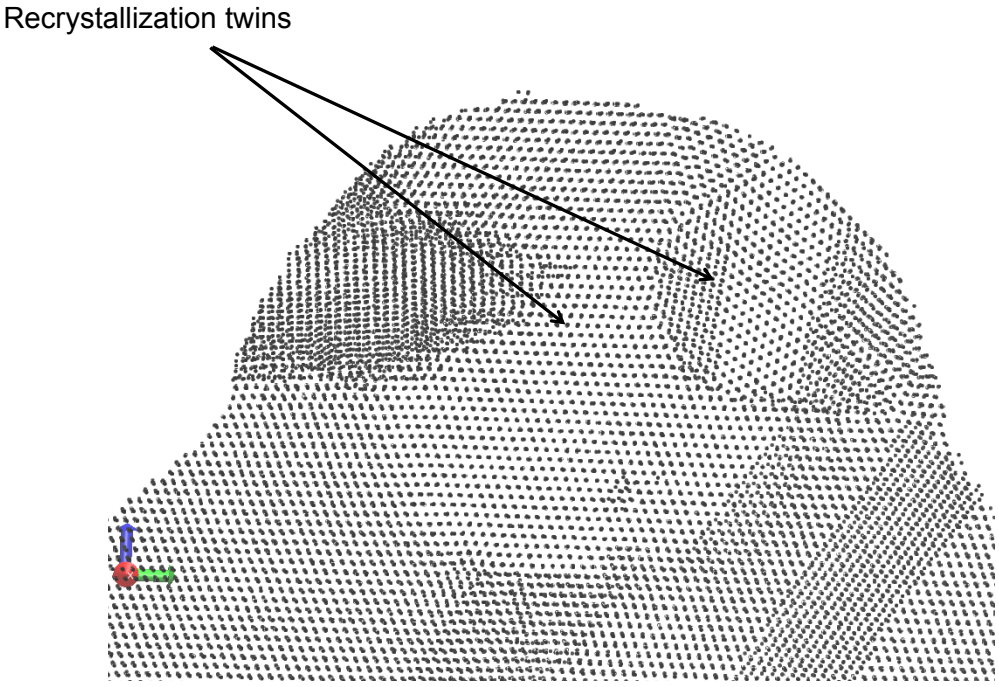

**Figure 5.7, continued**

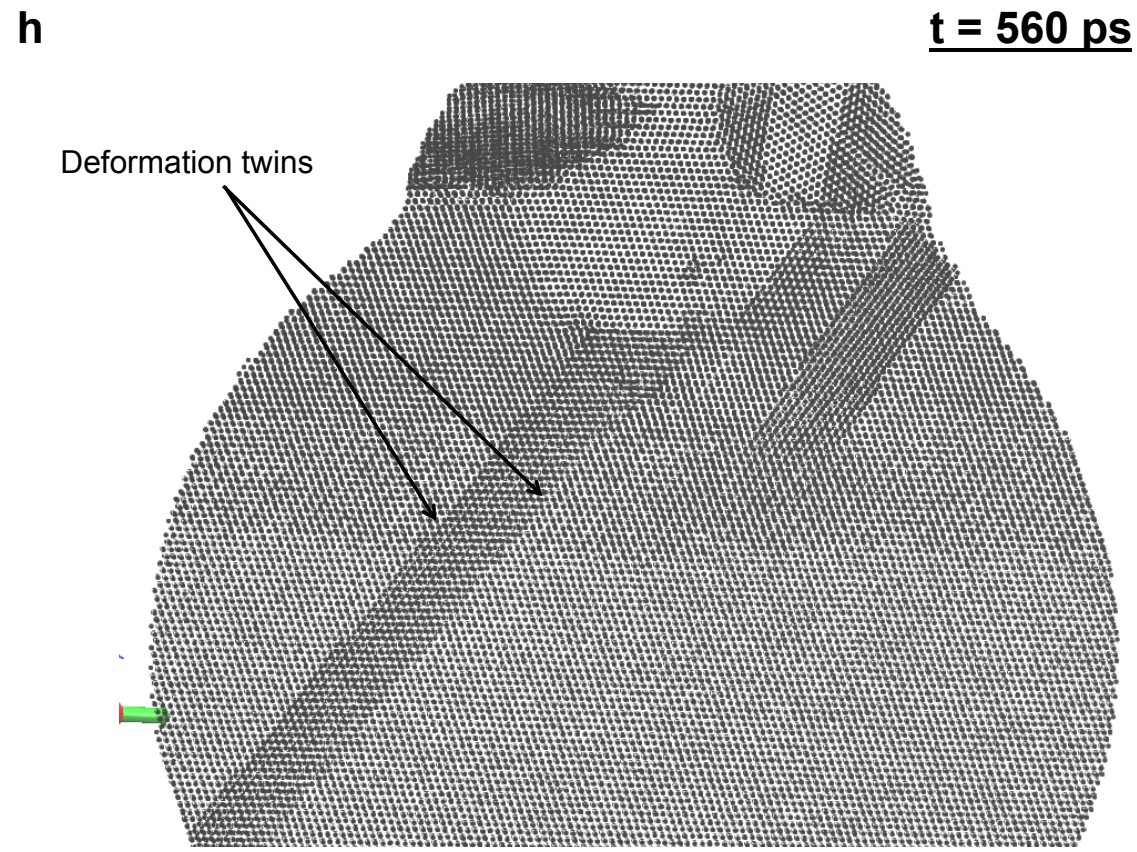


## 5.3 Conclusions on the mechanisms occurring during NP impaction

In the first part of this chapter, direct observations of the microstructures produced by impaction of NPs were presented. TEM micrographs for specimens prepared under nominally the same conditions showed both epitaxial depositions of NPs as well as non-epitaxial deposition are possible, suggesting that this range of processing variables lies near a transition from non-epitaxial to epitaxial. This study also showed that there are a variety of possible mechanisms occurring upon impact of NPs, and the TEM observations enabled identification of some of these. A key limitation of using TEM observations for the study of mechanisms of deformation and sticking during high velocity impaction is

that this technique is limited to the observation of only the final state after the impaction event has concluded.

Coupling MD simulations with the experimental results allowed a more in depth understanding of the mechanisms that occur during the impaction process. To illustrate this, a particular a NP-on-NP impaction event based on a TEM observation was studied in detail using a series of snapshots in time from the MD simulation. The simulation enabled us to decompose the impaction event into a sequence of events that include: 1) amorphization of the material in the vicinity of the impact in both nanoparticles, 2) matter flow by NP splitting and rotation as well as deformation twinning in the larger nanoparticle, 3) crystallization from the amorphous regions leading to either perfect crystals or, more often, crystals that contain annealing twins, and 4) grain coarsening by grain boundary motion. This sequence of events and the final state of the particles observed in the simulation is consistent with some of the final microstructures observed in TEM, but considerable variations were observed experimentally in the final states of particles produced under nominally identical conditions. It was suggested that, in this range of conditions, the final state is sensitive to details such as the relative misorientation of the impacting particles.

The variety of possible mechanisms illustrates the complexity of the NP impaction process, and explains the complex microstructure of the materials produced via the LAMA process. Establishing a quantitative model to predict the processing parameters to control the final microstructure would enable us to create advanced materials that fully exploit the advantages of the LAMA process. However it remains a challenge to this point. Based on the results from this chapter, it appears that increasing

NP speed and reducing NP size still remain viable strategies to achieve epitaxial deposition of films. The next chapter studies film build up from impaction of Ag NPs, where the speed of impacting NPs has been increased.

# Chapter 6: Improvements in film quality

In this chapter, modifications to the NP deposition process are explored and the effects on the deposited films are studied. The focus is on characterizing the influence of processing parameters on the macroscopic morphology of the films; a study of film microstructure will be presented in the next chapter. The first section presents briefly the motivations for trying to achieve better film quality. Next, the improvements to the NP deposition process that were implemented are discussed, with particular emphasis on the use of larger accelerating nozzles to increase the impaction velocity of the NPs. Lastly, the influence of nozzle size on the profiles of deposited Ag films and film densities are discussed.

## 6.1 Motivations and system improvements

O'brien [38] and Albert [23] were the first to study Ag deposited via LAMA for applications in electronics interconnects and packaging. Huang [39] and Nahar [22] later studied the sintering behavior and conductivity of such Ag films. At that time, they utilized a flat-plate nozzle with a diameter and accelerating length of 0.25 mm. With this nozzle size, the width of the expanding gas jet is narrow and so is the jet of impacting NPs. Most of the material is confined in a narrow region near the center of the jet, leading to narrow films. When the substrate is translated relative to the jet during deposition, "lines" are produced. These lines are suitable for applications like interconnects, but patterned lines with this morphology are not ideal because they do not produce films with uniform thicknesses over large areas. Also, the deposited material has a relatively high porosity (around 30%) and high porosities cause films with high

resistivity. MD simulations suggest that porosity could be reduced by increasing the kinetic energy of impacting NPs [5]. Therefore, there are motivations to both increase the NP kinetic energy to reduce porosity and also to adapt the system to produce more uniform films at higher deposition rates.

The modifications to the LAMA apparatus involved a number of changes to the deposition system. The capacity of the vacuum system was increased by changing the plumbing beneath the deposition chamber and the chamber itself was modified to accommodate flat-plate nozzles with a larger accelerating length and diameter, which results in higher NP impaction energies.

The methodology for determining the influence of nozzle size on impaction energy is explained in detail in Chapter 2. In summary, the gas velocity is first calculated under conditions of choked flow through the nozzle using thermodynamic relations for the gas temperature, pressure, and density. The particle velocity is then determined from the drag force on the particle from the expanding gas [3]. The calculated deposition energies are presented in Table 6.1 for Ag particles for NP diameters of 5, 10, 20, and 40 nm and for nozzle sizes of 0.25, 0.5, and 1 mm. From this table, it is apparent that the particle impaction energies increase as the particle size is reduced because smaller particles have less mass and therefore are easier to accelerate. It is also apparent that, for a given NP size, larger/longer nozzles result in higher impaction energies because the NPs spend more time in the nozzle, where the pressure and density are relatively high. This allows the momentum of the gas to be more effectively transferred to the NPs. Larger nozzle sizes are particularly effective at accelerating larger NPs.

**Table 6.1: Calculated NP kinetic energy (eV/atom) as a function of the NP diameter and accelerating nozzle size, using He carrier gas (calculations courtesy of Dr. Michael F. Becker)**

| NP diameter (nm) | NP kinetic energy (eV/atom) | | |
|---|---|---|---|
| | 0.25 mm nozzle | 0.5 mm nozzle | 1 mm nozzle |
| 5 | 0.63 | 0.8 | 1 |
| 10 | 0.47 | 0.62 | 0.8 |
| 20 | 0.34 | 0.47 | 0.62 |
| 40 | 0.22 | 0.33 | 0.47 |

Another improvement that was made to the LAMA apparatus was the development of a more flexible control system for the X-Y translating substrate holder that allows a wider range of patterns to be deposited. The improved stage control uses text files containing the instruction to write a given pattern using National Instrument's Labview software. An example is given in the appendix.

## 6.2 Influence of nozzle size on NP acceleration and film uniformity

Increases in the nozzle size do not result in self-similar deposition patterns. As the nozzle size in increased, the NP jet is spread out, as illustrated schematically in Fig. 6.1, leading to flatter, more uniform deposits. The density of NPs upstream of the accelerating nozzle is fixed by the ablation chamber and is therefore independent of the nozzle size. Thus, a larger nozzle leads to a wider NP jet with a lower NP density. The nozzle-to-substrate distance is fixed at three times the nozzle diameter, which is a distance large enough for the NPs to reach the maximum velocity but smaller than the distance at which a Mach disk forms as the carrier gas is expanded to supersonic speeds [14].

**Figure 6.1 : Schematic showing the influence of accelerating nozzle size on the aerodynamics of impacting NPs and on the resulting film profile**

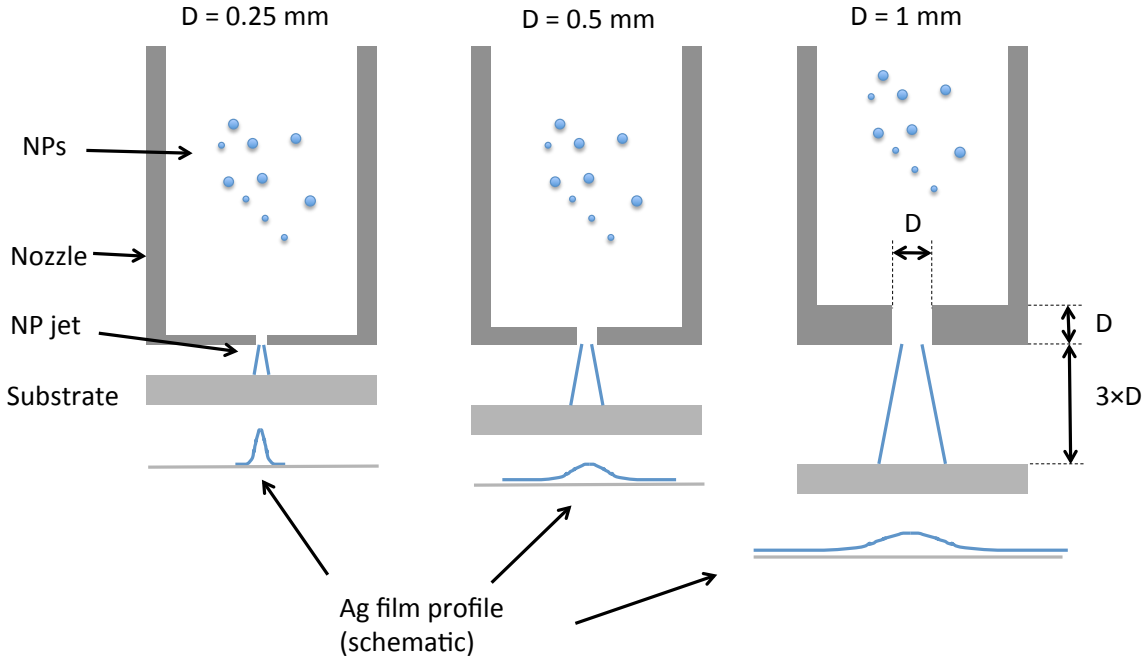


The profiles of Ag films or "lines" deposited for nozzle sizes of 0.25, 0.5, and 1 mm have been measured experimentally by optical profilometry, and are shown in Fig. 6.2. The optical profilometry scans for 0.5 and 1 mm samples are noisy because lower magnification lenses had to be used to capture the full width of the films. The line width and full width at half maximum (FWHM) of the films have been determined from the profilometry data and are shown in Table 6.2. This table confirms that using larger accelerating nozzles leads to wider films, with a more uniform distribution of the deposited material.

To deposit uniform films of 1 cm × 1 cm, the pitch between individual lines was chosen to be equal to the FWHM of an individual line. At a typical translating speed of 1 mm/s, it takes approximately 1 hour to deposit a film with the desired pattern using a 0.25

mm nozzle, and 3 min when using a 1 mm nozzle. This is a clear indication that the larger nozzle not only results in more uniform films, but also enables larger area depositions.

**Figure 6.2: Comparison of film profile for 3 nozzle sizes, obtained by optical profilometry**

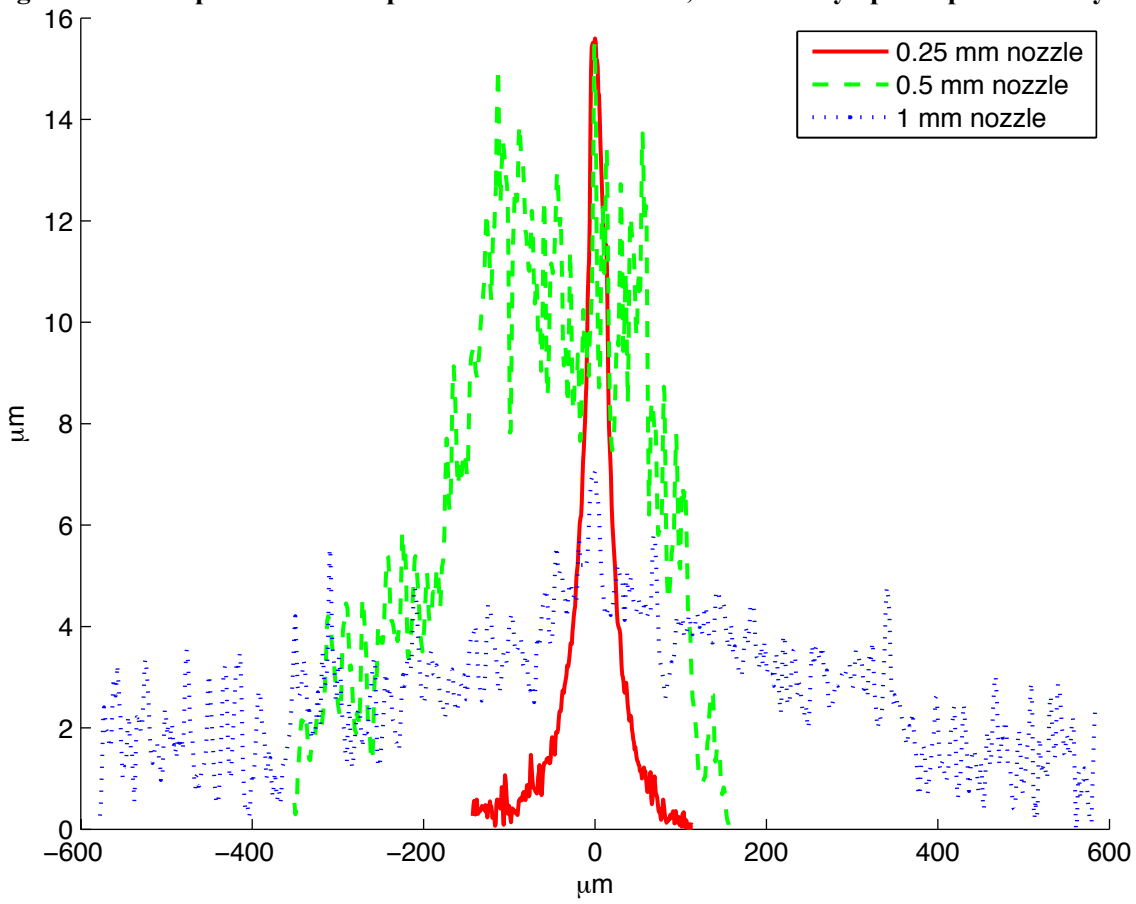


**Table 6.2: Typical width and full width at half maximum of films for 3 nozzle sizes, at a nozzle-to-substrate distance equal to 3 times the nozzle diameter**

| Nozzle diameter *(mm)* | Film width *(μm)* | FWHM *(μm)* |
|---|---|---|
| 0.25 | 256 | 28 |
| 0.5 | 507 | 186 |
| 1 | 1162 | 557 |

## 6.3 Influence of nozzle-to-substrate distance on the kinetic energy of NPs upon impaction

When the expanding gas (He in this work) recompresses onto the substrate, it creates a bow shock (region where the pressure is higher than the pressure in the vacuum chamber, but always lower than the pressure upstream of the accelerating nozzle). The bow shock slows down the NPs before they can impact onto the substrate, since NPs travelling in a gas at higher pressures experience a higher drag force [3]. The thickness of the bow shock can be estimated [48], and from that, a nominal 10% reduction in velocity for all 3 nozzles can be expected for NPs in the size range of 5-10 nm. For bigger particles, the deceleration is less severe since they have more momentum. When increasing the nozzle diameter and keeping the nozzle-to-substrate (z/d) equal to 3, the deceleration is more severe, since decreasing the nozzle-to-substrate distance increases the pressure in the bow shock [48]. The effect is greater for larger nozzles and smaller particles; for example, 5 nm NPs accelerated with a 1 mm nozzle are predicted to be slowed by 33.6% [46].

Previously, it was established that there is a critical velocity at which particles stick, and previous measurements [44] of Ag line width vs. z/d for z/d between 2 and 12, showed a linear increase in line width with z/d (measurement made for d = 0.25 mm). This shows that adhesion efficiency and the particle impact velocity of NPs is not strongly affected by the bow shock deceleration effect at least for d = 0.25 mm, even for z/d equal to 3. Also, the data presented in Table 6.2 shows that Ag line width seems to increases linearly with nozzle diameter, for z/d equal to 3. Again, this

suggests that adhesion efficiency of NPs is not dramatically affected by the deceleration effect.

However, for future work, a larger distance should be used for larger diameter nozzles. Ideally, the nozzle-to-substrate distance and diameter should be scaled together [45]. This would minimize the bow shock deceleration effect especially for larger nozzles and small NPs.

## 6.4 Film densities

Although samples written with the 0.25 mm nozzle exhibit a continuous, cohesive microstructure, it was clear from handling the samples during the preparation of electron transparent TEM sample, that these films had a lower adhesive strength to the substrate compared to those deposited with the larger nozzle (all but one membrane collapsed during the final thinning stages of thinning). This is also consistent with a previously measured porosity of 30%, for films produced under similar conditions [22]. It was easier to manufacture TEM samples from films deposited with 0.5 and 1 mm nozzles, corresponding to higher impaction energies for the NPs. Film density in LAMA is known to increases with impaction energy [28]. For example, Ag films deposited from 50 nm particles with a speed of 364 m/s resulted in films with a relative density of approximately 40% whereas films deposited from 5-10 nm particles with a speed of 920-1056 m/s resulted in films with a relative density of 70%.

Direct measurement of film densities were not conducted on samples deposited with 0.5 mm and 1 mm nozzles. The method used previously to measure the densities of Ag deposits [22] relies on a precise measurement of film profile to assess the volume of

the deposit. Subsequently, the sample is dissolved in an acid and the concentration of Ag in the solution is measured using the inductively coupled plasma (ICP) method. The porosity can be deduced from the knowledge of the volume and the mass of the deposit. However, for samples deposited with 0.5 mm and 1 mm nozzles, the width of the Ag lines is too large to use the high magnification lens on the available optical profilometer. Volume measurement using lower power lenses leads to large errors. As can be seen on Fig. 6.2, the large peaks on the profile of samples deposited with 0.5 mm and 1 mm nozzle prevent a precise volume measurement. These peaks correspond to artifacts in the optical system when using low power lenses, rather than actual roughness.

Nevertheless, the higher mechanical stability of samples deposited with 0.5 mm and 1 mm nozzle was clear during preparation of TEM specimens using a focused ion beam. In addition, the films deposited with the larger nozzles had a shiny, mirror-like finish compared to a dull looking surface of samples deposited with smaller nozzles, as can be seen on Fig. 6.3. The likely cause of this improvement in optical quality is an increase in the film density, which reduces scattering from the surface. The TEM micrographs presented in the next chapter show the Ag films microstructure and are also consistent with a more dense material, although it is difficult to quantify density using TEM.

**Figure 6.3 : Optical micrographs of Ag films deposited with a) 0.25 mm nozzle b) 1 mm nozzle**

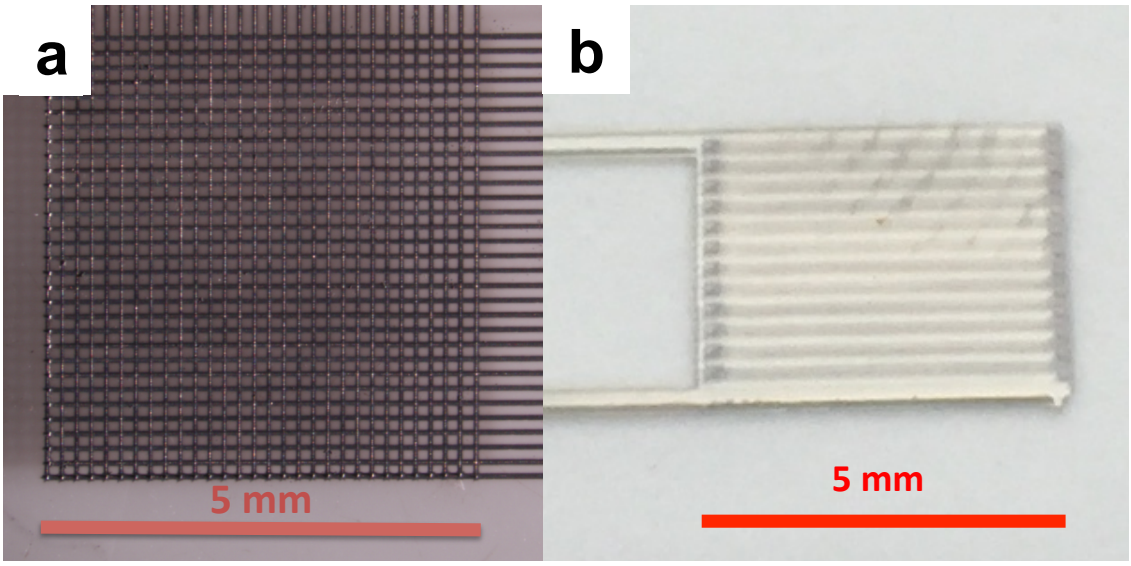


## 6.5 Conclusions on the quality of Ag films

In this chapter, we have shown that improvements made to the system by modifying the X-Y stage control and through the use of larger deposition nozzle sizes improve the film quality from both a microscopic and a macroscopic point of view. Specifically, larger area deposits with more uniform thicknesses, significantly higher optical quality, and higher densities were demonstrated.

# Chapter 7: Study of film microstructure by electron microscopy (SEM, TEM, EDS)

In this chapter, we study the microstructures of Ag films deposited by the impaction of nanoparticles (NPs). The influence of increasing kinetic energy of impacting NPs on the microstructure is investigated. Higher kinetic energies of impacting NPs are obtained with larger nozzles, as discussed previously. The microstructures have been observed directly using SEM and TEM micrographs of cross-sectional samples. More details on film deposition and on the fabrication of TEM cross-sectional samples are given in Chapters 3 and 4, respectively.

This chapter is organized as follows: The first section presents electron microscopy (EM) observations of Ag samples deposited using 0.25, 0.5 and 1 mm accelerating nozzles. Cross-sectional TEM samples were fabricated and observed with increasing magnifications. Images at the lowest magnifications show the full thickness of the films (2-20 μm), images at the highest magnification reveal grain sizes of less than 5 nm. Fig. 7.1, 7.2 and 7.3 show a set of micrographs for each of the three samples. The second section provides a composition analysis using EDS. It confirms the presence of elements expected in different regions of the TEM samples, and also shows the high quality of TEM samples, since there is no observable Ga contamination from TEM sample preparation using the focused ion beam (FIB) tool. The third section discusses various aspects of film microstructure based on EM observations: The influence of increasing NP impaction energy on the film density, challenges associated with direct grain size measurements, and the influence of NP kinetic energy on grain morphology and grain

size. Section 3 also discusses two different film growth mechanisms. Finally, the benefits of using these EM observations coupled with molecular dynamics (MD) simulations to improve the understanding of multiple NP impaction events is discussed.

## 7.1 Electron microscopy observations

This section presents SEM and TEM investigations of LAMA-deposited Ag films, with increasing impaction energy. All three samples presented in this section were deposited by overwriting the same region on the stainless steel substrate with 20 passes of the NP jet. The cross-sectional TEM samples were obtained using a FIB technique that is detailed in Chapter 4.

### 7.1.1 Sample 1: Lowest impaction energy

SEM images of sample 1 (Fig. 7.1.a) that was written with the 0.25 mm nozzle show a patterned line with an approximately Gaussian profile with a peak film thickness of 15 μm at the center of the line. The full width at half maximum of this line is approximately 10 μm. A higher magnification image of a cross-section of this film (Fig. 7.1.b) shows that there is a distinct "fan-like" morphology with columnar structures present that originate from the center of the base of the line. Similar morphologies have been observed previously [23]. The spatial scale of this morphology is sub-micron, and clearly much larger than the size of the impacting particles. Possible mechanisms for the formation of this morphology are discussed in Section 7.3.4.1.

An electron-transparent window was fabricated from a thinner region, away from the center of the line because the large gradient in film thickness close to the center of the line prevented the fabrication of an electron-transparent window at this location. Low

magnification TEM micrographs (Fig. 7.1.c and 7.1.d) show the full thickness of the Ag film at this location. They reveal a porous microstructure that results from a mixture of individual NPs and unablated MPs from the LAMA process. A selected area electron diffraction (SAED) pattern obtained from this region is shown in Fig. 7.1.e (a circular region with diameter of 640 nm). The SAED confirms that this region is polycrystalline and consists of a large number of grains, such that nearly complete rings are visible in the SAED. This also confirms that epitaxial deposition did not occur over an area this large for these processing conditions.

Fig. 7.1.f shows a HRTEM picture of the thinnest observable region within the electron transparent window. The lattice fringes visible in the particles reveal that there are multiple grains present within some of the particles. The observed particle size is consistent with the size of impacting NPs. It has been previously reported that damage may occur during TEM specimen fabrication using a FIB that includes amorphization of the sample material [31]. In addition, the region shown in Fig. 7.1.e lies within a large pore, and was therefore likely protected from direct interaction with the Ga ion beam during the FIB process, which would have minimized sample damage. Thus, it is likely that the HRTEM micrograph shown in Fig. 7.1.f is representative of the film microstructure, rather than artifacts created during TEM sample preparation.

**Figure 7.1 : Microstructure of Ag film deposited with a 0.25 mm nozzle in 20 passes of the NP jet over the substrate**
**(a) SEM micrograph showing Ag film cross-section (54° tilted view)**
**A TEM cross-sectional sample was fabricated in the region shown in the smaller box**
**(b) Higher magnification view of region highligted in (a)**
**(c) Low magnification TEM micrograph showing the full thickness (3 µm) of a film deposited using a 0.25 mm nozzle. The electron transparent window shown here was fabricated about 15 µm away from the center of the line because the large gradient in thickness closer to the center was not suitable for the FIB process**
**(d) Low magnification TEM micrograph showing a porous microstructure and particles that are mixture of individual NPs and unablated MPs from the LAMA process.**
**(e) SAED pattern corresponding to region shown in Fig. 7.1.d. The column to the right indicates the family of planes associated with each ring in the DP, starting from the innermost ring; the pattern is consistent with polycrystalline grains of fcc Ag**
**(f) HRTEM image obtained from a thin region in the electron-transparent window. The lattice fringes visible in the particle show evidence of multiple grains within the particles. The particle size is consistent with the size of impacting NPs**

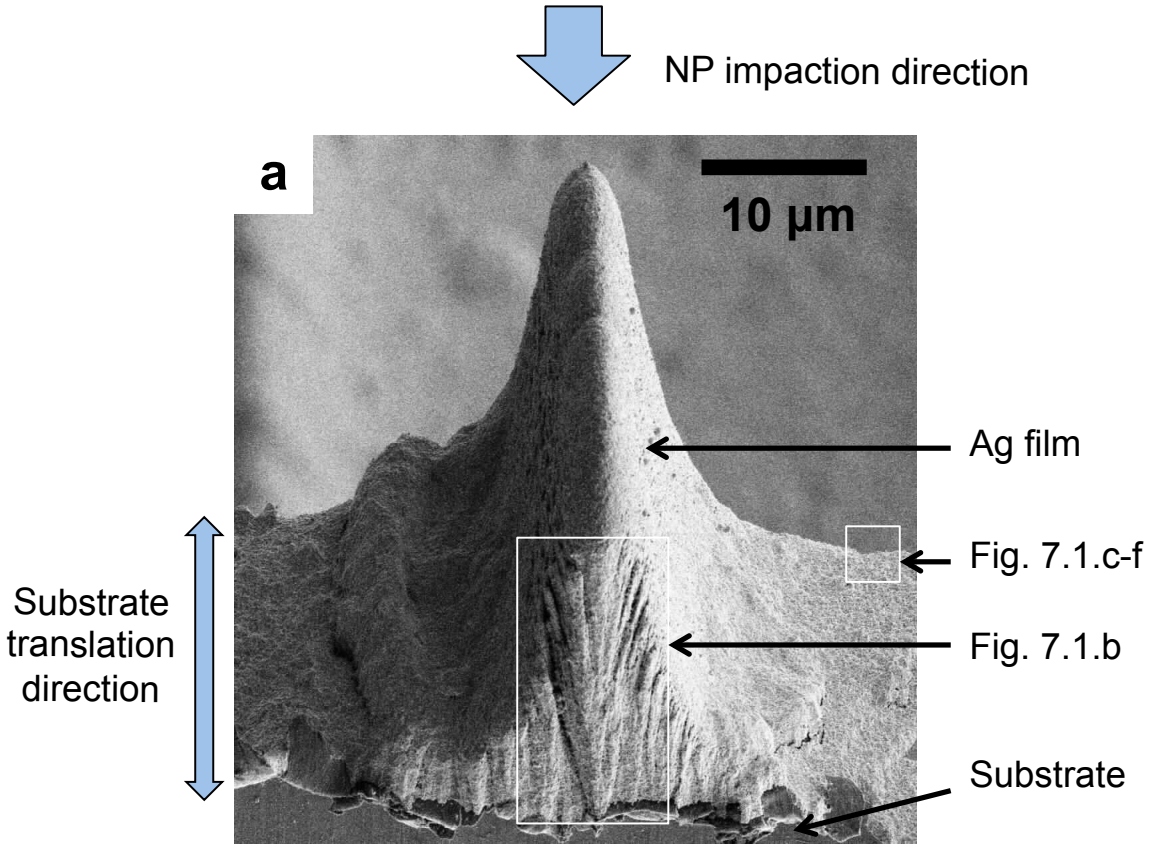

**Figure 7.1, continued**

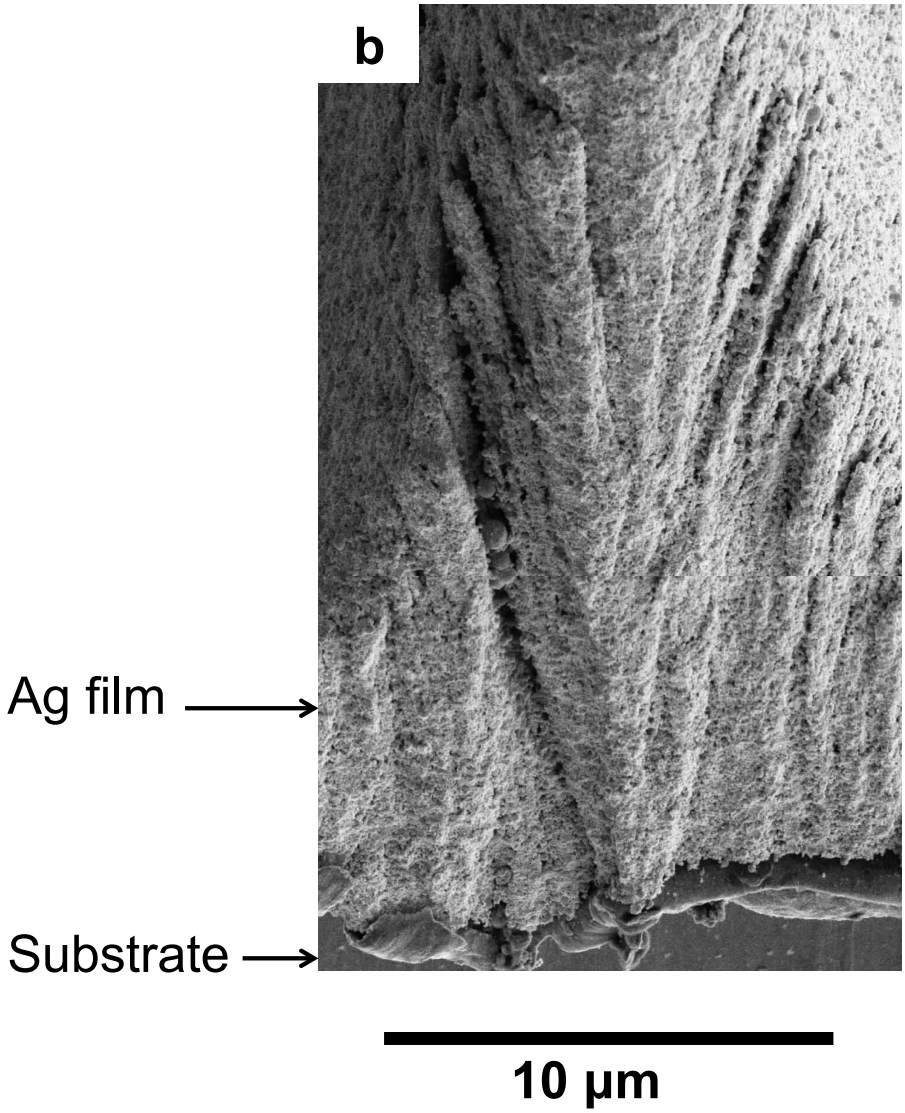

**Figure 7.1, continued**

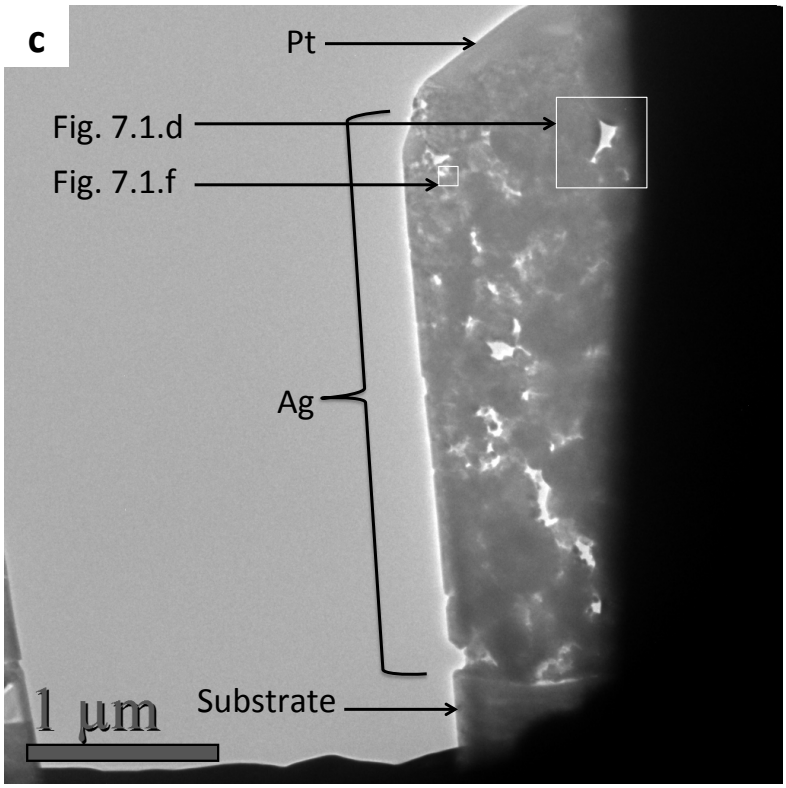


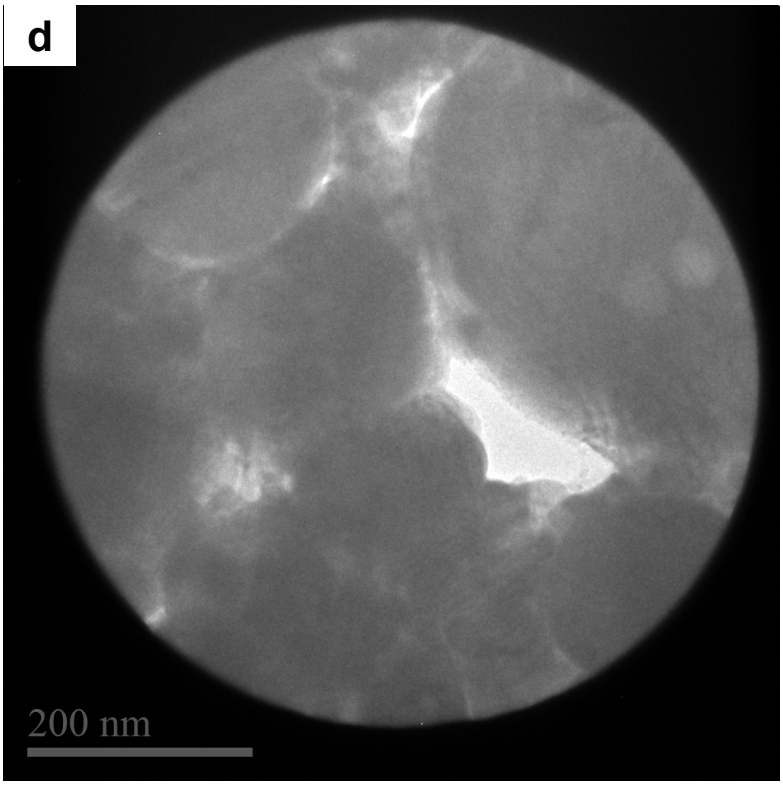

**Figure 7.1, continued**

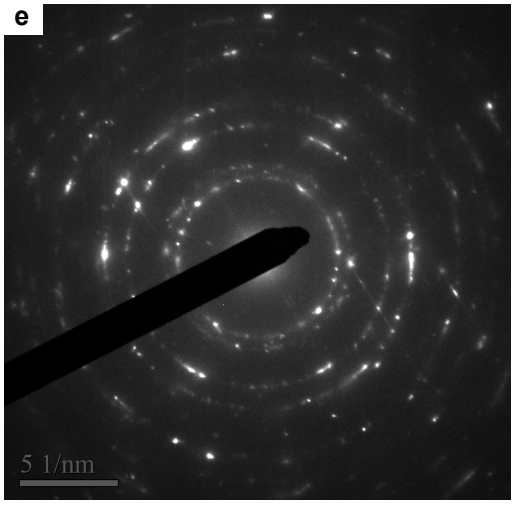


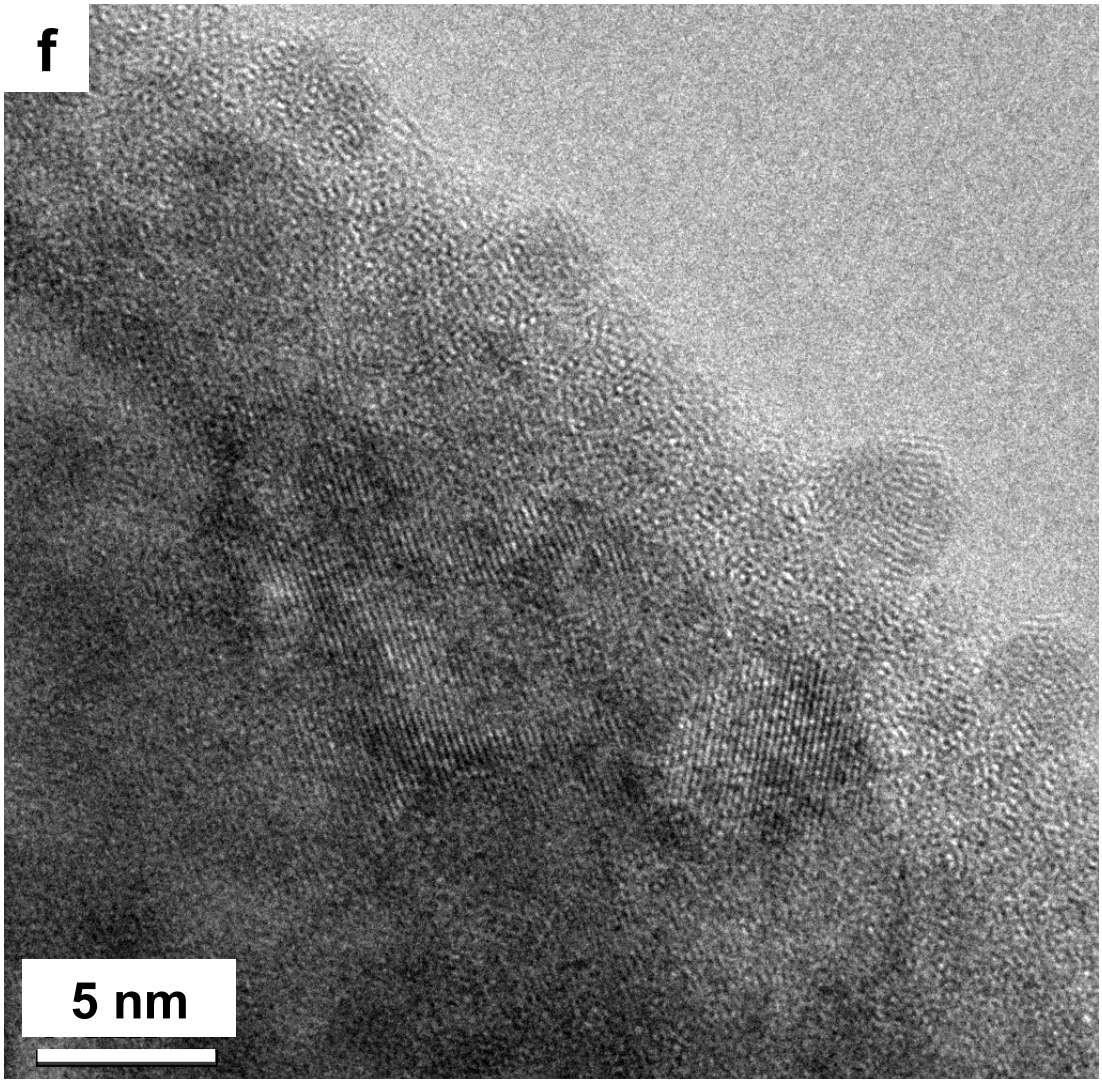

### 7.1.2 Sample 2: Intermediate impaction energy

A low magnification TEM image (7.2.a) shows the electron-transparent window produced to investigate film microstructure. In this case, the Pt protective layer has been visibly etched from the top of the window and therefore some of the film has also been removed. Note the absence of residual MPs in the microstructure, unlike in sample 1. The thickness of the observable region is approximately 1.5 μm. At least 16 distinct layers of Ag NPs can be distinguished in this micrograph. This compares to the 20 layers deposited for this sample, which confirms that part of the films was also removed during the specimen preparation. The cross-sectional TEM image also shows for the first time the formation of layers during successive passes of the NP jet over the substrate. Potential mechanisms that may have lead to the formation of such distinct layering will be discussed in subsequent sections of this chapter.

The region of the sample shown in Fig. 7.2.a was too thick to obtain HRTEM pictures of the grains. Thus, the following alternative method was used to reveal grain morphology and size: A SAED pattern was obtained from a large area covering the whole thickness of the sample. A bright spot in the diffraction pattern was then used for dark field imaging. This technique highlights only grains of that specific orientation, with these grains appearing as bright regions in the dark field image. This mode of imaging also revealed features not visible in Fig. 7.2.a. In particular, the dark field imaging shows that equiaxed grains are present with a size ranging from 5 nm to 40 nm (See Figs. 7.2.b and 7.2.c). This grain size is similar but slightly larger than the size of the impacting NPs; this suggests that some degree of epitaxy occurred over an area of the size of a few grain diameters, particularly amongst smaller particles in the distribution.

On the other hand, Fig. 7.2.d and 7.2.e present evidence that epitaxial deposition of small NPs might have occurred over a large area compared to the particle size. The SAED pattern was obtained from a region with a diameter close to 100 nm, which is significantly larger than the mean size of impacting NPs. The diffraction pattern clearly shows a preferred crystallographic orientation within this area, consistent with epitaxial deposition of a large number of smaller NPs.

Fig. 7.2.f is a bright field TEM micrograph where twins are clearly recognizable. For example, the box in Fig. 7.2.f highlights a 40 nm equiaxed grain containing a twinned region. The presence of large equiaxed grains is consistent with non-epitaxial deposition of the larger NPs present in the NP aerosol size distribution. The twins within these grains could have been present prior to impaction, resulting from the laser ablation process, but could also have been formed by plastic deformation upon impact of the NPs (deformation twins).

**Figure 7.2 : Microstructure of Ag film deposited with a 0.5 mm nozzle, in 20 successive passes of the NP jet over the stainless steel substrate.**
**(a) Low magnification TEM image**
**(b) Dark field image. Bright regions show grains of a specific orientation**
**(c) Higher magnification of region highlighted in (b). This observation technique clearly reveals the presence of equiaxed grains of up to 40 nm in diameter.**
**(d) Low magnification TEM micrograph showing a region close to the interface between substrate and film**
**(e) SAED pattern of region highlighted in (d), showing a preferred crytallographic orientation within this region, consistent with epitaxial deposition of NPs over an area that is large compared to the impacting NP size**
**(f) Bright field TEM image showing equiaxed grains <40 nm in diameter, with twin defects clearly visible, for example in the highlighted region**

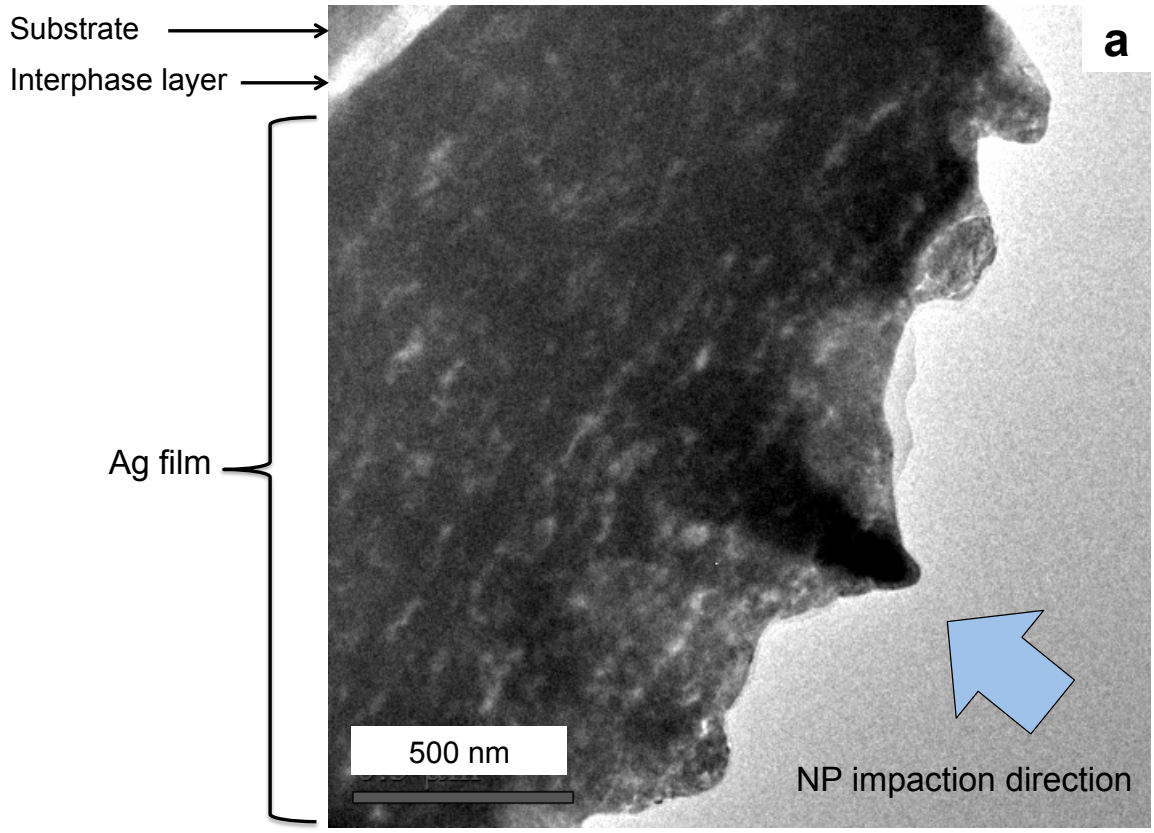

**Figure 7.2, continued**

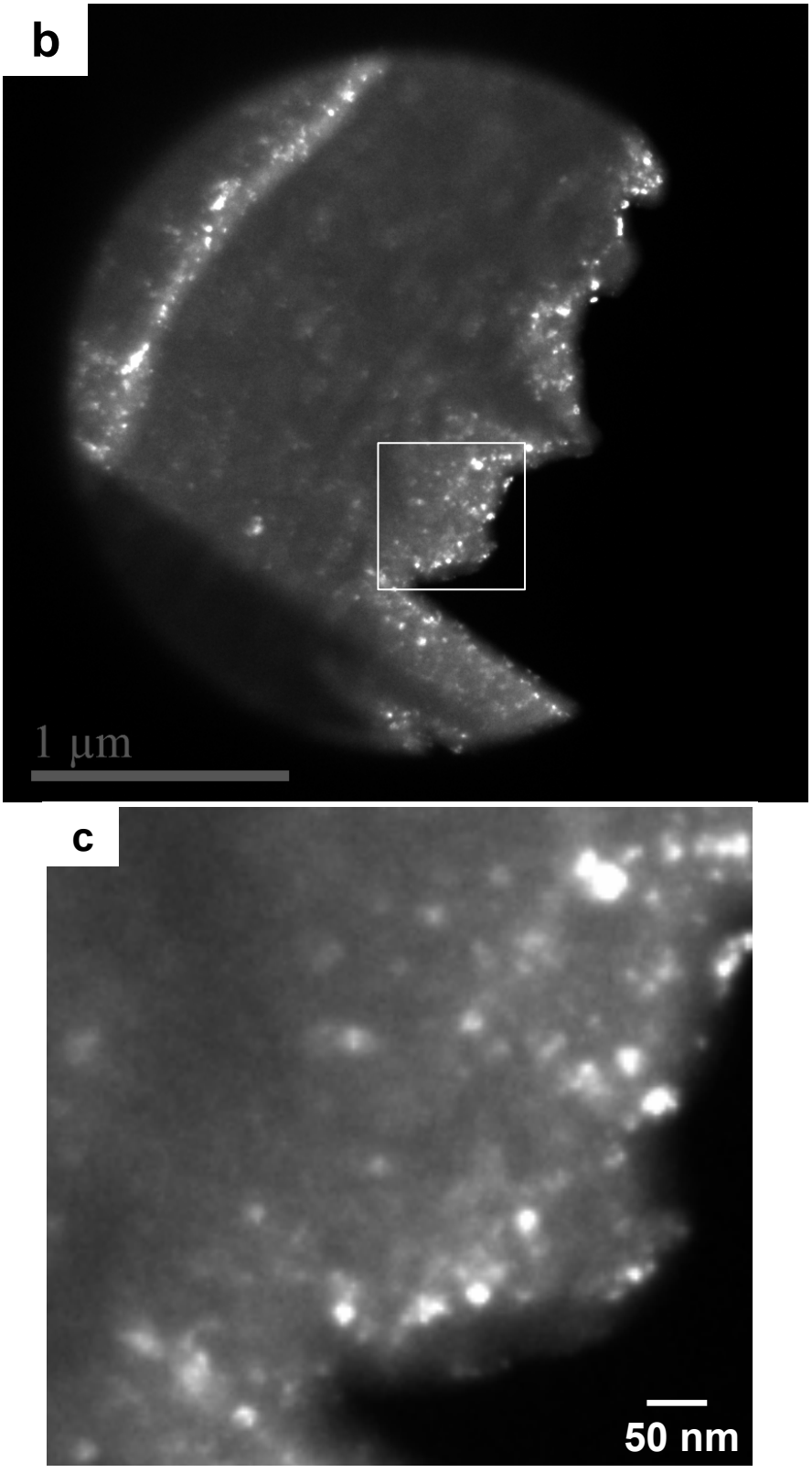

**Figure 7.2, continued**

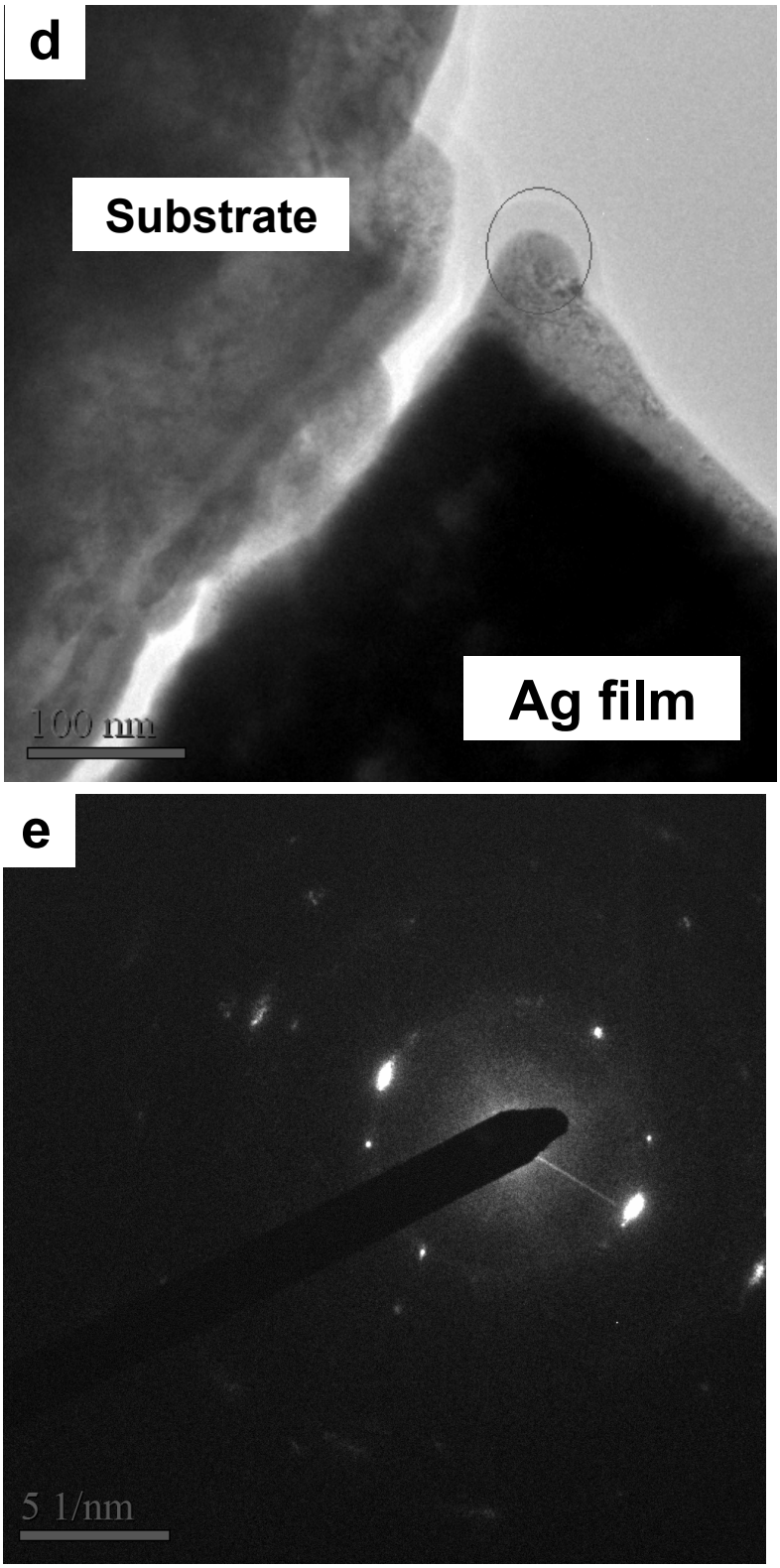

**Figure 7.2, continued**

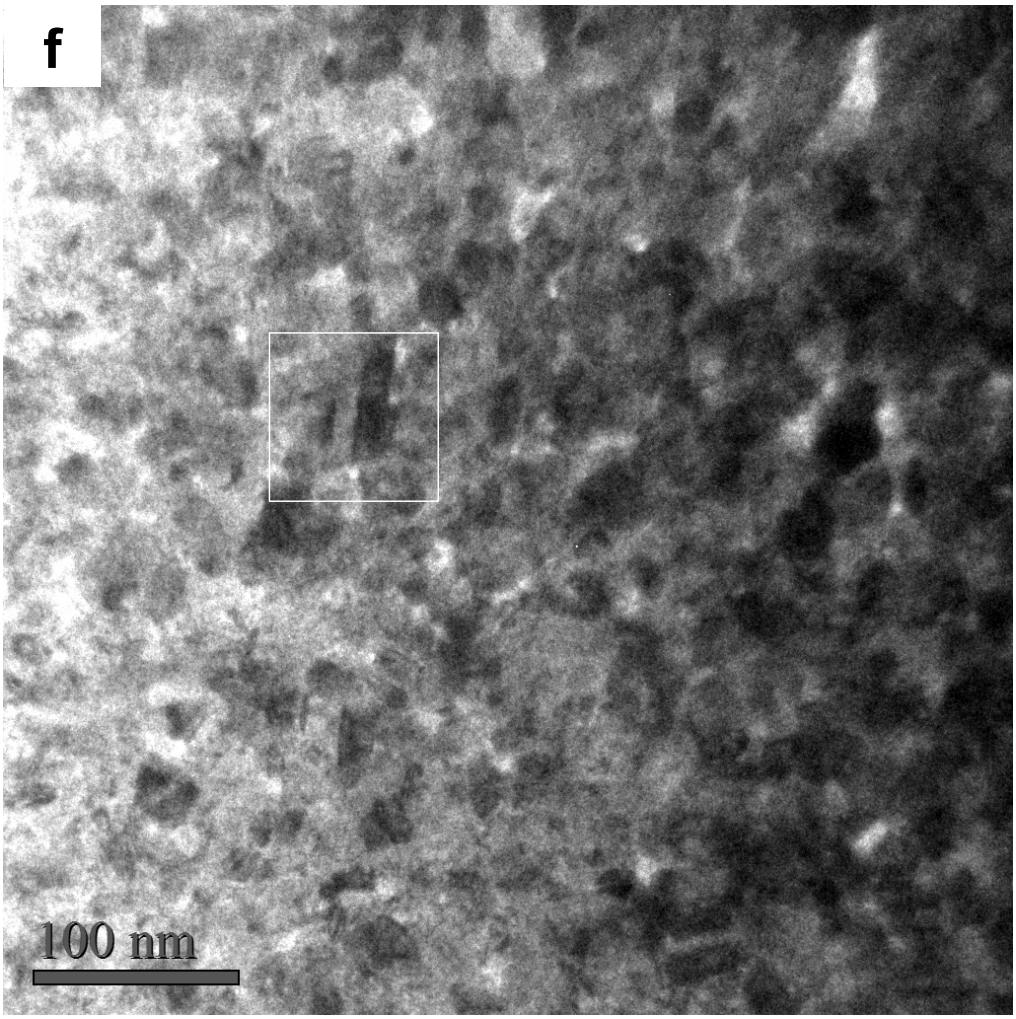


### 7.1.3 Sample 3: Highest impaction energy

The highest quality electron-transparent window was obtained from an Ag film deposited using a 1 mm nozzle, which resulted in the highest impaction energy of the three nozzles that were studied. Following the methodology used for samples 1 and 2, images were obtained with increasing magnification starting at the lowest magnification. A SEM image taken at a tilt angle of 54° shows the location of the electron transparent

window, which has a thickness of less than 100 nm. The differences in contrast show that the window contains both part of the Ag film, and part of the stainless steel substrate.

A low magnification TEM image (Fig. 7.3.b) shows the full thickness of the Ag film. Unlike sample 2, the protective Pt layer is still present and thus the full thickness of the film is observable. We can distinguish 20 layers of Ag NPs, corresponding to the 20 successive passes of the NP jet over the substrate. Unlike in sample 1, but similarly to sample 2, no unablated MPs are observable in the microstructure. The regions that are presented at higher magnification in subsequent figures are shown with white boxes.

Fig. 7.3.c shows a bright field TEM image where the stainless steel substrate, an interphase layer and the first 3 layers of NPs are all visible. Individual NPs can be seen both in the interphase region and within the layers of the films. EDS data presented later in Section 2 revealed that the interphase layer contains mostly carbon. A higher magnification view of the interphase layer using HRTEM (Fig. 7.3.d) reveals individual NPs are embedded in the interphase layer. This indicates that during film formation in the deposition chamber, the very first layer of NPs didn't impact directly onto the substrate, but onto a layer of organic material. The organic layer was present despite careful cleaning of the substrates prior to film deposition using acetone followed by ethanol/methanol. Most importantly, the NPs embedded in the carbon, which are isolated so that they cannot coarsen once they deposit, are as small as 2 nm. Particles this small were not visible in the films in the absence of the carbon, which suggests that very fine Ag particles coarsen upon impaction in the absence of the carbon interphase.

Bright field images of thin regions within the electron transparent window (Fig 7.3.e) reveal a dense, polycrystalline microstructure. Equiaxed grains containing twins are

present, with the largest having a size similar to those observed in sample 2 (40 nm). This range of grain sizes is consistent with non-epitaxial deposition of NPs. As mentioned previously for sample 2, the twins within these grains could have resulted from plastic deformation (deformation twins), or could have been present within the NPs before impaction (growth or annealing twins). In any case, it is clear that NPs on the larger end of the size distribution, like the ones observed here, do not consistently impact epitaxially.

Fig 7.3.f through 7.3.i are HRTEM pictures of the thinnest regions from the electron transparent window, and their associated fast Fourier transforms (FFTs). They show that dense, polycrystalline regions are present with a grain size of 5 nm – 20, in addition to the equiaxed grains that were described earlier. The microstructure of these regions could have resulted from epitaxial deposition of the smallest NPs in the size distribution of the NP jet, followed by subsequent coarsening by grain growth. Indeed, small NPs are more likely to deposit epitaxially because they are accelerated to higher impaction velocities than larger particles [5] for a fixed nozzle size and gas type.

**Figure 7.3 : Microstructure of Ag film deposited with a 1 mm nozzle, in 20 sucessive passes of the NP jet over a stainless steel substrate**

**(a) SEM image of an electron transparent cross-section of Ag film at a 54° tilted view**
**(b) Low magnification TEM showing the full thickness of film. 20 layers are visible, corresponding to 20 passes of the NP jet. There is no evidence of unablated MPs**
**(c) Bright field TEM image showing the stainless steel substrate, an interphase layer and the first 3 layers of NPs. Individual NPs can be seen both in the interphase region and the film layers**
**(d) HRTEM image of the interphase region, showing implantation of NPs in the interphase layer. This indicates the presence of a layer of soft material on the substrate. EDS revealed that the interphase layer consisted mostly of carbon**
**(e) Bright field image showing a dense polycrytalline microstructure. Equiaxed, twinned grains are highlighted in boxes 1 and 2 (digitally enhanced contrast)**
**(f) HRTEM image from the thinnest part of the electron-transparent window, revealing small overlapping gains (< 5nm)**
**(g) FFT of (f)**
**(h) HRTEM image showing a single, 20 nm grain**
**(i) FFT of (h)**

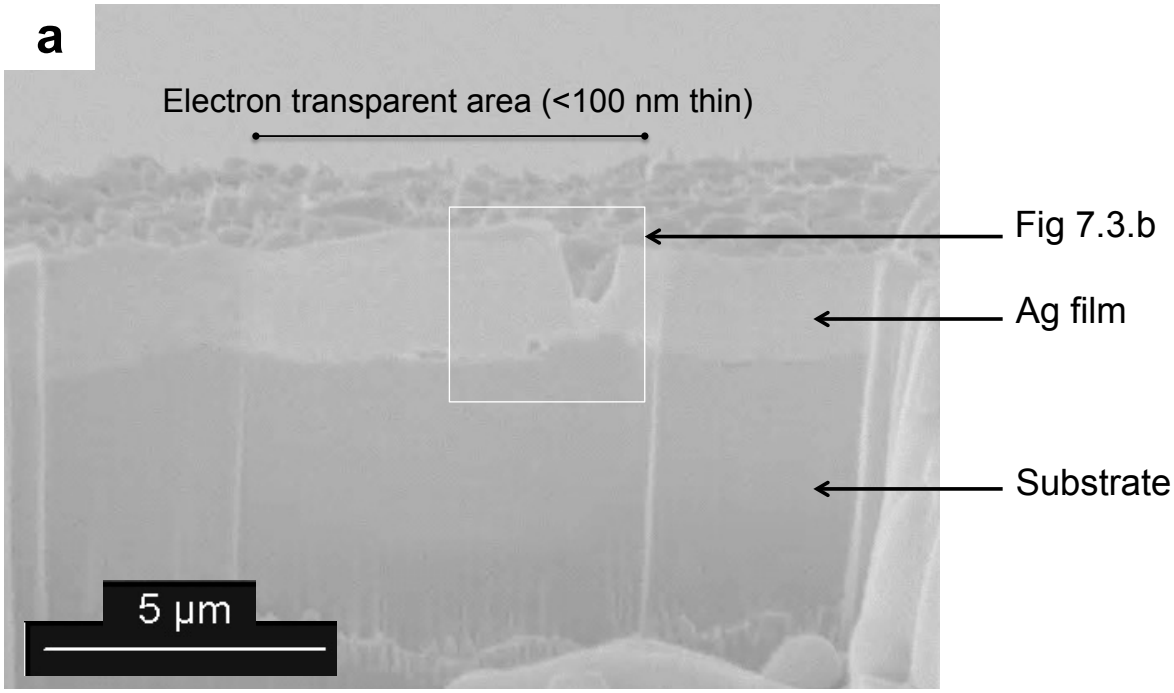

**Figure 7.3, continued**

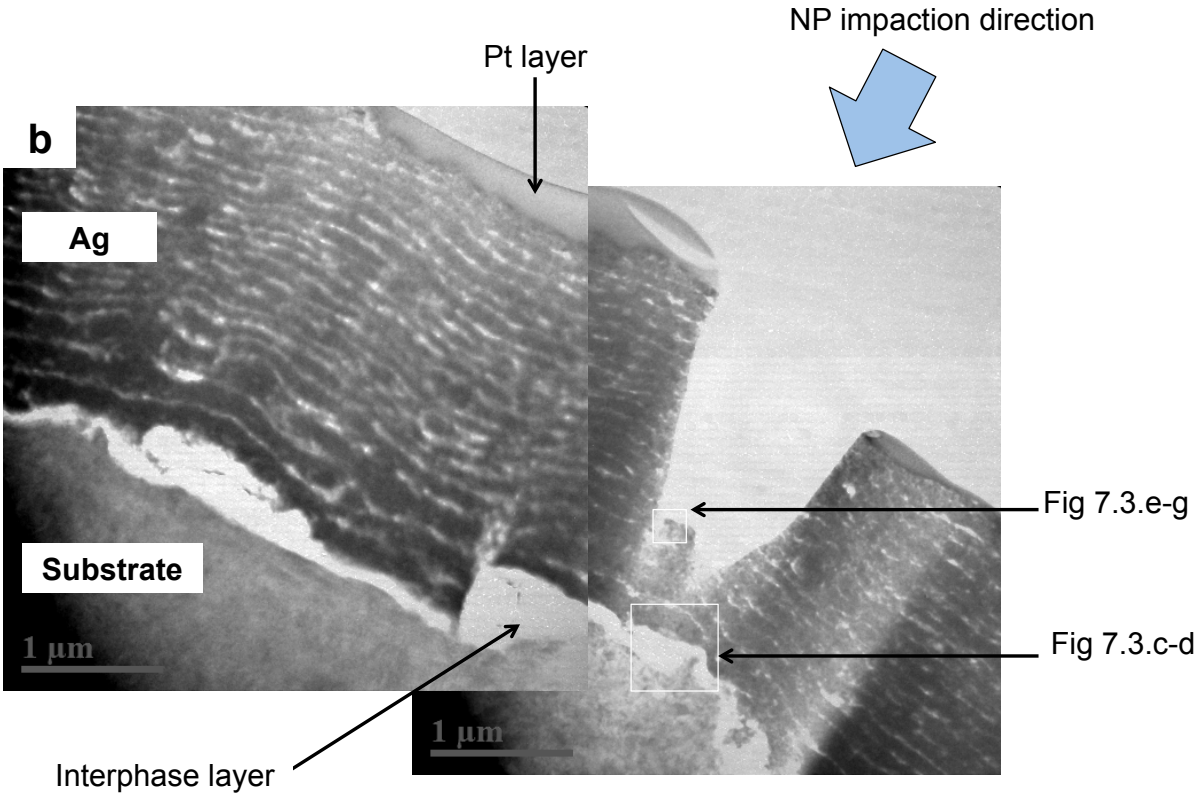


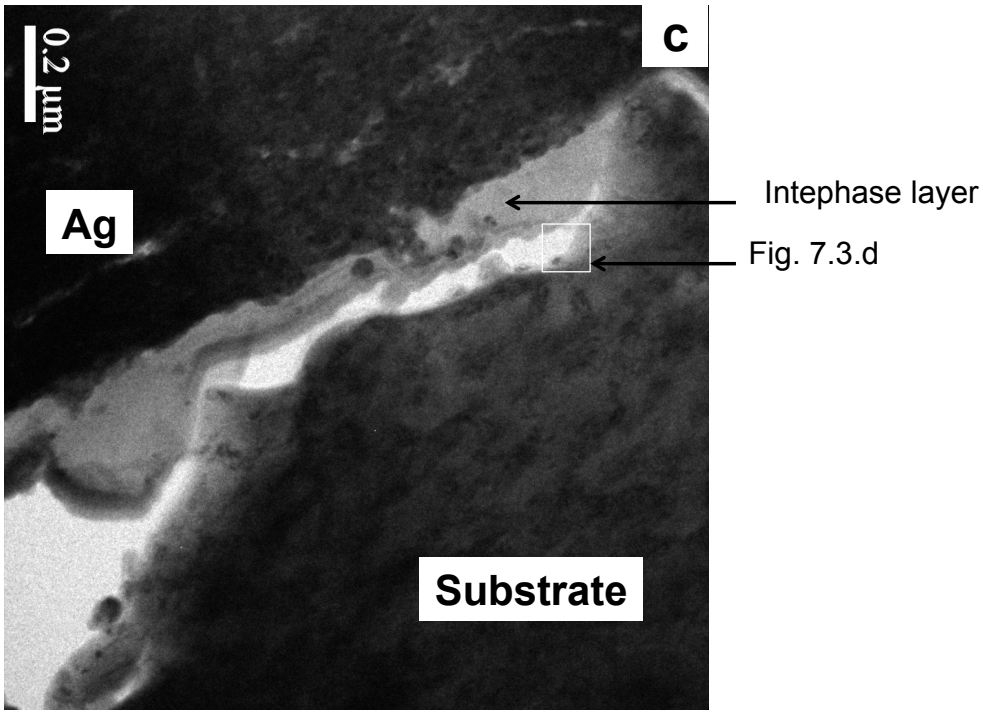

**Figure 7.3, continued**

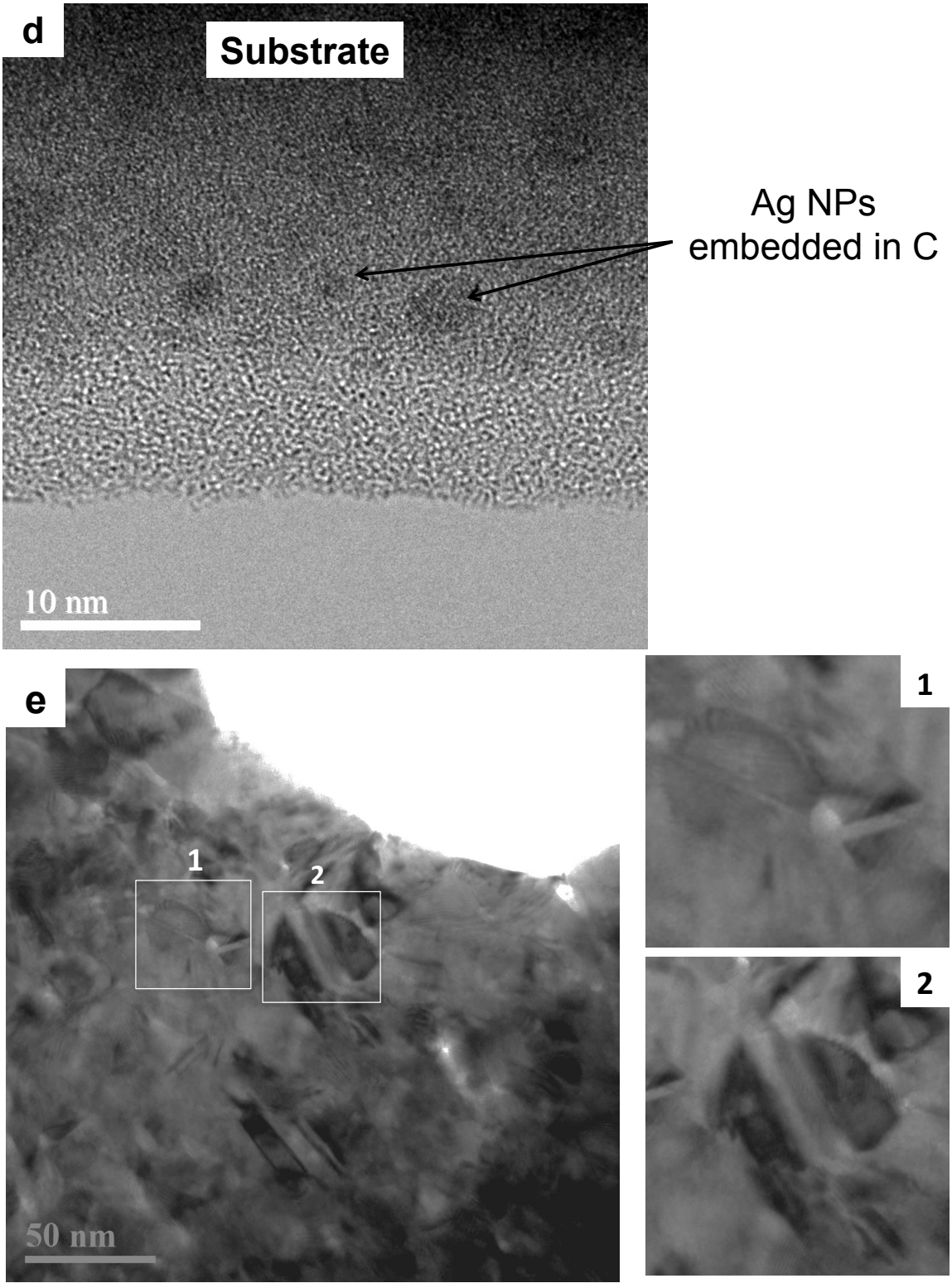

**Figure 7.3, continued**

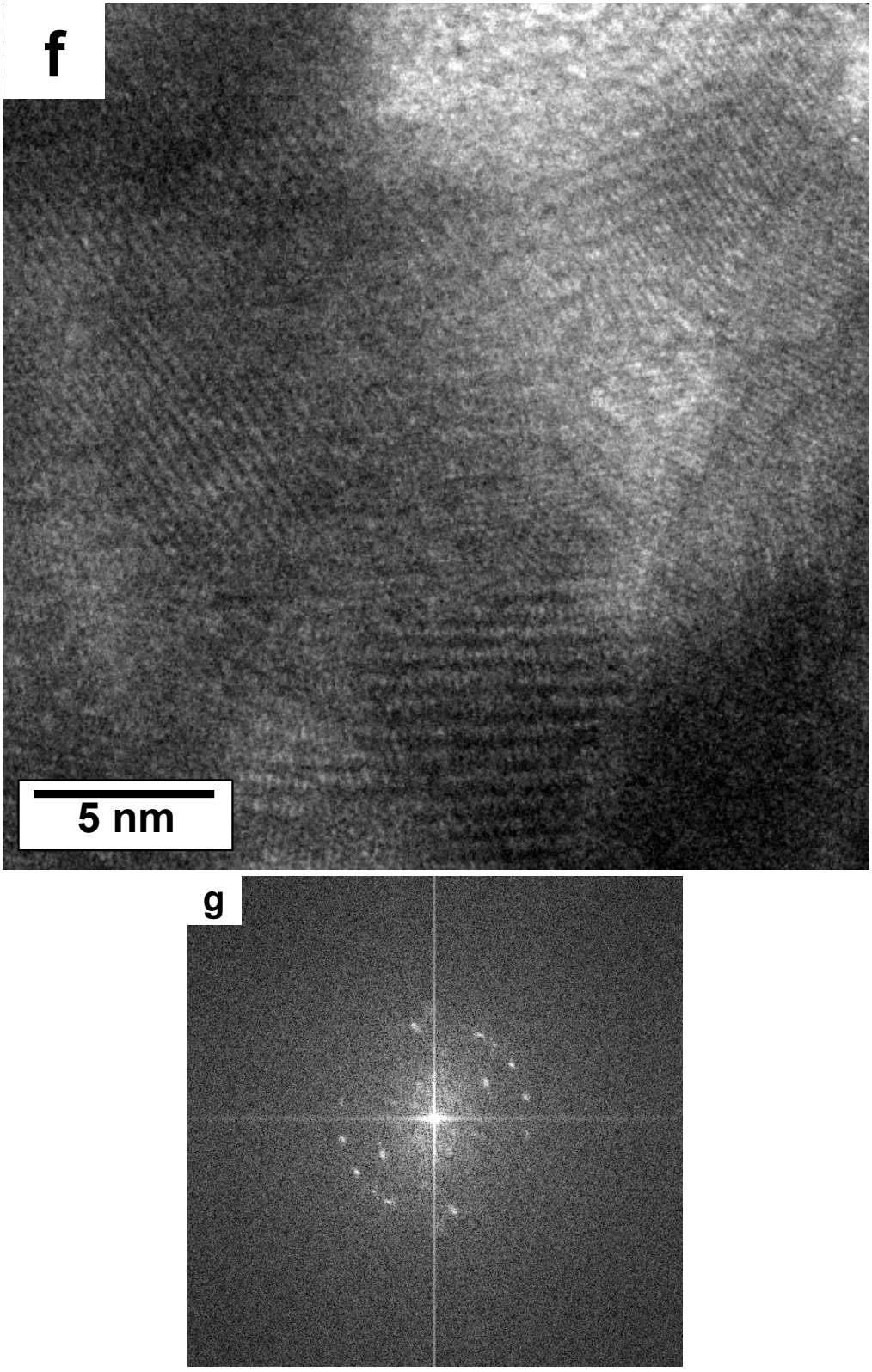

**Figure 7.3, continued**

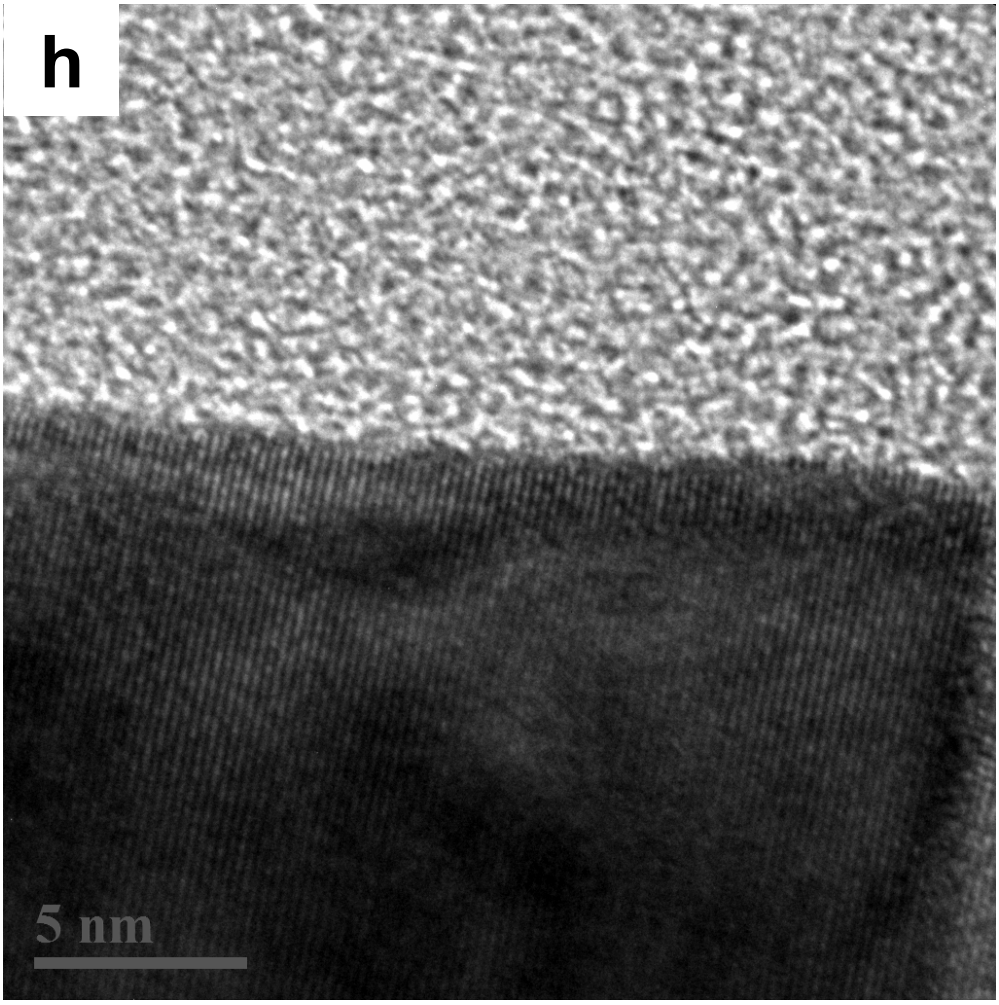


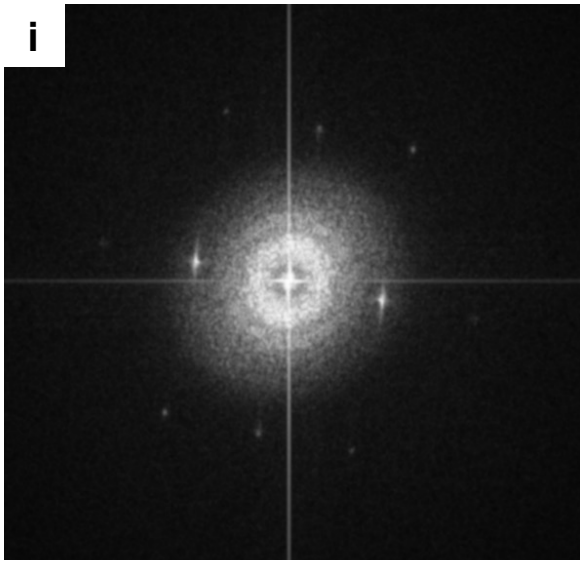

## 7.2 Composition analysis using EDS

Energy dispersive spectroscopy (EDS) analysis was conducted in different regions of sample 3. These regions are visible in Fig. 7.3.b and 7.3.c and include the regions that contain 1) the Ag film, 2) the stainless steel substrate, 3) the interphase layer between stainless steel and the Ag film, and 4) the Pt layer. EDS spectra were obtained using the same acquisition time and beam spot size for each region in order to be able to compare the composition from different regions. It is likely that the finite size of the electron beam resulted in the capture of spurious x-rays from outside of a single imaging region. Thus, some overlap of the signals from the different regions is expected.

The quantitative data from the EDS analysis are shown in Table 7.1. Cu is detected because the TEM grid is made of copper. This data shows the expected elements in the stainless steel substrate: Fe, C, Cr, Ni, Mn. This data also shows that the interphase layer consists mostly of organic material (high atomic % of C). Lastly, since no Ga contamination is detected except in the interphase layer, it shows that the TEM samples likely were not heavily damaged by the FIB specimen preparation process.

**Figure 7.4 : EDS spectra obtained from different regions of sample 3 (refer to Fig. 7.3.c)**
**(a) Stainless steel substrate (b) Ag film (c) Interphase layer**
**(d) Protective Pt layer from the FIB process**

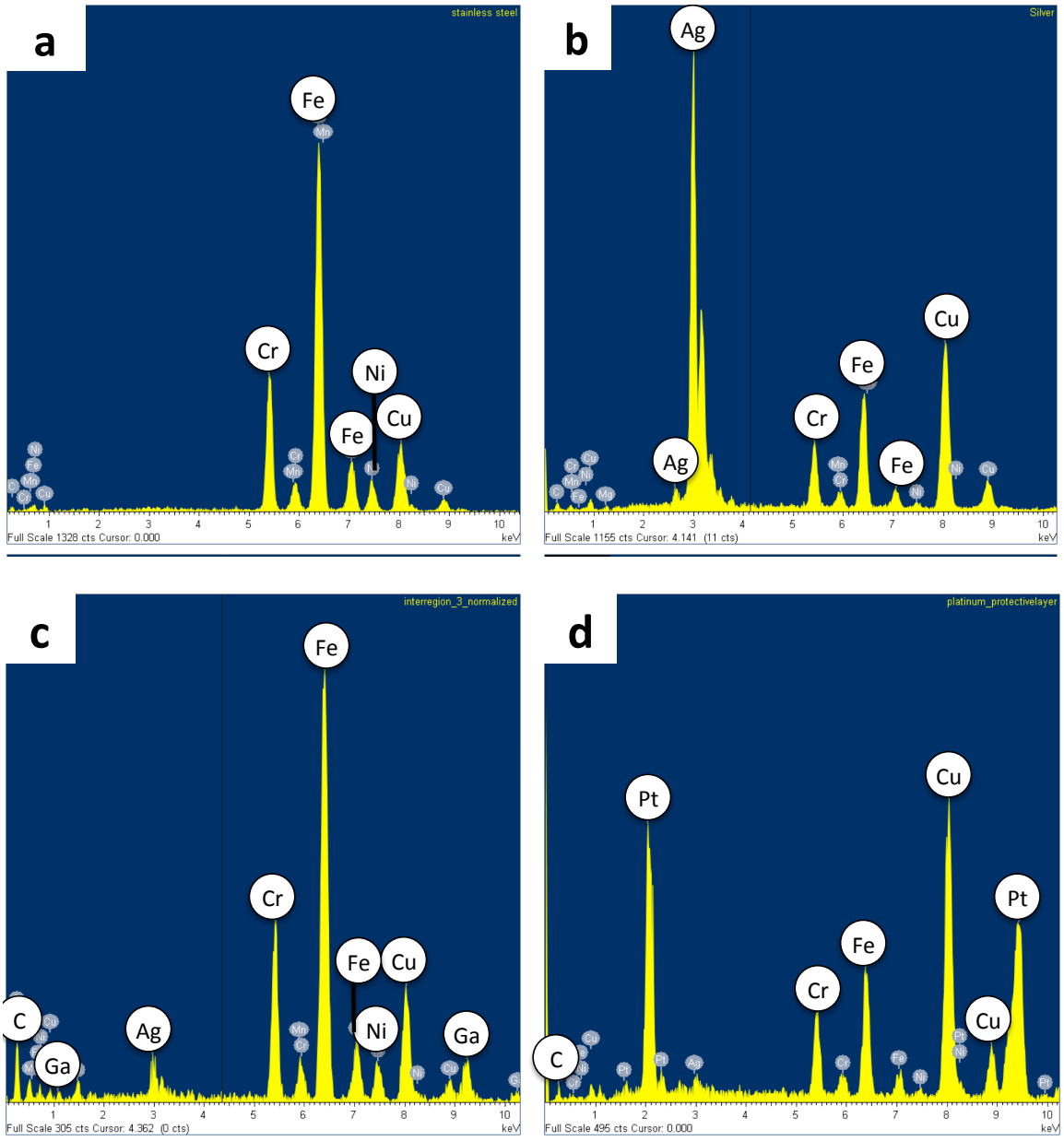

**Table 7.1: Quantitative elemental analysis obtained from different areas of Ag film using EDS. Table shows weight percentage and atomic percentage compositions calculated from the EDS spectra shown in Fig. 7.4**

| | (a) Substrate | | (b) Ag film | | (c) Interface | | (d) Pt layer | |
|---|---|---|---|---|---|---|---|---|
| | Weight % | Atomic % | Wt. % | At. % | Wt. % | At. % | Wt. % | At. % |
| **C** | 3.06 | 10.41 | 2.21 | 10.21 | 3.48 | 46.81 | 1.47 | 16.12 |
| **O** | - | - | - | - | 0.44 | 4.48 | - | - |
| **Al** | - | - | - | - | 0.16 | 0.99 | - | - |
| **Cr** | 16.95 | 13.31 | 6.38 | 6.82 | 2.01 | 6.25 | 2.89 | 7.34 |
| **Mn** | 2.08 | 1.55 | 0.96 | 0.97 | 0.23 | 0.68 | - | - |
| **Fe** | 70.52 | 51.54 | 15.94 | 15.87 | 7.61 | 22.02 | 5.76 | 13.6 |
| **Ni** | 8.84 | 6.14 | 1.01 | 095 | 1.03 | 2.84 | 0.48 | 1.07 |
| **Cu** | 26.55 | 17.05 | 42.94 | 37.57 | 3.8 | 9.65 | 24.62 | 61.12 |
| **Ga** | - | - | - | - | 2.4 | 5.55 | - | - |
| **Ag** | - | - | 51 | 26.29 | 0.49 | 0.74 | 0.71 | 0.87 |
| **Mg** | - | - | 0.57 | 1.31 | - | - | - | - |
| **Pt** | - | - | - | - | - | - | 14.61 | 9.88 |
| **Total** | 128 | 100 | 121.01 | 99.99 | 21.65 | 100.01 | 50.54 | 110 |

## 7.3 Discussion of film microstructures

### 7.3.1 Influence of NP kinetic energy on film density

Samples written with the 0.25 mm nozzle exhibited a continuous, cohesive microstructure. Yet, they were also quite weak and fractured easily during the preparation of electron transparent samples. For example, all but one of the windows collapsed before the final thinning stages of the FIB process. The relative weakness of these samples is consistent with previously measured porosity of 30% for samples made under similar processing conditions [22]. It was easier to manufacture TEM windows from samples deposited with 0.5 and 1 mm nozzles, which suggests that the higher impaction energy of the NPs resulted in films with lower porosity and therefore higher strength.

The TEM observations themselves are consistent with an increase in relative density as the impaction energy of NPs is increased, This is particularly evident in Fig. 7.1.c, which shows the porous nature of the film deposited with the 0.25 mm nozzle when compared to Figs. 7.2.b and 7.3.e which both show denser film microstructures for films deposited with 0.5 and 1 mm nozzles. These observations are also consistent with MD simulations that predict a transition from porous to higher density films as the impaction energy is increased [5].

### 7.3.2 Challenges for direct measurements of grain size using TEM

It is important to highlight the challenges in obtaining direct grain size measurements using TEM. In addition to the known difficulties in fabricating cross-sectional TEM samples, it was particularly challenging with these samples because the adhesion between the films and the substrate was poor. The high porosity for films deposited at lower impaction energy also greatly increased the difficulty in fabricating mechanically stable and yet electron-transparent TEM windows.

Ideally, the grain size distribution could be measured for each sample either directly from bright field imaging or using an orientation imaging technique where information about grain orientations are obtained from backscattered electrons. Orientation imaging methods also give information about the relative misorientations of the grains so that information about preferred textures is also obtained. However, existing orientation imaging methods such as D-STEM [40] are very difficult to implement for grain sizes of less than 5 nm, such as the films produced for this study. These techniques also require an electron transparent window that is large enough to yield measurements on a statistically

significant number of grains. Perhaps the greatest challenge is that all of the above must occur while ensuring that the sample is uniformly one grain thick or less, because samples that are thicker will convolute the information from overlapping grains through the thickness. Unfortunately, such samples could not be produced for this study.

Nevertheless, the TEM observations presented here bring valuable insight. In particular, they show the complexities of the microstructures that are present in LAMA-deposited films and, although quantitative measurements proved to be impossible, the conclusions drawn from qualitative observations about the densities of the films, the grain sizes, and the defects in the films were consistent.

### 7.3.3 Influence of impaction energy on grain morphology and grain size

For all samples, the final microstructures exhibit a large variation in grain sizes. This reflects the range of possible impaction regimes for NPs, given the range of NP sizes in the LAMA-produced NP aerosol [29], and the resulting range of impaction energies. For example, larger NPs (up to 40 nm) are still visible in the final films microstructures and often contain twins, as shown in the EM observation (Fig. 7.2.c, 7.2.f, 7.3.e). However, particles smaller than a few nanometers are largely absent from the films, although they were observed embedded in carbon interlayers. This suggests that the finer particles are present in the depositing aerosol, but are eliminated by a coarsening process upon impaction.

### 7.3.4 Film growth mechanisms

#### 7.3.4.1 Columnar microstructure in Ag deposited using a 0.25 mm nozzle

For sample 1, SEM images of film cross sections (Fig 7.1.b) revealed that fan-like columnar structures formed upon impaction of NPs. These columns seem to originate from the center of the Ag line and then radiate outward as they grow from the base. Although the mechanisms for the formation of the columnar structures is not known, it is possible that these columns could be due to a higher density of impacting NPs in a narrow region, leading to a rapid drop in film growth rate away from the center of the NP jet. Such a gradient in growth rate would likely favor such vertical features. The jet of impacting NPs has a higher density at the center and thus the overall force exerted on the growing vertical structures by the impacting NPs is likely to push these structures to the side, explaining the fan-like morphology. Although the proposed mechanism for the formation of the fan-like morphology is speculative, it is consistent with the observed morphologies and the known hydrodynamics under the deposition jet. It would be difficult to confirm the proposed mechanism using MD simulations since the required volumes necessary to simulate the evolution of this morphology is currently beyond the scope of what can be simulated in reasonable times.

#### 7.3.4.2 Layered microstructure of Ag deposited using 0.5 mm and 1 mm nozzles

For the first time, cross sectional TEM observations of films produced via LAMA were conducted. They revealed a layered structure, with each Ag layer corresponding to one pass of the substrate under the NP jet. The layering is clearly visible in Fig. 7.3.b and subsequent analysis showed that the interphase present between the Ag layers consisted

primarily of carbon. The presence of a carbon layer between successive layers of Ag, suggests that organic impurities were present in the deposition chamber. The growth rate of this impurity layer can be roughly estimated by dividing the thickness of the gap between two successive Ag layers. From Fig. 7.3.c., the gap thickness is about 30 nm. The time between two passes of the NP jet over the substrate is 5 s (5 mm at a fixed translation velocity of 1 mm/s). This leads to an estimated growth rate of the organic impurity layer of 6 nm/s.

The layering phenomenon was observed in samples 2 and 3, which were deposited with the 0.5 and 1 mm diameter nozzles, respectively, but not in sample 1, which was deposited with the 0.25 mm nozzle. As noted previously, there are several changes that occur as the nozzle size is increased. Not only does the deposition energy increase, but the macroscopic morphology of the approximately Gaussian profile of the lines also changes. Specifically, the breadth of the lines increases and the NPs are deposited more uniformly over a larger area as the nozzle size is increased. Because changes in both impaction energy and film morphology occur as the nozzle size is increased, it is not possible to ascribe the layering to a specific change in deposition parameter and further work will be needed to clarify the cause of the layering.

## 7.4 Conclusions

The microstructures of LAMA-deposited Ag films were observed directly using SEM and TEM cross-sectional samples. Samples deposited using acceleration nozzles with diameters of 0.25, 0.5 and 1 mm exhibited a complex polycrystalline grain structure. Direct evidence was presented that shows epitaxial deposition of small, NPs (<5 nm; Fig.

7.1.f) that were deposited at high impaction energies. Evidence of non-epitaxial deposition of large NPs (up to 40 nm) that deposited at lower impaction energies is suggested by Fig. 7.2.b-c,f and Fig. 7.3.e, but the equiaxed grains observed in these TEM images could also have resulted from grain growth. There is also evidence of epitaxial deposition of NPs over large areas (300 $nm^2$) compared the particle size (see Figs. 7.2.d and 7.2.e). Such regions of epitaxial deposition would be expected to increase the mean grain size in the film compared to the size of the impacting NPs. This suggests that impaction at even higher impaction energies might lead to an even more significant increase in grain size. However, if the goal is to produce an epitaxial film, it is likely that higher impaction velocities alone would not be sufficient. A single crystal substrate free of amorphous organic or oxide layers would be required, in order for the first layer of deposited NPs to epitaxially align with the substrate.

The complexity of the microstructures of LAMA-deposited materials reflects the wide range of potential impaction regimes, even when the impaction conditions are fixed to a particular nozzle size and gas type, because the impaction energies also depend on particle size. In order to find a theoretical threshold for minimum kinetic energy for epitaxial deposition, it is necessary to better understand multiple particle impacts. In Chapter 5, it was shown that a range of behaviors is possible for single particle impactions; in some cases a single particle impaction leads to an increase in grain size compared to the impacting NP, and in other cases it leads to a decrease in grain size. There is even more complexity in the case of multiple particle impacts during film growth, as demonstrated by the current SEM and TEM observations. Therefore more work is needed in closely coupling MD simulations of multiple particle impacts to TEM

observations to better understand the mechanisms of film formation and growth. If successful, this could lead to processing conditions that result in epitaxial deposition of films from LAMA-produced NPs.

# Chapter 8: Study of film microstructure using XRD

In this chapter, the influence of increasing the kinetic energy of impacting nanoparticle (NPs) on the grain size of LAMA-deposited Ag films is studied using X-ray diffraction (XRD). More precisely, peak broadening analysis enables to extract information about the size of crystallographic domains that diffract X-rays coherently (diffracting domain size) rather than grain size. A peak broadening analysis was conducted on films deposited with 0.25, 0.5 and 1 mm nozzles, and then the size of diffracting domains was extracted from the peak breadth. This analysis complements the direct observations of grain morphology by TEM presented in the previous chapter, as it provides the average grain size over an area that is much larger than the impacting particle size. The various assumptions necessary to extract the grain size information from the XRD diffraction patterns (DP) are discussed, as well as the implications for interpreting the results. This study revealed an obvious anisotropy in peak broadening, which is also discussed. Additionally, a pole figure analysis was conducted to study the texture of LAMA-deposited Ag, and is presented in the second section.

## 8.1 Diffracting domain size

The X-ray DPs for samples deposited with 0.25, 0.5 and 1 mm nozzles are presented in Fig. 8.1. Williamson-Hall (W-H) plots were obtained to separate the effects of crystallite size and microstrain on the peak broadening, as shown in Fig. 8.2. The error bars on the plots reflect the 95% confidence intervals for the fwhm parameter obtained from fitting the peaks with a Lorentzian model (see Eq. 4.3, and standard error propagation in subsequent calculations). The relatively small size of the error bars is a reflection of the good quality of the Lorentzian fit to the data. The only data point with a large error bar is the {400} reflection, that was obtained only for the 0.25 mm sample, due to the low intensity and low signal-to-noise ratio for this reflection.

It appears from the W-H plots that the data points do not align to form a straight line, as is expected if the diffracting domains were equiaxed. The lack of a linear relation between the $B \cdot \cos\theta$ and $\sin\theta$ does not allow the strain component to be extracted using the W-H method. However, it is reasonable to assume that the strain in the deposited films is not significant. For example, depositions onto polymer substrates did not reveal evidence of sample curvature (which would occur if in-plane residual stresses were present from deposition) [22], and MD simulations have not shown evidence of nanoscale residual stresses following deposition (personal communication with Tushar Chitrakar). The strain was therefore neglected, and the diffracting domain size was calculated for each reflection assuming zero strain. Neglecting the strain means that the calculated values for the domain size represent a lower bound to the real domain size, since all other sources that could cause peak broadening are neglected.

The calculated domain size is shown for each crystallographic direction in Table 8.1. The averages for the first 4 reflections were calculated and are given in Table 8.2. The calculated sizes from the same family of reflections, for example {111} and {222}, were taken individually for the calculation of the average value. The results show a small but consistent increase in domain size compared to the size of impacting NPs, and a small decrease in domain size as the kinetic of impacting NPs is increased. Some care should be taken in interpreting whether there are statistical differences between grain sizes for films produced using different nozzle sizes, given the assumptions made in the analysis.

Anisotropy in W-H plots, where non-linear relationships occur between $B \cdot \cos\theta$ and $\sin\theta$, have been reported previously in fcc nanocrystalline materials, both experimentally [23],[41] and by computer simulation [42],[43]. For example, computer simulation of X-ray diffraction patterns of a material with 10 nm, defect-free grains and high angle grain boundaries resulted in a nearly linear W-H plot. However, when twin defects or dislocations were introduced within the grains, a non-monotonic W-H plot was observed, with a distinct influence of crystallographic direction on peak broadening. In particular, when twin defects were introduced within the grains, the {111} family of DF were the least affected and the {200} family of DF was the most affected by the additional broadening. The authors attributed this effect to the fact that for the {111} family, there is always one direction that is not affected by the twin or stacking fault, whereas all {100} planes are affected in the same way by twins. In Chapter 7, we saw from the TEM micrographs that LAMA-deposited samples clearly show a high density of twins. Thus the XRD results are consistent with twin/stacking fault induced W-H

anisotropy. Thus, the experimental evidence strongly supports that the observed anisotropy in the W-H plots results from twinning.

**Figure 8.1: X-ray diffraction patterns obtained from Ag films deposited with increasing NP impaction energy**

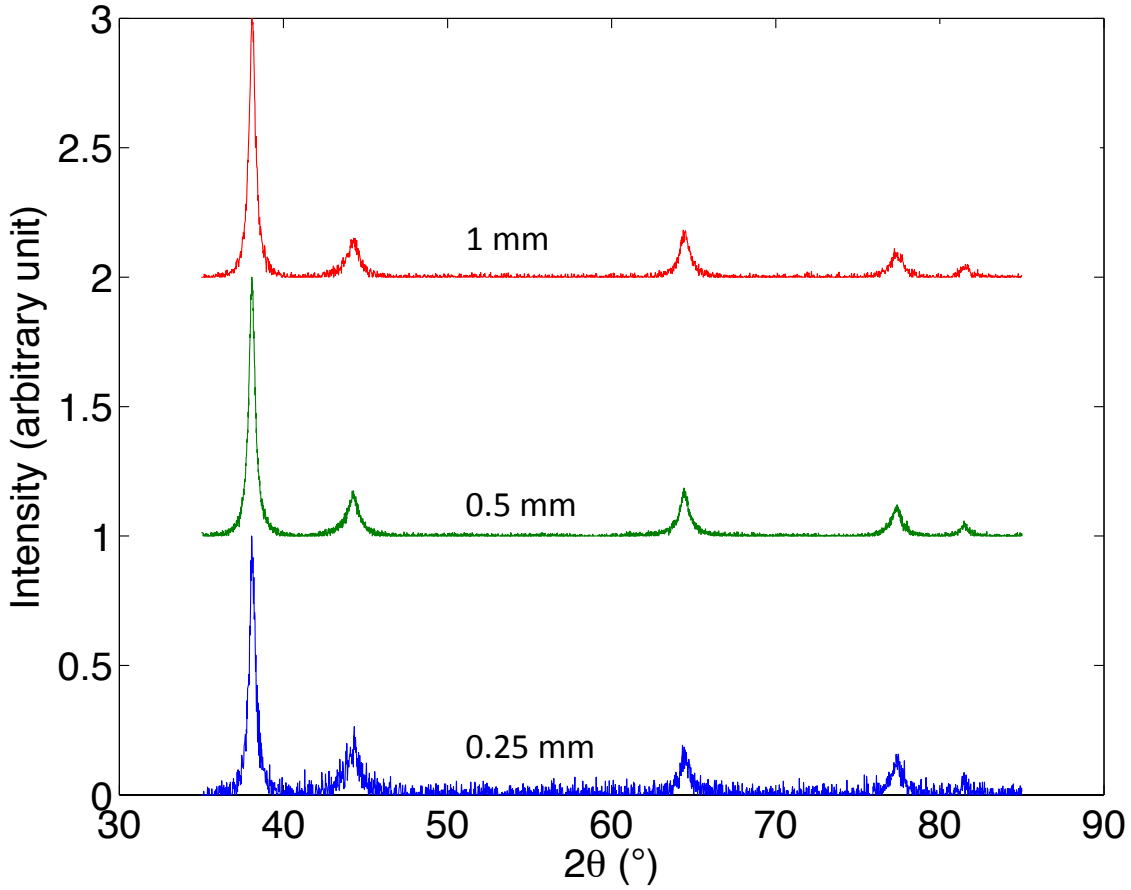


Two hypotheses could explain this influence of increasing the kinetic energy on the microstructure of LAMA-deposited Ag: (1) An actual decrease in grain size with increasing kinetic energy of NPs is possible, and evidence was presented in Chapter 5 that NP impaction could lead to a decrease in grain size compared to particle size. (2) An increase in kinetic energy could also result in an increase of the fraction of NPs that land epitaxially and recrystallize with a high stacking fault density (like shown in Fig. 5.4).

This would produce films with a larger grain size, but a smaller domain size as a result of the high twin/stacking fault density. Since both mechanisms would produce W-H plots with more anisotropy, it is difficult to determine which mechanism is occurring the LAMA-deposited films.

**Figure 8.2: Williamson-Hall plots obtained from the data shown in Fig. 8.1**

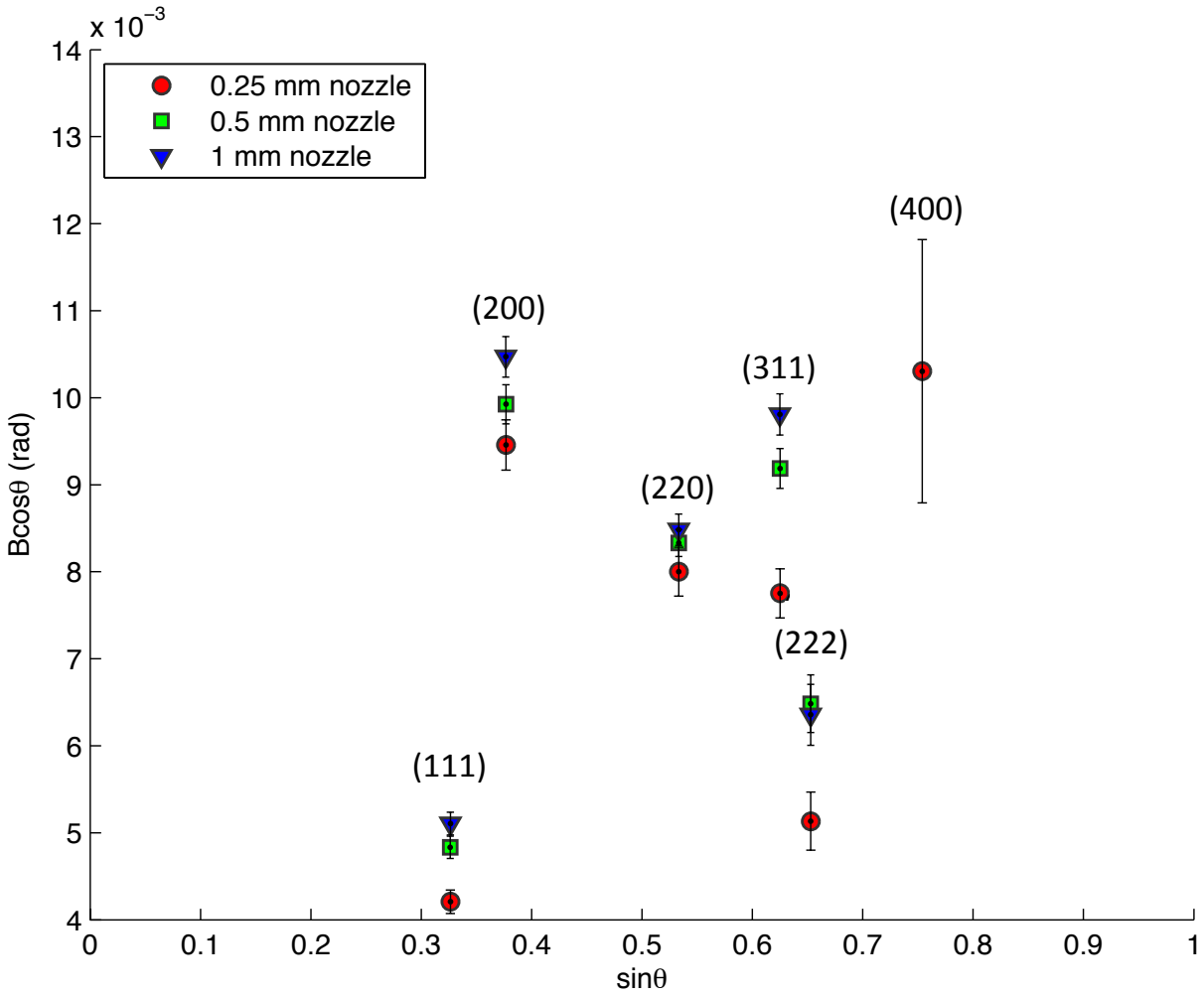

**Table 8.1: Diffracting domain size calculated for various crystallographic directions**

| Nozzle *mm* | {hkl} | Diffracting domain size *nm* | Error % | Error *nm* |
|---|---|---|---|---|
| 0.25 | 111 | 33.0 | 6.4 | 2.1 |
| | 200 | 14.7 | 6.1 | 0.9 |
| | 220 | 17.3 | 7.0 | 1.2 |
| | 311 | 17.9 | 7.3 | 1.3 |
| | 222 | 27 | 13.0 | 3.5 |
| | 400 | 13.5 | 29.4 | 4.0 |
| 0.5 | 111 | 28.7 | 5.3 | 1.5 |
| | 200 | 14 | 4.5 | 0.6 |
| | 220 | 16.7 | 3.7 | 0.6 |
| | 311 | 15.1 | 5.0 | 0.8 |
| | 222 | 21.4 | 10.2 | 2.2 |
| 1 | 111 | 27.2 | 5.1 | 1.4 |
| | 200 | 13.3 | 4.5 | 0.6 |
| | 220 | 16.4 | 4.2 | 0.7 |
| | 311 | 14.1 | 4.8 | 0.7 |
| | 222 | 21.8 | 11.0 | 2.4 |

**Table 8.2 : Average diffracting domain size, calculated from {111}, {200}, {220} and {311} reflections, for Ag films deposited with increasing NP kinetic energy.**

| Nozzle *mm* | Diffracting domain size *nm* | Error % | Error *nm* |
|---|---|---|---|
| 0.25 | 20.7 | 7 | 1.4 |
| 0.5 | 18.6 | 5 | 0.9 |
| 1 | 17.7 | 4.5 | 0.8 |

## 8.2 Texture

The diffracted intensities of {200} planes ($2\theta = 44.27°$) were measured as a function of orientations of the films relative to the X-ray beam to investigate whether any preferred orientation of the {200} planes relative to the surface of the deposition substrate exists. Two samples were studied: Ag deposited on amorphous soda-lime glass, and Ag on {100} Si single crystal substrate. Note that although the silicon substrate is crystalline, under ambient conditions, a thin amorphous layer of oxide is present on the surface.

Fig. 8.3 shows the measured intensity of the {200} peak vs. polar angle (α) for a particular azimuthal angle (β = 0˚) . The data shown here was obtained from an Ag sample deposited on glass, but similar results were obtained for the other sample deposited onto Si. A distinct change in intensity with angle is observed. However, it is important to note that, on an absolute scale, the differences from minimum to maximum in intensity with angle are only about a factor of 3.5. The two-fold symmetry in the plot suggests that {200} planes may be oriented along or perpendicular to the deposition direction or specimen surface. However, this type of texture is unusual in films, which instead often exhibit a wire texture that exhibits four-fold symmetry [47]. It is possible that the observed texture is an artifact in the measurement, but the source of that artifact was not obvious. The magnitude of the observed variations in intensities with angle suggest that if a texture was present, it was not a strong preferred texture. The θ - 2θ plots are also consistent with a material that does not exhibit strong texture since a strong preferred texture would reveal itself in these plots as a sharp differences in intensities for each diffraction peak compared to those predicted from theory; this was not observed.

**Figure 8.3 : Typical slice from {200} pole figure obtained from LAMA-deposited Ag sample for β = 0° deposited onto soda-lime glass showing the dependence on α. Qualitatively similar plots were obtained for other values of β and when the sample was deposited onto Si.**

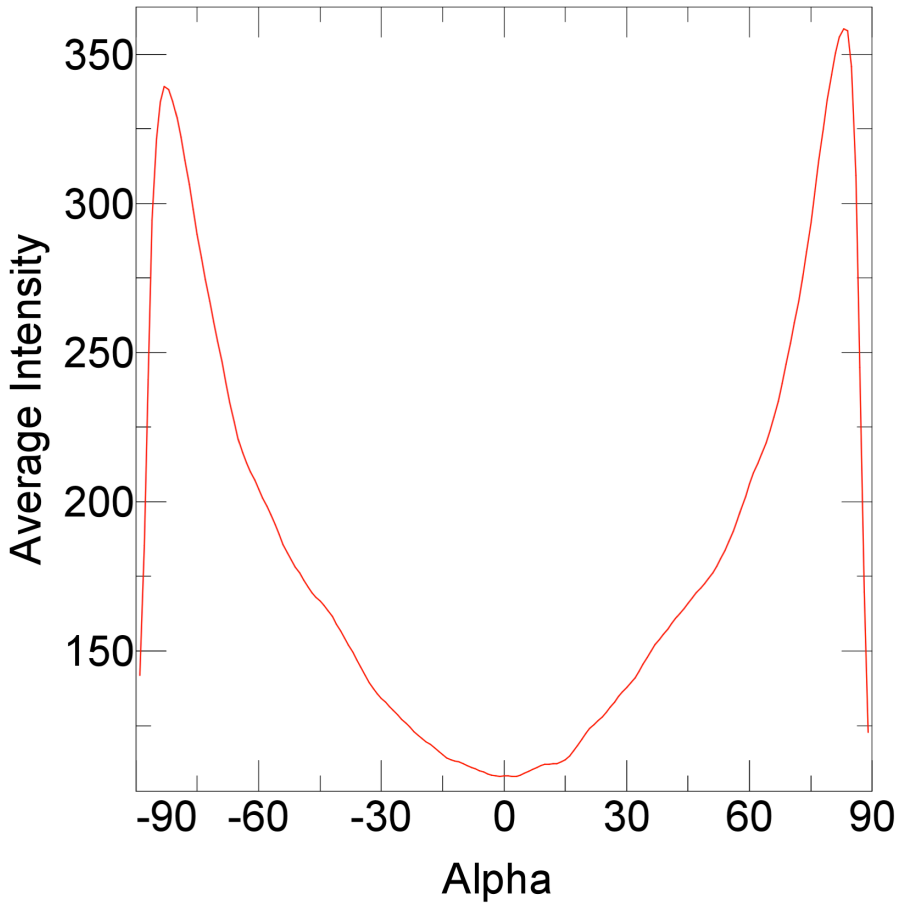

## 8.3 Conclusions

In this chapter, the use of XRD was explored to characterize the microstructures of deposited films. XRD techniques are useful because they can probe the average size of diffracting domains and average preferred crystallographic texture present in the films. The domain size obtained from such analyses is typically related to the grain size in nanograined materials, but in films such as those studied here, which were shown in the previous two chapters to contain high density of twins/stacking faults, the domain size may also be related to twin/stacking fault density.

Texture measurements made using pole figures did not reveal strong texture in the LAMA-deposited films. Analysis of the peak broadening from XRD results revealed an anisotropy in the W-H plot that is consistent with a high density of twin/stacking faults. This anisotropy precluded the use of the standard W-H analysis in which the microstrain and the domain size are treated separately. Instead, it was assumed that the contributions to the peak broadening from microstrain were negligible and that the only contributions were from grain size/domain size effects. This assumption was justified by previous experiments and by previous MD simulations.

With these assumptions, the analysis revealed that the domain sizes decreases slightly when the impaction energy was increased. Two hypothesis were discussed to explain the mechanisms that could cause this result: 1) the grains break up into smaller grains upon impaction or 2) the particles deposit epitaxially, but with a high density of twins/stacking faults. Since both mechanisms have been shown to be possible from MD simulations presented in the previous chapters, the dominant mechanism cannot be

ascertained from XRD analysis alone. Further, more detailed coupling between experiments and MD simulations may be necessary to understand this phenomenon.

# Chapter 9: Conclusions and future work

In this dissertation, direct observations of the microstructures produced by impaction of individual NPs were presented. TEM micrographs for specimens prepared under nominally the same conditions showed both epitaxial deposition of NPs as well as non-epitaxial deposition are possible. This study showed that there are a variety of possible mechanisms occurring upon impact of NPs, and the TEM observations enabled identification of some of these. A key limitation of using TEM observations for the study of mechanisms of deformation and sticking that occur during very fast time scales is that this technique is limited to the observation of only the final state after the impaction event has concluded.

Coupling MD simulations with the experimental results allowed more in depth understanding of the mechanisms that occur during the impaction process. To illustrate this, a particular a NP-on-NP impact event based on a TEM observation was studied in detail using a series of snapshots in time from MD simulations. The simulation enabled the decomposition of the impaction event into a sequence of events that include: 1) amorphization of the material in the vicinity of the impact in both nanoparticles, 2) matter flow by NP splitting and rotation as well as deformation twinning in the larger NP, 3) crystallization from the amorphous regions leading to either perfect crystals or, more often, crystals that contain annealing twins, and 4) grain coarsening by grain boundary motion. This sequence of events and the final state of the particles observed in the simulation is consistent with some of the final microstructures observed in TEM, but considerable variations were observed experimentally in the final states of particles

produced under nominally identical conditions. It was suggested that, in this range of conditions, the final state is sensitive to details such as the relative misorientation of the impacting particles.

The variety of possible mechanisms illustrates the complexity of the NP impaction process, and explains the complex microstructure of the materials produced via the LAMA process. Establishing a quantitative model to predict the right processing parameters to control the final microstructure would enable us to create advanced materials that fully exploit the advantages of the LAMA process. However it remains a challenge to this point. Increasing NP speed and reducing NP size still remain viable strategies to achieve epitaxial deposition of films.

Chapters 6 and 7 studied film growth from impaction of Ag NPs, where the velocity of impacting NPs has been increased. It was shown that improvements made to the system by modifying the X-Y stage control and through the use of larger deposition nozzle sizes improve the film quality from a macroscopic and microscopic point of view. Specifically, larger area deposits with more uniform thicknesses, significantly higher optical quality, and higher densities were demonstrated.

The microstructures of LAMA-deposited Ag films were observed directly using SEM and TEM cross-sectional samples. Samples deposited using acceleration nozzles with diameters of 0.25, 0.5 and 1 mm exhibited a complex polycrystalline grain structure. Direct evidence was presented that shows epitaxial deposition of small NPs (<5 nm) that deposited at high impaction energies. The presence of equiaxed grains, 20-40 nm in size, could result from non-epitaxial deposition of large NPs that deposited at lower impaction energies, or could result from epitaxial deposition of smaller NPs followed by grain

growth. There is also evidence of epitaxial deposition of NP over large areas (300 $nm^2$) compared the particle size in some of the films. Such regions of epitaxial deposition would be expected to increase the mean grain size in the film compared to the size of the impacting NPs. This suggests that impaction at even higher energies might lead to an even more significant increase in grain size. However, if the goal is to produce an epitaxial film, it is likely that higher impaction velocities alone would not be sufficient. A single crystal substrate free of amorphous organic or oxide layers would be required, in order for the first layer of NPs to epitaxially align with the substrate. To achieve epitaxial growth of films, the choice of substrate material should also favor heteroepitaxy in the deposition of the first later of NPs, and MD simulation could be useful in determining good substrate materials that favor this.

The complexity of the microstructures of LAMA-deposited materials reflects the wide range of potential impaction regimes, even when the impaction conditions are fixed to a particular nozzle size and gas type because the impaction energies also depend on particle size. In order to find a theoretical threshold for minimum kinetic energy for epitaxial deposition, it is necessary to better understand multiple particle impacts. In Chapter 5, it was shown that a range of behaviors is possible for single particle impactions; in some cases a single particle impaction leads to an increase in grain size compared to the impacting NP, and in other cases it leads to a decrease in grain size. There is even more complexity in the case of multiple particle impacts during film growth, as demonstrated by the current SEM and TEM observations. Therefore more work is needed in closely coupling MD simulations of multiple particle impacts to TEM observations to better understand the mechanisms of film formation and growth. If

successful, this could lead to processing conditions that result in epitaxial deposition of films from LAMA-produced NPs.

The size of coherent domains in Ag samples deposited by impaction of NPs has been estimated using XRD and the influence of increasing the NP impaction energy was studied. An increase in grain size at higher impaction energies would be intuitive since it favors epitaxial deposition of NPs [6]. In this study, samples deposited with higher NP impaction energy exhibited a slightly smaller average coherent domain size, that could be due to either a decrease in grain size, or to an increase in the fraction of NPs that deposit epitaxially, coupled with an increase in stacking fault density. Studying the influence of increasing the impaction energy on coherent domain size, for materials other than Ag, that do not have such a propensity to form stacking faults upon crystallization would enable confirmation of one of these hypotheses.

# References


[1] W. T. Nichols, “Production and controlled collection of nanoparticles: toward manufacturing of nanostructured materials,” 2002.

[2] W. T. Nichols, G. Malyavanatham, D. E. Henneke, J. R. Brock, M. F. Becker, J. W. Keto, and H. D. Glicksman, “Gas and pressure dependence for the mean size of nanoparticles produced by laser ablation of flowing aerosols,” J. Nanoparticle Res., vol. 2, no. 2, pp. 141–145, 2000.

[3] C. Huang, W. T. Nichols, D. T. O’Brien, M. F. Becker, D. Kovar, and J. W. Keto, “Supersonic jet deposition of silver nanoparticle aerosols: Correlations of impact conditions and film morphologies,” J. Appl. Phys., vol. 101, no. 6, p. 064902, 2007.

[4] K. Nordlund, T. T. Järvi, K. Meinander, and J. Samela, “Cluster ion–solid interactions from meV to MeV energies,” Appl. Phys. A, vol. 91, no. 4, pp. 561–566, 2008.

[5] H. Haberland, Z. Insepov, and M. Moseler, “Molecular-dynamics simulation of thin-film growth by energetic cluster impact,” Phys. Rev. B, vol. 51, no. 16, p. 11061, 1995.

[6] K. Meinander, K. Nordlund, and J. Keinonen, “Size dependent epitaxial cluster deposition: The effect of deposition energy,” Nucl. Instrum. Methods Phys. Res. Sect. B Beam Interact. Mater. At., vol. 242, no. 1, pp. 161–163, 2006.

[7] L. B. Han, Q. An, S. N. Luo, and W. A. Goddard, “Ultra-elastic and inelastic impact of Cu nanoparticles,” Mater. Lett., vol. 64, no. 20, pp. 2230–2232, 2010.

[8] A. Papyrin, V. Kosarev, S. Klinkov, A. Alkhimov, and V. M. Fomin, Cold Spray Technology. Elsevier, 2006.

[9] H. Assadi, F. Gärtner, T. Stoltenhoff, and H. Kreye, “Bonding mechanism in cold gas spraying,” Acta Mater., vol. 51, no. 15, pp. 4379–4394, 2003.

[10] J. Pattison, S. Celotto, R. Morgan, M. Bray, and W. O’Neill., “Cold gas dynamic manufacturing: A non-thermal approach to freeform fabrication,” Int. J. Mach. Tools Manuf., vol. 47, no. 3–4, pp. 627–634, Mar. 2007.

[11] M. Grujicic, C. L. Zhao, W. S. DeRosset, and D. Helfritch, “Adiabatic shear instability based mechanism for particles/substrate bonding in the cold-gas dynamic-spray process,” Mater. Des., vol. 25, no. 8, pp. 681–688, 2004.

[12] R. H. Morgan, C. J. Sutcliffe, J. Pattison, M. Murphy, C. Gallagher, A. Papworth, P. Fox, and W. O’Neill, “Cold Gas Dynamic Manufacturing–A new approach to Near-Net Shape Metal Component Fabrication,” in MRS Proceedings, 2002, vol. 758, pp. LL2–6.

[13] K. Balani, A. Agarwal, S. Seal, and J. Karthikeyan, “Transmission electron microscopy of cold sprayed 1100 aluminum coating,” Scr. Mater., vol. 53, no. 7, pp. 845–850, 2005.

[14] J. F. de la Mora, S. V. Hering, N. Rao, and P. H. McMurry, “Hypersonic impaction of ultrafine particles,” J. Aerosol Sci., vol. 21, no. 2, pp. 169–187, 1990.

[15] J. Pattison, S. Celotto, A. Khan, and W. O’Neill, “Standoff distance and bow shock phenomena in the Cold Spray process,” Surf. Coat. Technol., vol. 202, no. 8, pp. 1443–1454, 2008.

[16] J. Akedo, “Aerosol deposition method for fabrication of nano crystal ceramic layer,” in Materials Science Forum, 2004, vol. 449, pp. 43–48.
[17] J. Akedo, “Aerosol deposition of ceramic thick films at room temperature: densification mechanism of ceramic layers,” J. Am. Ceram. Soc., vol. 89, no. 6, pp. 1834–1839, 2006.
[18] J. Akedo and M. Lebedev, “Influence of carrier gas conditions on electrical and optical properties of Pb (Zr, Ti) O3 thin films prepared by aerosol deposition method,” Jpn. J. Appl. Phys., vol. 40, no. 9S, p. 5528, 2001.
[19] J. Akedo, “Room temperature impact consolidation (RTIC) of fine ceramic powder by aerosol deposition method and applications to microdevices,” J. Therm. Spray Technol., vol. 17, no. 2, pp. 181–198, 2008.
[20] M. Lebedev, J. Akedo, and T. Ito, “Substrate heating effects on hardness of an α-Al 2 O 3 thick film formed by aerosol deposition method,” J. Cryst. Growth, vol. 275, no. 1, pp. e1301–e1306, 2005.
[21] J. Iwasawa, R. Nishimizu, M. Tokita, M. Kiyohara, and K. Uematsu, “Plasma-Resistant Dense Yttrium Oxide Film Prepared by Aerosol Deposition Process,” J. Am. Ceram. Soc., vol. 90, no. 8, pp. 2327–2332, 2007.
[22] M. Nahar, “Highly conductive, nanoparticulate thick films processed at low processing temperatures,” 2012.
[23] A. D. Albert, M. F. Becker, J. W. Keto, and D. Kovar, “Low temperature, pressure-assisted sintering of nanoparticulate silver films,” Acta Mater., vol. 56, no. 8, pp. 1820–1829, May 2008.
[24] C. Carlton and P. Ferreira, “Dislocation instability in nanoscale particles,” in MRS Proceedings, 2005, vol. 903, pp. 0903–Z14.
[25] L. B. Han, Q. An, S. N. Luo, and W. A. Goddard III, “Ultra-elastic and inelastic impact of Cu nanoparticles,” Mater. Lett., vol. 64, no. 20, pp. 2230–2232, 2010.
[26] K. Nordlund, T. T. Järvi, K. Meinander, and J. Samela, “Cluster ion–solid interactions from meV to MeV energies,” Appl. Phys. A, vol. 91, no. 4, pp. 561–566, 2008.
[27] K. Meinander and K. Nordlund, “Irradiation-induced densification of cluster-assembled thin films,” Phys. Rev. B, vol. 79, no. 4, p. 045411, 2009.
[28] M. Nahar, I. F. Gallardo, K. L. Gleason, M. F. Becker, J. W. Keto, and D. Kovar, “Metal-on-oxide nanoparticles produced using laser ablation of microparticle aerosols,” J. Nanoparticle Res., vol. 13, no. 8, pp. 3455–3464, 2011.
[29] K. L. Gleason, “Engineering nanocomposite polymer membranes for olefin/paraffin separation,” 2011.
[30] V. A. Marple and C. M. Chien, “Virtual impactors: a theoretical study.,” Environ. Sci. Technol., vol. 14, no. 8, pp. 976–985, 1980.
[31] D. B. Williams and C. B. Carter, “The Transmission Electron Microscope,” in Transmission Electron Microscopy, Springer US, 1996, pp. 3–17.
[32] C. Hammond and C. Hammond, The basics of crystallography and diffraction. Oxford University Press Oxford, 2009.
[33] G. K. Williamson and W. H. Hall, “X-ray line broadening from filed aluminium and wolfram,” Acta Metall., vol. 1, no. 1, pp. 22–31, 1953.

[34] S. Plimpton, “Fast parallel algorithms for short-range molecular dynamics,” J. Comput. Phys., vol. 117, no. 1, pp. 1–19, 1995.
[35] P. L. Williams, Y. Mishin, and J. C. Hamilton, “An embedded-atom potential for the Cu–Ag system,” Model. Simul. Mater. Sci. Eng., vol. 14, no. 5, p. 817, 2006.
[36] H. Zheng, A. Cao, C. R. Weinberger, J. Y. Huang, K. Du, J. Wang, Y. Ma, Y. Xia, and S. X. Mao, “Discrete plasticity in sub-10-nm-sized gold crystals,” Nat. Commun., vol. 1, p. 144, Dec. 2010.
[37] J. P. Hirth and J. Lothe, Theory of dislocations, 2nd ed. New York: Wiley, 1982.
[38] D. T. O’Brien, “Deposition and characterization of nanostructured silver thick films,” 2003.
[39] C. Huang, M. F. Becker, J. W. Keto, and D. Kovar, “Annealing of nanostructured silver films produced by supersonic deposition of nanoparticles,” J. Appl. Phys., vol. 102, no. 5, p. 054308, 2007.
[40] K. j. Ganesh, M. Kawasaki, J. p. Zhou, and P. j. Ferreira, “D-STEM: A Parallel Electron Diffraction Technique Applied to Nanomaterials,” Microsc. Microanal., vol. 16, no. 05, pp. 614–621, Oct. 2010.
[41] S. Zabihzadeh, S. Van Petegem, L. I. Duarte, R. Mokso, A. Cervellino, and H. Van Swygenhoven, “Deformation behavior of sintered nanocrystalline silver layers,” Acta Mater., vol. 97, pp. 116–123, Sep. 2015.
[42] S. Brandstetter, P. M. Derlet, S. Van Petegem, and H. Van Swygenhoven, “Williamson–Hall anisotropy in nanocrystalline metals: X-ray diffraction experiments and atomistic simulations,” Acta Mater., vol. 56, no. 2, pp. 165–176, 2008.
[43] P. M. Derlet, S. Van Petegem, and H. Van Swygenhoven, “Calculation of x-ray spectra for nanocrystalline materials,” Phys. Rev. B, vol. 71, no. 2, p. 024114, 2005.
[44] G. J. Noiseau, Film deposition and mechanical properties of silver produced by impaction of nanoparticles
[45] Private conversation with Dr Kovar
[46] Private conversation with Dr Becker
[47] U.F. Kocks, C.N. Tomé, H.R. Wenk, "Texture and anisotropy", Cambridge University Press, 2000
[48] H. Ashkenas, F.S. Sherman, "The structure and utilization of supersonic free jets in low-density wind tunnels", Experimental methods in rarified gas dynamics, 1966